MICRORESONATOR-BASED OPTICAL FREQUENCY COMBS FOR MICROWAVE AND MILLIMETER-WAVE APPLICATIONS

A Dissertation Presented to the Faculty of

the School of Engineering and Applied Science

University of Virginia

In Partial Fulfillment of the Requirements for the Degree of

Doctor of Philosophy

by

Beichen Wang

April 2023

Charlottesville, Virginia

Microresonator-based optical frequency combs for microwave and millimeter-Wave applications

Beichen Wang

(ABSTRACT)

Optical frequency comb is a powerful technology that coherently links the optical frequency and microwave frequency, and it has revolutionized metrology, time keeping, spectroscopy, and ranging. In the past decade, the microresonator-based soliton frequency combs, or soliton microcombs, have been extensively studied due to their small footprint, wide optical span, and high coherence. One major advantage of these microcombs is their high repetition-rate, ranging from GHz to 1 THz, which makes them ideal candidates for a range of applications, including wavelength multiplexing, self-referencing, and photonics-based high-speed RF oscillators. In this thesis, the soliton microcombs are used to build coherent links between optical, mmWave, and microwave frequencies. High-frequency millimeter-Waves are demonstrated with high power and high coherence by directly photodetecting the microcombs on a ultrahigh-speed photodiode. Significantly, the low noise of optical references can be coherently divided down to the generated mmWaves using integrated optical frequency division. On the other hand, the high repetition-rate can also bring challenges in its accurate detection when the frequency is above the bandwidths of photodiodes and electronics. In the later chapter of this thesis, an optical Vernier frequency division approach based on dual-comb coherent sampling is developed to coherently divide down the mmWave frequency to microwave frequency, which is used to count and

stabilize the microcomb sub-THz rep-rate using GHz bandwidth optoelectronics. Additionally, the microresonator dual-comb technique also enables the full electrical spectrum control including its amplitudes, phases, and the corresponding temporal waveforms. And an integrated photonics-based microwave arbitrary waveform generator was demonstrated with the potential to achieve high analog bandwidths and large effective number of bits thanks to the high repetition-rates of microcombs.

In memory of my grandpa, Hanmin Wang

Acknowledgments

First of all, I would like to thank my PhD advisor, Prof. Xu Yi, for his guidance and support. I have gained a better understanding of scientific research from him. I appreciate that he has always made time for discussion. I benefited by learning the way he solves scientific problems and manages research projects. Equally importantly, I was able to conduct my research without any financial concerns during entire five years thanks to his funding support.

I want to thank my present and former lab colleagues Zijiao Yang, Mandana Jahanbozorgi, Shuman Sun, Xiaobao Zhang, Haoran Chen, Ruxuan Liu, for the friendly and helpful work space we created. I would like to thank my collaborators from Prof. Andreas Beling's group at UVA; Jesse Morgan, Junyi Gao, and Keye Sun. I would like to thank my collaborators from Prof. Dan Blumenthal's group at UCSB; Kaikai Liu and Jiawei Wang.

I would like to thank all my friends for the valuable moments and inspirations they have brought to my life. I would like to thank my best friend and my fiancée, Mandana Jahanbozorgi, for her love, understanding, and support during the past years. Finally, I would like to thank my father Ze Wang, my mother Xiuli Ni, and my family for their continuous love, trust, and support.

Contents

List of Figures

Chapter 1

Introduction

Millimetre-wave (mmWave; 30 GHz to 300 GHz) and sub-Terahertz wave (sub-THz; 0.1 THz to 1 THz) technology continue to draw great interest due to its broad applications in wireless communications, radar, spectroscopy, and imaging (Kleine-Ostmann and Nagatsuma 2011; Koenig et al. 2013; Ghelfi et al. 2014; Schmalz et al. 2017). Compared with existing microwave systems operating at lower frequencies, the high carrier frequencies of mmWaves and sub-THz waves are advantageous to expand the bandwidth and data capacity of wireless communications (Nagatsuma, Ducournau, and Renaud 2016). For applications including radar, spectroscopy, and imaging (Cooper et al. 2008; De Lucia, Petkie, and Everitt 2008), the shorter wavelengths of mmWaves and sub-THz waves can also provide higher resolution. However, for pure electronic solutions, the generation of higher carrier frequencies requires smaller oscillator structures which leads to higher noise and lower output power. Consequently, the high noise will reduce the effective data rate for wireless communications, and limit the sensitivity in radar, spectroscopy, and imaging. Besides the carrier generation, modulation, filtering and multiplexing beyond 100 GHz are still challenging for existing electronic solutions. In contrast, photonic oscillators operate at frequencies of hundreds of THz and the frequency of the electrical signal produced by, e.g., the heterodyne detection of two lasers, is limited only by the photodiode bandwidth. Together with their low power dissipation and low-loss fiber remoting, microwave photonics technologies have gained tremendous interest for the generation, processing and distribution of microwave and mmWave signals in the past decades (Capmany and Novak 2007; Yao 2009; Marpaung et al. 2013).

In a parallel research line, the optical frequency combs have been extensively studied since it was introduced twenty years ago (Jones et al. 2000; Udem, Ronald Holzwarth, and Hänsch 2002; Cundiff and J. Ye 2003; S. Diddams, Bergquist, et al. 2004; Scott A Diddams 2010; Nathan R Newbury 2011). An optical frequency comb typically consists of hundreds to thousands of equally spaced laser lines in the frequency domain. The frequency of each comb line can be expressed in terms of offset frequency and repetition frequency, where the latter usually ranges from tens of MHz to tens of GHz (Minoshima and Matsumoto 2000; Holzwarth et al. 2000; Fortier, Bartels, and Scott A Diddams 2006; Steinmetz et al. 2008; Bartels, Heinecke, and Scott A Diddams 2009; Carlson et al. 2018). Therefore, the optical frequency comb technology coherently connects radio frequencies to optical frequencies, and has found its tremendous applications including but not limited to, optical clocks (S. Diddams, Udem, et al. 2001; S. Diddams, Bergquist, et al. 2004), optical frequency division (OFD) (Fortier, Kirchner, et al. 2011), optical frequency synthesis (Holzwarth et al. 2000; Jones et al. 2000; Ma et al. 2004), optical arbitrary waveform generation (Z. Jiang, Seo, et al. 2005; Cundiff and Weiner 2010), spectroscopy (Scott A Diddams, Hollberg, and Mbele 2007; Ian Coddington, William C Swann, and Nathan R Newbury 2008; Cingöz et al. 2012), and ranging (Coddington, William C Swann, et al. 2009). However, the repetition rate of conventional combs is limited by their size and structural complexity, and does not extend to mmWave frequency. To date, 30 GHz is the highest repetition rate reported (Carlson et al. 2018). For high-frequency mmWave or sub-THz technology, conventional combs usually require post-spectral filtering to remove unnecessary comb lines (Kuo et al. 2010; Wun et al. 2014), to effectively achieve high comb repetition frequency, or Nyquist bandwidth (half of the comb repetition frequency). This will nonetheless increase the complexity and costs of the system.

The microresonator-based frequency combs (Del'Haye et al. 2007; Tobias J Kippenberg, Ronald Holzwarth, and S. Diddams 2011), also called as microcombs, are the optical frequency combs recently demonstrated in ultra-high-Q microresonators (Kerry J Vahala 2003). The typical microresonator diameters range from 10's μm to several mm, and the corresponding cavity free-spectral-range (FSR) /comb repetition rate (rep-rate) ranges from 2 GHz to 1 THz (Suh and Kerry Vahala 2018; Q. Li et al. 2017; M. H. P. Pfeiffer et al. 2017). In 2014, the dissipated Kerr soliton was discovered in the microresonator (Herr, Brasch, et al. 2014). These solitary wave packets leverage Kerr nonlinearity to compensate for cavity loss and to balance chromatic dispersion (Akhmediev and Ankiewicz 2008; Leo et al. 2010; Herr, Brasch, et al. 2014). In frequency domain, the soliton microcombs are equally distant and exhibit a sech^2 shaped smooth spectral envelope. The reduction of resonator mode volume increases the intracavity Kerr nonlinearity, lowers the operation pump power and, extends the comb spectrum span. This has enabled demonstrations of battery-operated soliton combs at 194 GHz repetition rate (Stern et al. 2018), and octave-spanning soliton generation for self-referencing in a resonator with 1 THz free-spectral-range (FSR) (Spencer et al. 2018). High repetition rates (rep-rates) are also desired in many comb-based applications. For instance, the maximum acquisition speed in dual-comb spectroscopy (Suh, Q.-F. Yang, et al. 2016; Pavlov et al. 2017; Dutt et al. 2018), ranging (Trocha et al. 2018; Suh and Kerry J Vahala 2018), and imaging (Bao, Suh, and Kerry Vahala 2019; Yi, Q.-F. Yang, K. Y. Yang, and Kerry Vahala 2018), all increase linearly with the comb repetition rate. In terms of microwave/mmWave generation, photodetecting the soliton microcombs will convert the highly coherent optical solitons into mmWaves or sub-THz oscillators at the frequency of the comb repetition frequency (Liang et al. 2015; J. Liu, Lucas, et al. 2020). In addition, the soliton microcombs oscillator can also reduce the phase noise from its pump laser as a result of its unique noise transfer mechanism (Yi, Q.-F. Yang, Xueyue Zhang, et al. 2017; Lucas et al. 2020).

In this thesis, several microwave and mmWave applications using integrated microresonator soliton frequency combs are explored. Here is an overview of the thesis chapters:

Chapter 2 introduces the basics of optical microresonators, including free-spectral-range, quality-factor, coupling regimes, cavity dispersion and nonlinearity. An experimental characterization method of the microresonators is also briefly discussed.

Chapter 3 provides the theoretical background of the soliton microcombs, including the analysis in both frequency domain and time domain. A simulation method is included at the end of the chapter.

Chapter 4 describes the experimental demonstration of 100 GHz mmWave generation using soliton microcombs and high-speed MUTC-PD. The soliton provides 6 dB higher power and two orders better coherence compared to the conventional heterodyne detection approach. This work provides a viable path to chip-scale, high-power, low-noise, high-frequency sources for integrated photonic mmWave applications.

Chapter 5 presents an integrated solution of optical frequency division to reduce the phase noise of soliton repetition rate for low-noise mmWave generation. Both reference cavity and soliton microresonator are integrated on Si_3N_4 platform. Our preliminary results are given and discussed.

Chapter 6 provides an integrated solution of sub-THz soliton microcombs repetition rate detection using a dual-comb technique. A Vernier frequency division method is developed to count and stabilize a 200 GHz signal using electronics with GHz bandwidth.

Chapter 7 explores the power of the microresonator dual-comb coherent sampling. A radio-frequency arbitrary waveform generator was realized by spectral line-by-line shaping one of the optical soliton microcombs. Different arbitrary waveforms are demonstrated. An analysis of the effective number of bits using the dual-comb approach is discussed.

Chapter 2

Background of optical microresonators

2.1 Introduction

Optical microresonator, or microcavity (Kerry J Vahala 2003), is a small photonic device that can trap the light within its micro-scale circular structure through total internal reflection. At certain optical frequencies, the light can keep circulating inside the microresonator until it dissipates.

The dimension of a microresonator is typically at the scale of micrometers to millimeters, which provides a small mode volume to accommodate the optical field. As a result, the optical field will not only just stay inside the microresonator, but also a portion of the optical field can overlap with anything placed near the optical mode. Therefore, the effective refractive index of the optical field is relatively sensitive to changes to its confinement structure.

On the other hand, low-loss is usually desired in optical microresonators to enhance the light-matter interaction that can find applications such as cavity quantum electrodynamics, biological/chemical sensing, and optomechanics (Kerry J Vahala 2003; Hofer, Schliesser, and Tobias J Kippenberg 2010; Ward and Benson 2011). What else, the light energy can build up inside the low-loss microcavity by a few magnitudes of order, and the high intracavity power can usually lead to strong nonlinear optical effects.

In this chapter, I will introduce the key properties of microresonators including cavity free-spectral-range, cavity loss and quality factor, dispersion, nonlinearity, and coupling schemes. Experimental methods of characterizing these properties will also be discussed.

2.2 Types of microresonators

There are several types of microresonators, including whispering-gallery mode (WGM) resonators (A. Matsko et al. 2005), micro-ring resonators (Rabus 2007), photonic crystal resonator (Altug and Vučković 2004), Fabry–Pérot microresonator (Obrzud, Lecomte, and Tobias Herr 2016), etc.

Whispering-gallery mode (WGM) resonators include micro-toroids [SiO_2 (Del'Haye et al. 2007)], micro-disks [SiO_2 (Yi, Q.-F. Yang, K. Y. Yang, Suh, et al. 2015)], micro-spheres [SiO_2 (Mikhail L Gorodetsky, Savchenkov, and Vladimir S Ilchenko 1996)], micro-rods [MgF_2 (Herr, Brasch, et al. 2014), SiO_2 (S. Zhang, Silver, Del Bino, et al. 2019)]. The light can be coupled into this type of resonator via an optical tapered fiber. Typically, the WGM resonators have very low material losses, which will give a very high quality factor over 10^8 (the concept of Q-factor will be introduced in a later section).

Micro-ring resonators are closed-loop waveguides, and the light can be coupled in and out through bus-waveguides that are integrated near the ring-resonator. With that being said, the microring resonators can have different geometrical shapes including ring (Gondarenko, Levy, and Lipson 2009), racetrack (Long Zhang et al. 2020), etc. Due to its compatibility with integration, the micro-ring resonators have been studied at different material platforms including Si_3N_4 (Brasch et al. 2016), Si (Griffith et al. 2015), AlN (Gong et al. 2018), AlGaAs (Chang et al. 2019), $LiNbO_3$ (He et al. 2019). The qualify factor of micro-ring resonators is usually at the order of 10^6.

2.3 Cavity free-spectral-range (FSR)

Light can circulate inside the microresonator if its frequency is on cavity resonance frequency. This can be satisfied when the optical path of a cavity roundtrip equals an integer times the light wavelength:

$$2\pi nr = m\lambda_m \tag{2.1}$$

where n is the refractive index, r is the radius of the microresonator, and λ_m is the m-th resonance wavelength in the vacuum. Using light frequency-wavelength conversion $\nu = c/\lambda$ where c is the speed of light, the resonant frequency is given by

$$\nu_m = m\frac{c}{2\pi nr} \tag{2.2}$$

The free-spectral-range (FSR), known as the frequency spacing between two neighbouring resonant modes, is

$$FSR = \frac{c}{2\pi nr} \tag{2.3}$$

At first sight, FSR looks like a constant value. However, the refractive index in most materials changes with wavelength due to the dispersion effect. As a result, FSR also changes with the optical wavelength.

The cavity roundtrip time is equal to the inverse of the FSR,

$$t_R = \frac{2\pi nr}{c} = \frac{1}{FSR}. \tag{2.4}$$

2.4 Cavity loss, Q-factor, and finesse

Cavity loss

There are a variety of losses happening inside the optical microresonators when light is traveling inside them, such as

- Material absorption (material intrinsic loss, fabrication impurities...),
- Scattering (sidewall, fabrication imperfections...),
- Radiation (small radius),
- Coupling to other optical modes,
- Coupling to other waveguides.

...

It is conventional to consider the first four sources as cavity intrinsic loss, and the last term as coupling loss. Because of these losses, the energy of the optical field will decay exponentially inside the microresonator at a rate of κ (in radian),

$$\frac{dE_{stored}}{dt} = -\kappa E_{stored} \tag{2.5}$$

Assuming there is no pump source feeding into the cavity, an analytical solution of the stored energy can be expressed over time,

$$E_{stored}(t) = E_{stored}(0)e^{-\kappa t} \tag{2.6}$$

The lifetime of the light inside the cavity can be defined when its energy decayed to $1/e$ of the initial energy at $t = 0$,

$$t_L = 1/\kappa \tag{2.7}$$

which is the inverse of the dissipation rate κ.

Q-factor

An important factor of microresonators to characterize cavity loss is called the quality factor (Q-factor). There are two common definitions for Q, and we will see they are equivalent to each other. The first one is using the ratio between the optical angular frequency ($\omega = 2\pi\nu$) and the energy dissipation rate,

$$Q = \frac{\omega}{\kappa} = \frac{\nu}{\kappa/2\pi} \tag{2.8}$$

The second definition uses the ratio between the initial stored energy inside the cavity and the energy dissipation within one optical cycle period ($T = 2\pi/\omega$),

$$Q = 2\pi \frac{E_{stored}(0)}{\frac{dE_{stored}}{dt} \times T} = \frac{\omega}{\kappa} \tag{2.9}$$

which gives the same result as Equation 2.8.

Finesse

Another important parameter of the resonator, finesse $\mathcal{F}$, is defined with 2π times the ratio between FSR and the resonance linewidth (which is equivalent to κ, this will be explained in a later section),

$$\mathcal{F} = 2\pi \frac{FSR}{\kappa} = 2\pi \frac{t_L}{t_R} \tag{2.10}$$

which relates to how many roundtrips the light can travel inside the cavity within its lifetime. In an ideal cavity with no loss $\kappa = 0$, the light can circulate infinitely ($\mathcal{F} = \infty$).

2.5 Coupling light to microresonator

To study the optical phenomenon inside the cavity, one needs to couple the light into the microresonator. Different coupling approaches have been realized including prism coupling (M. Gorodetsky and V. Ilchenko 1994), tapered fiber coupling (Spillane et al. 2003), and bus waveguide coupling (M. H. Pfeiffer, J. Liu, et al. 2017).

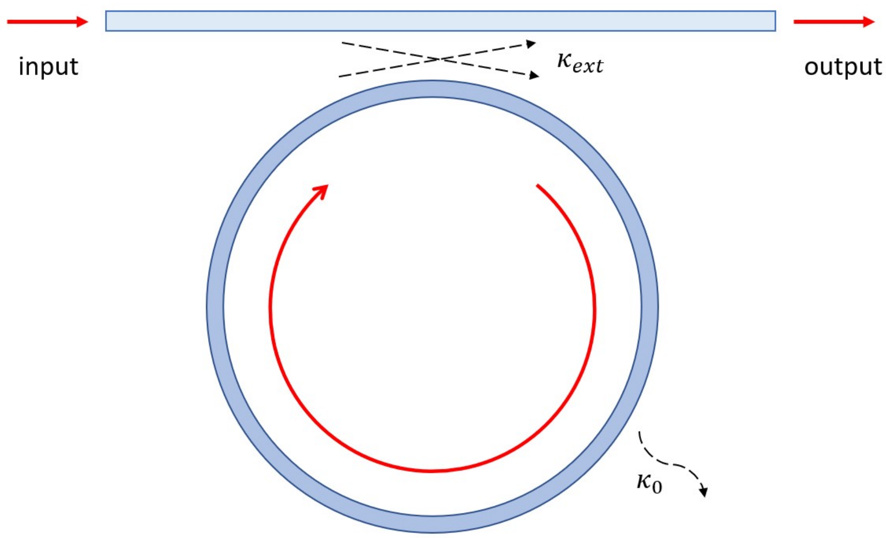

Figure 2.1: **Diagram of coupling between waveguide and microresonator.**

2.5.1 Modelling of the light propagation inside the microresonator

Here, a diagram of waveguide coupling to microring resonator is shown in Fig. 2.1:

i) For waveguide coupling, the pump light needs to be first coupled to the input port of the bus waveguide through a lensed fiber or a grating coupler. An efficient fiber-to-waveguide coupling is typically considered with an insertion loss of 2 dB or below per facet.

ii) Then, the light is coupled in the micro-ring resonator from the bus waveguide through evanescent coupling. The coupling rate is described as κ_{ext}, which is determined by the overlapping between the optical modes between two waveguides. In the experiment, one can vary κ_{ext} by adjusting the waveguide width, coupling interaction length, and the gap distance between resonator waveguide and bus waveguide.

iii) The light circulates inside the microresonator when its frequency is on cavity resonance. Its energy decays due to intrinsic loss κ_0, which is caused by material absorption, scattering, or radiation loss.

iv) The light is coupled out from the micro-ring resonator to the bus waveguide through evanescent coupling with the same coupling rate κ_{ext}.

v) Finally, the light can be coupled out from the output port of the bus waveguide and collected by another lensed fiber or grating coupler.

2.5.2 Theoretical analysis of spectral transmission and resonance linewidth

The optical field inside the microresonator experiences intrinsic loss κ_0 and coupling loss κ_{ext}, as well as a driving field from the pump light. Its propagation equation can be described as

$$\frac{dA(t)}{dt} = -\frac{\kappa_0 + \kappa_{ext}}{2} A(t) + \sqrt{\kappa_{ext}} S_{in} e^{-i(\omega-\omega_0)t}. \tag{2.11}$$

It is worth noting that this equation is normalized by single photon energy $\hbar\omega_0$ (ω_0 is the cavity resonant frequency), so that $|A(t)|^2$ is in the unit of the photon number and $A(t)$ represents the normalized field amplitude inside the cavity. $|S_{in}|^2 = P_{in}/\hbar\omega_0$ is in the unit of the pump laser photon number per second in the bus waveguide by normalizing the input pump power P_{in} by $\hbar\omega_0$. The pump field is coupled to the cavity through a rate of $\sqrt{\kappa_{ext}}$. By writing $\kappa = \kappa_0 + \kappa_{ext}$ and switching the field into a relative frequency frame by $a(t) = A(t)e^{i(\omega-\omega_0)t}$, Equation 2.11 can be written as

$$\frac{da(t)}{dt} = -i(\omega_0 - \omega)a - \frac{\kappa}{2}a + \sqrt{\kappa_{ext}}S_{in}. \tag{2.12}$$

The steady-state solution ($da(t)/dt = 0$) of the intracavity field is given by,

$$a = \frac{\sqrt{\kappa_{ext}}}{i(\omega_0 - \omega) + \kappa/2}S_{in} \tag{2.13}$$

and the photon number inside the cavity is

$$|a|^2 = \frac{\kappa_{ext}}{(\omega_0 - \omega)^2 + \kappa^2/4}|S_{in}|^2 = \frac{\kappa_{ext}P_{in}/\hbar\omega_0}{(\omega_0 - \omega)^2 + \kappa^2/4}. \tag{2.14}$$

The intracavity power can be calculated by the ratio between the intracavity energy and the cavity roundtrip time $\hbar\omega_0|a|^2/t_R$, and the power enhancement G from the input pump power to the intracavity built-up power is given by

$$G = \frac{\hbar\omega_0|a|^2/t_R}{P_{in}} = \frac{\kappa_{ext}/t_R}{(\omega_0 - \omega)^2 + \kappa^2/4}. \tag{2.15}$$

For the special case of $\kappa_0 = \kappa_{ext} = \kappa/2$ (critical coupling) and $\omega = \omega_0$ (pump laser is on resonance) the power enhancement is

$$G = 2\frac{1}{t_R\kappa} = \frac{2FSR}{\kappa} = \mathfrak{F}/\pi. \tag{2.16}$$

The normalized output field is given by

$$s_{out} = s_{in} - \sqrt{\kappa_{ext}}a, \tag{2.17}$$

and the power transmission results in

$$T(\omega) = \frac{|s_{out}|^2}{|s_{in}|^2} = 1 - \frac{\kappa_0 \kappa_{ext}}{(\omega_0 - \omega)^2 + (\kappa_0 + \kappa_{ext})^2/4}. \tag{2.18}$$

Therefore, the transmission of the cavity resonance has a Lorentzian lineshape in the frequency domain, as shown in Fig. 2.2. The full width at half minimum of the resonance dip equals to the total loss $\kappa = \kappa_0 + \kappa_{ext}$.

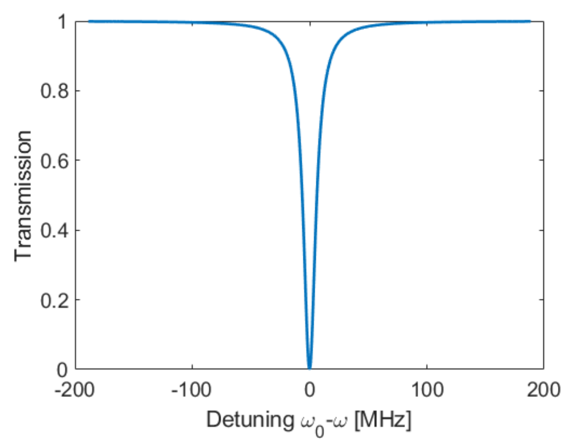

Figure 2.2: **Cavity resonance transmission.** $\kappa_0 = \kappa_{ext} = 2\pi\times$ 1 MHz is set as an example.

2.5.3 Different coupling regimes

It is conventional to describe the coupling strength using the ratio between the coupling loss κ_{ext} and the total loss $\kappa = \kappa_0 + \kappa_{ext}$,

$$\eta = \frac{\kappa_{ext}}{\kappa} \tag{2.19}$$

and depending on the coupling strength, the coupling condition can be divided into three regimes:

Under-coupling $\kappa_{ext} < \kappa_0$

In the under-coupling regime, coupling strength $\eta < 0.5$. The coupling rate is slower than the cavity intrinsic loss rate. The transmission $T > 0$ happens when laser is on resonance ($\omega = \omega_0$).

Critical-coupling $\kappa_{ext} = \kappa_0$

In the critical-coupling regime, coupling strength $\eta = 0.5$. The coupling rate is equal to the cavity intrinsic loss rate. The transmission $T = 0$ happens when laser is on resonance ($\omega = \omega_0$), which means the transmission from the waveguide output vanishes as a result of the interference between the transmitted pump field and the cavity field coupled to the waveguide. Due to the energy conservation law, the intracavity power will be the highest in the critical-coupling regime.

Over-coupling $\kappa_{ext} > \kappa_0$

In the over-coupling regime, coupling strength $\eta > 0.5$. The coupling rate is faster than the cavity intrinsic loss rate. The transmission $T > 0$ happens when laser is on resonance ($\omega = \omega_0$).

For WGM resonators, the coupling rate κ_{ext} can be conveniently controlled in the experiment by adjusting the distance between the tapered fiber and the microresonator. However, for micro-ring resonators, the gap distance is fixed after the fabrication process. To reach different coupling regimes, one usually needs to design an array of micro-ring resonators with scanning gap distances to the bus waveguides if the intrinsic loss rate is unknown or not predictable in certain fabrication processes.

2.5.4 Drop-port configuration

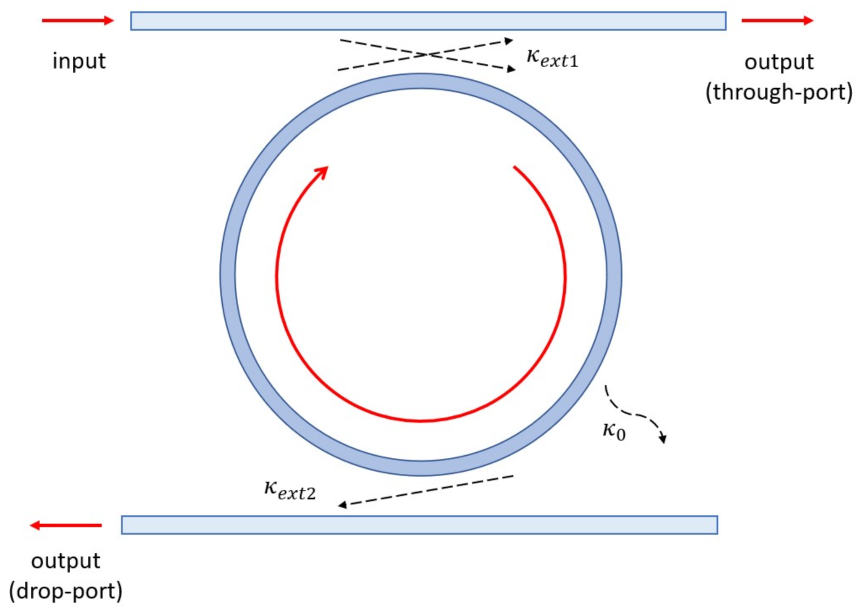

Figure 2.3: **Diagram of coupling between waveguide and microresonator with drop-port.**

The model described above applies to the case that the microresonator is coupled to a single bus-waveguide or a tapered fiber, which is called a through-port geometry. Sometimes, a drop-port can be added for purposes of optical filters. In this case, the light can escape the cavity from both through-port κ_{ext1} and drop-port κ_{ext2}. To reach the critical coupling condition on the through-port, the condition $\kappa_{ext1} = \kappa_0 + \kappa_{ext2}$ needs to be satisfied.

2.6 Cavity dispersion and resonance spectrum

In a microresonator, the cavity can usually accommodate different transverse mode families depending on the dimensions and shapes of the microresonator. It is also possible to design a single-mode waveguide for micro-ring resonators that can only support fundamental modes, such as TE_{00} and TM_{00}.

For each mode family, it consists of a series of longitudinal modes whose frequencies are separated by one FSR in the frequency domain. However, as a result of the dispersion, the refractive index is changing with the optical frequency. And the cavity FSR is not a constant in the frequency domain. To describe the resonant frequencies of a certain transverse mode family, one can first select one arbitrary resonance frequency ω_0 as the center frequency, and express its neighboring resonant frequencies ω_μ using Taylor expansion,

$$\omega_\mu = \omega_0 + D_1\mu + \frac{D_2}{2}\mu^2 + \sum_{j=3}^{\infty} \frac{D_j}{j!}\mu^j \tag{2.20}$$

where $\mu = 0, \pm1, \pm2, ...$ is the relative mode number to the center mode, and D_j is the j-th order dispersion. $D_1/2\pi$ is the cavity FSR of the 0-th mode. D_2 is the cavity group velocity dispersion and can be connected to the second-order dispersion β_2 of optical waveguides using $D_2 = -(c/n)\beta_2 D_1^2$. It is conventional to say the cavity dispersion is anomalous when $D_2 > 0$ ($\beta_2 < 0$, and the cavity dispersion is normal when $D_2 < 0$ ($\beta_2 > 0$). Sometimes, all the dispersion terms except for the FSR term can be expressed as a summation called integrated dispersion,

$$D_{int} = \sum_{j=2}^{\infty} \frac{D_j}{j!}\mu^j \tag{2.21}$$

and one can tailor the dispersion (dispersion-engineering) by adjusting the geometry of the microresonator.

2.7 Cavity nonlinearity

When light propagates in the cavity, the light electrical field can affect the cavity material dielectric polarization density, which can be expressed in Taylor expansion,

$$\mathbf{P} = \epsilon_0(\chi^{(1)}\mathbf{E} + \chi^{(2)} : \mathbf{EE} + \chi^{(3)} \vdots \mathbf{EEE} + \cdots) \tag{2.22}$$

where 0 is the vacuum permittivity and $\chi^{(n)}$ is an $(n+1)$-th rank tensor that represents the n-th order of the electric susceptibility.

When the light intensity is low inside the cavity, the first term $\chi^{(1)}$ dominates and provides a linear polarization response to the material. $\chi^{(1)}$ is equal to $\epsilon_r - 1$ where ϵ_r is the relative permittivity of the dielectric materials.

When the light intensity is high, the higher-order terms $\chi^{(2)}, \chi^{(3)}, ...$ can be dominating. Microresonator is an ideal platform to study the nonlinear optics as the optical power can build up easily with high cavity FSR and low loss. The second term $\chi^{(2)}$ provides a second-order nonlinear polarization that quadratically changes with light electrical field. And the frequency component of the polarization is the sum of the frequencies of two interacting light electrical fields. As a result, new frequencies can be generated through three-wave-mixing process such as frequency doubling, sum and difference frequency generation, optical parametric oscillation, etc. However, $\chi^{(2)}$ is a non-zero value only when the material crystal is non-centrosymmetric. Such materials are not very common, including $LiNbO_3$ and AlN.

The third term $\chi^{(3)}$ provides a third-order nonlinear polarization that changes with the cubic of light electrical field. Most materials in nature has non-zero $\chi^{(3)}$. The frequency components of the third-order polarization is the sum of the frequencies of three interacting light electrical fields. As a result, new frequencies can be generated through four-wave-mixing process.

2.8 Experimental characterization of microresonators

Characterizing microresonators is the first step before using them in the experiment. The most important cavity parameters include Q-factor, free-spectral-range, and dispersion. They can be characterized by different experimental approaches. Here, a widely used method using calibrated fiber Mach-Zehnder interferometer (MZI) will be introduced. It serves as a frequency reference and can measure all the parameters mentioned above.

The MZI used in our experiment is a fiber-based interferometer with two unbalanced arms. One can easily construct it by combining two 50/50 fiber couplers and adding a fiber delay Δ_L in one of the arms. When sending laser into it, the laser gets split into two optical paths by the first 50/50 coupler, and one of them accumulates more phase due to the fiber delay. Then they are combined by the second 50/50 coupler, and their interference output is sent to a photodetector (PD). The PD signal is recorded on an oscilloscope. When sweeping the laser frequency, the MZI interference pattern will be present on oscilloscope due to the relative phase changes between two arms.

The free-spectral-range of the interferometer (the frequency separation between two interference peaks) can be approximately expressed by $FSR_{MZI} = c/n\Delta_L$. Similar to cavity FSR, the interferometer FSR is not a constant value due to the fiber dispersion. Therefore, a proper dispersion calibration is necessary. For a 2-meter fiber delay, FSR_{MZI} is around 100 MHz.

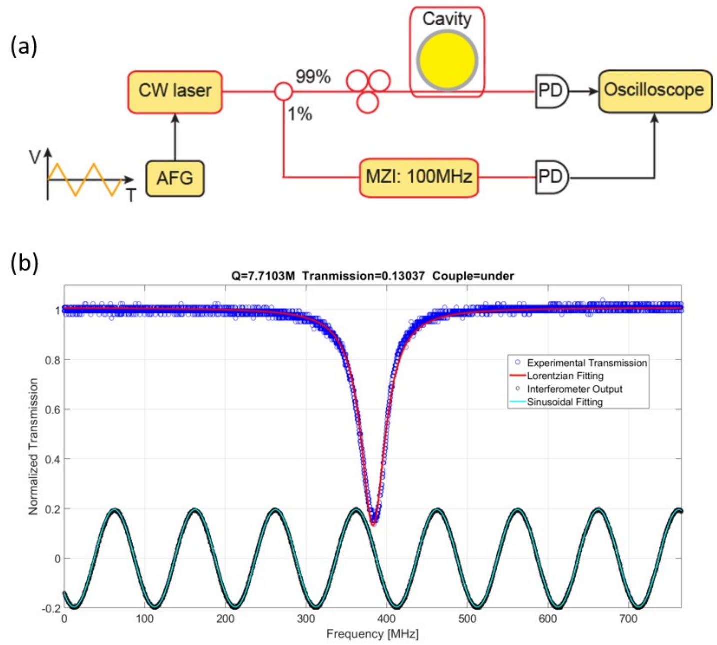

Figure 2.4: **Experimental characterization of cavity Q-factor. (a)** Experimental setup. **(b)** Example of the measured transmission of a 7 million Q microresonator.

To characterize the quality factor of the microresonator, the laser can be split by a 90/10 fiber coupler, where 90% goes to the microresonator then a photodetector, and 10% goes to the fiber MZI (Fig. 2.4). With knowing the interferometer FSR, one can monitor the laser frequency change in real time, and use it as a reference to calibrate the microcavity resonance linewidth and calculate the quality factor using Equation 2.8.

To characterize the resonance spectrum within a wide laser frequency scanning range, it is also convenient to use fiber MZI to calibrate the frequency separation between neighbouring resonances. The dispersion can be also obtained using the data retrieved from the resonance spectrum measurement. In most cases, the integrated dispersion is dominated by group velocity dispersion D_2 as higher-order dispersion coefficients are small. Therefore, the integrated dispersion will exhibit a parabolic shape by extracting the D_1 term from the resonance frequency data,

$$D_{int} = \omega_\mu - \omega_0 - D_1\mu = \frac{D_2}{2}\mu^2 + \sum_{j=3}^{\infty}\frac{D_j}{j!}\mu^j \sim \frac{D_2}{2}\mu^2 \tag{2.23}$$

and D_2 can be calculated with a proper parabolic fitting. An example is given in Fig. 2.5

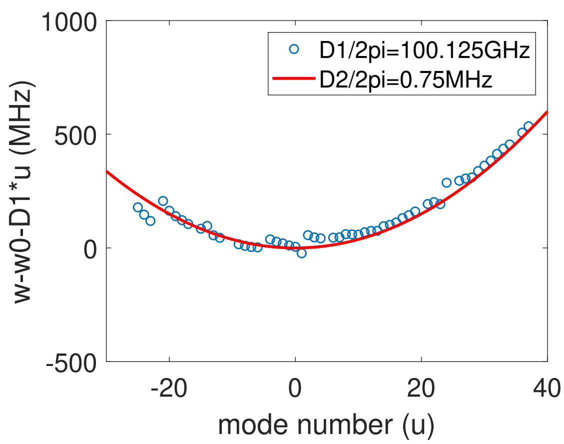

Figure 2.5: **Mode spectrum measurement using laser wide range scanning method.** A 100 GHz FSR SiN microresonator is characterized with a dispersion $D_2/2\pi = 0.75$ MHz.

Chapter 3

Background of microresonator soliton frequency combs

3.1 Introduction

The microresonator frequency comb (microcombs) was first demonstrated in 2007 (Del'Haye et al. 2007). The high quality-factor and small mode volume of microresonators make it an ideal platform for studying cavity nonlinear optics such as frequency comb generation. On the other hand, due to the small size of the microresonators, the optical frequency comb technology became possible to be integrated on a photonic chip (Herr, Brasch, et al. 2014; Brasch et al. 2016; Xiang, J. Liu, et al. 2021; W. Jin et al. 2021).

The microcombs can be formed using cavity Kerr effect. The Kerr effect can induce four-wave-mixing process, which converts the photons from the pump laser to new photons in other cavity longitudinal modes through four-wave-mixing process. In addition to the pump gain and cavity nonlinearity, the microcombs also experience cavity dispersion and cavity loss. The soliton microcomb is a special type of microcombs as a result of the double balance of cavity dispersion with cavity nonlinearity and cavity loss with Kerr-induced nonlinear gain (Herr, Brasch, et al. 2014; Brasch et al. 2016; Tobias J Kippenberg, Gaeta, et al. 2018). In time domain, it is in the form of a train of optical wavepackets that maintain its pulse shape when circulating inside the cavity. In frequency domain, the soliton microcombs feature a hyberbolic secant shaped spectral envelope and its frequency lines are equally spaced by roughly one cavity FSR. To date, soliton microcombs have been used in many applications, including spectroscopy (Suh, Q.-F. Yang, et al. 2016; Pavlov et al. 2017; Dutt et al. 2018), ranging (Trocha et al. 2018; Suh and Kerry J Vahala 2018), and imaging (Bao, Suh, and Kerry Vahala 2019; Yi, Q.-F. Yang, K. Y. Yang, and Kerry Vahala 2018).

In this chapter, the dynamics of microcombs will be introduced in both frequency domain and time domain theoretically, and the numerical simulation method is then given.

3.2 Four-wave-mixing through Kerr nonlinearity

A single frequency continuous-wave (c.w.) pump laser can be used to generate microresonator frequency comb with hundreds of frequency lines. The principle behind the comb generation is based on four-wave-mixing (FWM), which relies on the third-order nonlinear effect (Kerr effect) in the cavity. FWM describes that three light waves with same or different frequencies f_1, f_2, f_3 can interact with each other through nonlinear effect, and generate a fourth light wave with new frequencies $f_4 = |f_1 \pm f_2 \pm f_3|$. The energy conservation is met in this process.

Comb generation based on FWM process can be intuitively understood if we look at the laser in the quantum picture of photons. When the pump laser is coupled into the resonator, two pump photons with same frequency ω_p) can interact with a signal photon (rising from quantum noise) with frequency ω_s, and generate an idler photon with frequency $\omega_i = 2\omega_p - \omega_s$. Vice versa, the two pump photons can also interact with an idler photon and generate a signal photon with frequency $\omega_s = 2\omega_p - \omega_i$. This process involving two pump photons with the same frequency is called degenerate FWM, which happens at the early stage of comb generation.

Then, the non-degenerate FWM process can happen when the pump photon, signal photon, and idler photon interact with each other and generate another new photon whose frequency is $\omega_p + \omega_s - \omega_i$ or $\omega_p + \omega_i - \omega_s$. Such effects can also cascaded and more and more photons with new frequencies can be generated through degenerate FWM and non-degenerate FWM. A nice illustration and explaination can be found in (Herr, Hartinger, et al. 2012), and more complex FWM situations can be found there. In general, the four-wave-mixing process can occur for any interacting three waves. However, the phase matching condition $k_4 = k_1 + k_2 - k_3$ has to be satisfied for the efficient generation of the fourth wave, where the dispersion needs to be considered.

Note that only those photons whose frequencies are on cavity resonances can stay inside the microresonator, while the rest will dissipate due to the high loss. Therefore, one will see the laser lines exhibiting a comb structure in the frequency domain, so called microresonator frequency comb.

3.3 Coupled mode equations

Coupled mode equations can be used to analytically describe the microresonator comb formation in the frequency domain. The equations of motion for the field of μ-th mode A_μ can be written as (T. J. A. Kippenberg 2004; Chembo and N. Yu 2010; Herr, Hartinger, et al. 2012),

$$\frac{dA_\mu}{dt} = -(i\omega_\mu + \kappa/2)A_\mu + \delta_{0,\mu}\sqrt{\frac{\kappa_{ext}P_{in}}{\hbar\omega_0}}e^{-i\omega_p t} + ig\sum_{\mu_1,\mu_2,\mu_3} A_{\mu_1}A_{\mu_2}A^*_{\mu_3}, \tag{3.1}$$

where ω_μ is the angular frequency of A_μ, $\kappa = \kappa_0 + \kappa_{ext}$ is the total dissipation rate equal to the sum of intrinsic loss rate and external coupling rate. P_{in} is the power of the pump laser on chip. ω_0 and ω_p are the angular frequencies of the pumped cavity resonance and the pump laser, and $\delta_{0,\mu}$ means only the field A_0 gains from the pump laser directly. Note that the equation is normalized by single photon energy $\hbar\omega_0$ so that $|A_\mu|^2$ is in the unit of photon number. $g = \hbar\omega_0^2 c n_2/n_0^2 V_{eff}$ is the equivalent Kerr nonlinear coefficient in the microresonator where c, n_2, n_0, V_{eff} are the speed of light in vacuum, Kerr nonlinear refractive index, refractive index, and effective cavity mode volume, respectively. The last term represents the four-wave-mixing nonlinear process.

The fast oscillation ω_μ term in this equation can be eliminated by choosing a relative frequency frame of $a_\mu = A_\mu e^{-i(\omega_p + D_1\mu)t}$ ($D_1/2\pi$ is the cavity FSR at pumped mode frequency),

$$\frac{da_\mu}{dt} = -(i\omega_\mu - i\omega_p - iD_1\mu + \kappa/2)a_\mu + \delta_{0,\mu}f + ig\sum_{\mu_1,\mu_2,\mu_3} a_{\mu_1}a_{\mu_2}a^*_{\mu_3}e^{-iD_1(\mu 1+\mu 2-\mu 3-\mu)t}, \tag{3.2}$$

where $f = \sqrt{\kappa_{ext}P_{in}/\hbar\omega_0}$ is the normalized pump power. In microresonators, the dissipation rate is usually much smaller than FSR $\kappa \ll D_1$. Therefore, the four-wave-mixing term oscillates fast compared to the field evolution rate κ. Only when $\mu = \mu_1 + \mu_2 - \mu_3$, the four-wave-mixing term has non-zero contribution. Therefore, Equation 3.2 can be further reduced to,

$$\frac{da_\mu}{dt} = -(i\omega_\mu - i\omega_p - iD_1\mu + \kappa/2)a_\mu + \delta_{0,\mu} f + ig \sum_{\mu_1,\mu_2} a_{\mu 1} a_{\mu 2} a^*_{\mu 1+\mu 2-\mu}, \tag{3.3}$$

Although there is no exact solution known to the equation, it can provide some important information of the comb formation. For example, the threshold of the parametric oscillation can be derived from Equation 3.3 when only considering the pump mode $\mu = 0$ and a pair of the primary sidebands (signal and idler) $\mu = \pm m$ (T. Kippenberg, Spillane, and Vahala 2004; Chembo and N. Yu 2010; Herr, Hartinger, et al. 2012)

$$P_{th} = \frac{\pi n_0 \omega_0 S_{eff}}{4\eta n_2 D_1 Q^2} \tag{3.4}$$

where the pump power is inversely proportional to the $FSR = D1/2\pi$, and follows inverse-square law with the qualify factor $Q = \omega_0/\kappa$. At the same time, the mode number of the primary sidebands can be derived as a result of the dispersion, loss rate, and the ratio between pump power and threshold (Herr, Hartinger, et al. 2012),

$$m = \sqrt{\frac{\kappa}{D_2}(\sqrt{\frac{P_{in}}{P_{th}} - 1} + 1)} \tag{3.5}$$

3.4 Lugiato-Lefever equation

While coupled mode equations are used to describe the microcombs dynamics in the frequency domain, it is also natural to consider the microcomb evolution in the time domain by applying discrete Fourier transform,

$$A(\phi, t) = \sum_{\mu} a_{\mu}(t) e^{i\mu\phi} \tag{3.6}$$

where $A(\phi, t)$ is the overall optical amplitude at the azimuthal angle ϕ in the microresonator. Its evolution over time can be obtained by substituting Equation 3.6 into Equation 3.3 (Chembo and Menyuk 2013),

$$\frac{dA(\phi, t)}{dt} = i\frac{D_2}{2}\frac{\partial^2 A}{\partial \phi^2} + ig|A|^2 A - i\delta\omega A - \frac{\kappa}{2}A + f \tag{3.7}$$

where δ_{ω} is the resonance-pump detuning and D_2 is the cavity dispersion. This is the same form as the Lugiato-Lefever equation (LLE) (Lugiato and Lefever 1987).

3.5 Approximated solutions of soliton microresonator frequency combs

No exact solutions are known to Equation 3.7. However, an analytical stationary solution ($dA/dt = 0$) can be derived in the absence of loss and pump gain ($\kappa, f = 0$),

$$\frac{dA(\phi, t)}{dt} - i\frac{D_2}{2}\frac{\partial^2 A}{\partial \phi^2} - ig|A|^2 A + i\delta\omega A = 0 \tag{3.8}$$

with a soliton solution in the hyperbolic secant form,

$$A = B\text{sech}(\frac{\phi}{\phi_{\tau}}) \tag{3.9}$$

where B is the soliton amplitude and ϕ_{τ} is the pulse width in the azimuthal coordinate.

In real time frame, the pulse width is $\tau_s = \phi_\tau / D_1$ Although the pump and loss are not considered, it is still beneficial to plugging the unperturbed soliton solution Equation 3.9 into Equation 3.8 and understand how the dispersion, nonlinearity, and detuning affects the soliton properties,

$$(\frac{D_2}{2\phi_\tau^2} - \delta\omega) + (gB^2 - \frac{D_2}{\phi_\tau^2})\text{sech}^2(\phi/\phi_\tau) = 0 \tag{3.10}$$

which gives relations of,

$$\frac{D_2}{2\phi_\tau^2} = \delta\omega \tag{3.11}$$

$$gB^2 = \frac{D_2}{\phi_\tau^2} \tag{3.12}$$

It can understood that in a stationary soliton state, a portion of the cavity dispersion can be compensated by the cavity detuning, and the rest of dispersion can be balanced by the cavity Kerr nonlinearity. Also, Equation 3.12 and Equation 3.11 indicate that an anomalous cavity dispersion $D_2 > 0$ and red-detuned regime $\delta\omega = \omega_0 - \omega_p > 0$ are required for bright soliton existence in the cavity.

For the case including the cavity loss and pump gain, one can treat them as a perturbation and calculate approximated analytical solutions using Lagrangian variation method (Andrey B Matsko and Maleki 2013; Herr, Brasch, et al. 2014; Yi, Q.-F. Yang, K. Y. Yang, and Kerry Vahala 2016). The ansatz of Equation 3.7 is,

$$A(\phi, t) = B\text{sech}(\phi/\phi_\tau)e^{i\varphi} \tag{3.13}$$

where φ is the phase of soliton envelope relative to the pump. The Lagrangian method gives relation of

$$B = \sqrt{\frac{2\delta\omega}{g}} \tag{3.14}$$

$$\phi_\tau = \sqrt{\frac{D_2}{2\delta\omega}} \tag{3.15}$$

$$cos\varphi = \frac{\kappa B}{\pi f} = \sqrt{\frac{2\delta\omega}{g}}\frac{\kappa}{\pi f} \tag{3.16}$$

It can be seen that the soliton amplitude and pulse width is a function of detuning that can be controlled in experiment, but their product $B\phi_\tau = \sqrt{\frac{D_2}{g}}$ is a fixed value that is determined by the cavity dispersion and nonlinear coefficients. While the first two relations are equivalent to the Equation 3.11 and Equation 3.12 that are calculated under no pump and loss assumption, the Lagrangian method gives the third relation which sets a maximum detuning of (considering $|\cos\varphi| \leq 1$),

$$\delta\omega \leq \frac{g\pi^2 f^2}{2\kappa^2} \tag{3.17}$$

The maximum detuning range is a function of the normalized pump field f. In experiment, when the detuning is larger than the maximum value $\delta\omega_{max} = g\pi^2 f^2/2\kappa^2$, the soliton is no longer a solution to the LLE equation and cannot maintain in the cavity.

3.6 Numerical simulation methods

The numerical simulations of the microcombs dynamics can be done with either coupled mode equations using fourth-order Runge–Kutta method (Chembo and N. Yu 2010; Hansson, Modotto, and Wabnitz 2014)n, or LLE equation with split-step Fourier method (G. P. Agrawal 2007; Chembo and Menyuk 2013). Both methods can be equally efficient when considering the nonlinear (Kerr nonlinearity) evolution in time domain and linear evolution (dispersion, loss) in frequency domain. In this section, the split-step Fourier method is provided.

Usually, it is preferred to normalized the LLE equation to simulate a class of cases with different parameters. Here, it can be done by taking $t = 2\tau/\kappa$, $\phi = \sqrt{2D_2/\kappa}\theta$ and $A = \sqrt{\kappa/2g}\psi$, where τ, θ and ψ are the normalized time, azimuthal angle and optical field (Herr, Brasch, et al. 2014),

$$\frac{d\psi(\theta,\tau)}{d\tau} = \frac{i}{2}\frac{\partial^2\psi}{\partial\theta^2} + i|\psi|^2\psi - (i\zeta + 1)\psi + \tilde{f} \tag{3.18}$$

where $\zeta = 2\delta\omega/\kappa$ and $\tilde{f} = \sqrt{8g/\kappa^3}f$ are the normalized detuning and pump field. $|\tilde{f}|^2$ corresponds to the threshold power of parametric oscillation in Equation 3.4.

Considering a small time step $\Delta\tau$, the field evolution from $\psi(\theta,\tau)$ to $\psi(\theta,\tau+\Delta)$ can be divided into three steps:

Step 1: Calculate the Kerr nonlinearity in time domain by $\Delta\tau$ by using equation

$$\frac{d\psi(\tau)}{d\tau} = i|\psi|^2\psi \tag{3.19}$$

which gives

$$\psi_N(\tau + \Delta\tau) = e^{i|\psi|^2 \Delta\tau} \psi(\tau) \tag{3.20}$$

Step 2: Calculate the dispersion, damping (loss), and detuning in frequency domain using the Fourier transform of Equation 3.18

$$\frac{d\tilde{\psi}(\tau)}{d\tau} = -i\frac{\mu^2}{2}\tilde{\psi} - (i\zeta + 1)\tilde{\psi} \tag{3.21}$$

where we have used the property of the discrete Fourier transform $FFT(\frac{i}{2}\frac{\partial^2\psi}{\partial\theta^2}) = -i\frac{\mu^2}{2}FFT[\psi(\theta,\tau)]$. Then it gives

$$\psi_D(\tau + \delta\tau) = IFFT[e^{-(1+i\zeta+i\frac{\mu^2}{2})\Delta\tau} FFT[\psi_N(\tau + \Delta\tau)]] \tag{3.22}$$

Step 3: Calculate the pump term in time domain

$$\psi(\tau + \Delta\tau) = \psi_D(\tau + \delta\tau) + \tilde{f}\Delta\tau \tag{3.23}$$

Repeating the steps above, one can simulate the comb dynamics over time based on LLE equation. Note that proper seeding is required to initiate the modulation instability. For example, one can set half photon in each mode as the seeding to mimic the quantum noise in the cavity. Depending on the number of optical modes and the number of time steps, the simulation take from a minute to a few hours. For example, 200 modes with 1 million time steps can take about one minute on a personal computer.

Chapter 4

High-power, high-coherence 100GHz mmWave generation using integrated microcombs and high-speed photodiodes

4.1 Introduction

The millimeter-waves (mmWaves) technology has gained tremendous interest in recent years thanks to the increasing demand in wireless communications, radar, sensing, and imaging. (Cooper et al. 2008; Kleine-Ostmann and Nagatsuma 2011; Koenig et al. 2013). Photonic microwave technology provides an attractive solution thanks to its wide bandwidth, low power dissipation, and remoting through low-loss fiber. However, the performance of power and coherence for photonic mmWave systems, e.g. heterodyne detection of two lasers, are being held back fundamentally at high frequencies by (1) the power roll-off of photodiodes associated with the photodiode's bandwidth, and (2) the inability to stabilize laser beat note due to the high frequency.

The recent development of dissipated Kerr solitons in microresonators(Herr, Brasch, et al. 2014; Yi, Q.-F. Yang, K. Y. Yang, Suh, et al. 2015; Brasch et al. 2016; Gong et al. 2018; Gaeta, Lipson, and Tobias J Kippenberg 2019; He et al. 2019) provides an integrated solution to address the challenges of photonic-generated mmWaves in both power and coherence. These solitary wave packets achieve mode-locking by leveraging Kerr nonlinearity to compensate cavity loss and to balance chromatic dispersion (Herr, Brasch, et al. 2014; Tobias J Kippenberg, Gaeta, et al. 2018). Microresonator solitons have been applied to metrology (Spencer et al. 2018), optical communications (Marin-Palomo et al. 2017) and spectroscopy(Suh, Q.-F. Yang, et al. 2016; Dutt et al. 2018) in the form of microresonator-based frequency combs (microcombs)(Del'Haye et al. 2007). Due to the miniaturized dimension, the repetition rate of microresonator solitons ranges from a few GHz to THz (Suh and Kerry Vahala 2018; Q. Li et al. 2017). Direct detection of the solitons with a fast photodiode produces mmWave at the repetition frequency of the solitons. When compared with the conventional two laser heterodyne detection method, the soliton mode-locking provides up to 6 dB gain in mmWave output due to the constructive interference among beatnotes created by different pairs of neighboring comb lines (Kuo et al. 2010). This additional gain is of great importance at high frequencies, since it can relax the bandwidth requirements in the photodiode. In terms of signal coherence, recent studies have shown that the phase noise of the soliton repetition frequency at 10's of GHz can be orders of magnitude smaller than that of its pump laser (Liang et al. 2015; Yi, Q.-F. Yang, K. Y. Yang, Suh, et al. 2015; Yi, Q.-F. Yang, Xueyue Zhang, et al. 2017; J. Liu, Lucas, et al. 2020). When microresonator solitons are married with integrated lasers (Stern et al. 2018; Xiang, W. Jin, et al. 2020), amplifiers (Beeck et al. 2020), and high-speed photodiodes (Q. Yu et al. 2020) through heterogeneous or hybrid integration, a fully integrated mmWave platform can be created with high power, high coherence performance and the potential for large scale deployment through mass production (Fig.

4.1).

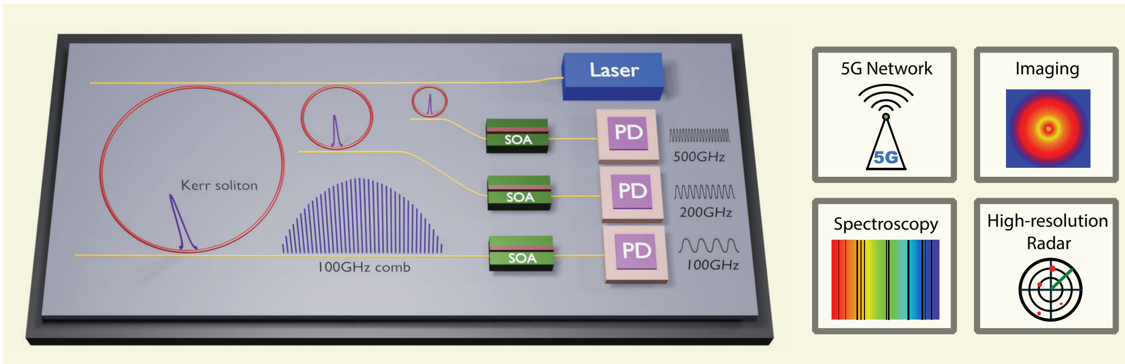

Figure 4.1: **Artistic conceptual view of fully integrated mmWave platform based on microresonator solitons.** The microresonator solitons are generated by pumping a high-Q Kerr microresonator with a continuous-wave (cw) laser. Photodetecting the solitons generates the mmWave signal at the soliton repetition frequency (comb spacing). Soliton mode-locking can provide up to 6 dB more power than that of conventional two laser heterodyne detection, and it is also capable of reducing the mmWave linewidth. By leveraging advances in photonic heterogeneous integration, all critical components, including pump laser, semiconductor optical amplifiers (SOAs) and ultrafast photodiodes (PDs), can potentially be integrated with the Kerr microresonators on the same chip. The integration will enable arrays of coherent mmWave sources, which can generate mmWave signals over a broad range of frequencies. Such a mmWave platform can advance applications in high-speed wireless communication, sub-THz imaging and spectroscopy, and high resolution ranging.

In this chapter, we demonstrated high power, high coherence photonic mmWave generation at 100 GHz frequency through the combination of integrated microresonator solitons and a modified uni-traveling carrier photodiode (MUTC PD). A 5.8 dB increase of mmWave power is obtained by using microresonator solitons when comparing to the output power of conventional heterodyne detection. Importantly, the power level we achieve with microresonator solitons is approaching the theoretical limit of heterodyne detection, which assumes an ideal photodiode with zero power roll-off in its frequency response. The system also achieves a maximum mmWave power of 7 dBm, one of the highest powers ever reported at 100 GHz (K. Sun and Andreas Beling 2019). For our free-running system, the 100 GHz signal has Lorentzian and

Gaussian linewidth of 0.2 kHz and 4.0 kHz, respectively, which is two orders of magnitude smaller than that of the pump laser. The dependence of output power on the number of comb lines and chromatic dispersion is carefully studied both theoretically and experimentally. Our demonstration paves the way for a fully integrated photonic microwave system with soliton microcombs and high-speed photodiodes.

4.2 100 GHz soliton generation

The dissipated Kerr solitons used in this work are generated in an integrated, bus-waveguide coupled Si_3N_4 micro-ring resonator. The resonator has a free spectral range (FSR) of $\sim$100 GHz, and an instrinsic quality factor of 2.6×10^6 and loaded quality factor of 2.2×10^6. The SiN resonator has a cross-section, width$\times$height, of 1.65×0.8 μm^2, and is coupled to a bus-waveguide of the same cross-section. The resonator radius is 0.24 mm, and the soliton-generation mode has anomalous dispersion of ~ 1 MHz/FSR. A thermoelectric cooler (TEC) is placed beneath the microresonator to coarsely overcome the environmental temperature fluctuations. To generate a single soliton state, a rapid pump laser frequency scanning method (J. R. Stone et al. 2018) is applied to overcome the thermal complexity when accessing the red-detuned soliton existence regime. The detailed experimental setup is shown in Fig. 4.2. The pump laser is derived from the first phase modulated sideband of a continuous wave laser, and the sideband frequency can be rapidly tuned by a voltage controlled oscillator (VCO). The pump laser scans its frequency at the speed of $\sim$20 GHz/μs, and the scan is stopped immediately once the pump laser frequency reaches the red-detuned regime of the resonator. The pump power in the waveguide is 1 Watt, which could be reduced in the future by 2 orders of magnitude through improving the quality factor and minimizing the thermal effect (J. Liu, Raja, et al. 2018) The single soliton state with a 35.4 fs pulse width is generated and its squared hyperbolic secant spectral envelope is characterized by an optical spectrum analyzer (Fig. 4.3**a**).The optical spectrum has a 3-dB bandwidth of 5.4 THz, which contains a sufficient number of comb lines for photodetection.

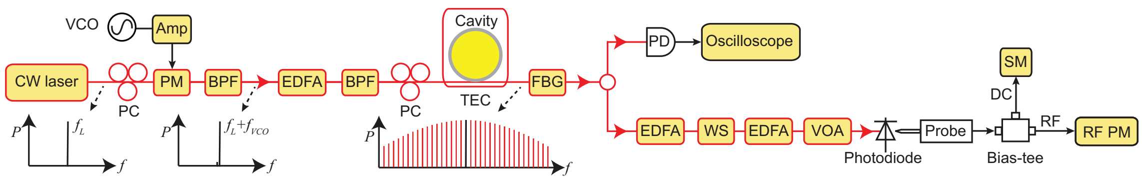

Figure 4.2: **Experimental setup.** The microresonator solitons are generated in a SiN resonator which is coarsely temperature controlled by thermoelectric cooler (TEC). The pump laser is the first modulation sideband of a phase modulated (PM) continuous wave (cw) laser, and the sideband frequency can be rapidly tuned by a voltage controlled oscillator (VCO). The frequencies of the cw laser and phase modulation are f_L and f_{VCO1}, respectively. The pump laser is then amplified by an erbium-doped fiber amplifier (EDFA), and the amplified spontaneous emission noise is filtered out by a bandpass filter (BPF). At the output of the resonator, a fiber-Bragg grating filter is used to suppress the pump. The microresonator solitons are then amplified, dispersion compensated by a waveshaper (WS), and sent to the photodiode. The configuration also includes polarization controllers (PC), variable optical attenuator (VOA), source meter (SM), and RF power meter (RF PM).

4.3 Photodetection of soliton microcombs using MUTC-PD

The solitons are coupled from the SiN on-chip bus waveguide into a lensed fiber. Before reaching the MUTC-PD, the soltion comb is amplified to > 200 mW by an erbium-doped fiber amplifier (EDFA), and a variable optical attenuator is used to precisely control the illumination power. An optical programmable waveshaper (WS) is used to compensate the group velocity dispersion and to suppress spontaneous emission (ASE) noise from the EDFA. The inset of Fig. 4.3**a** shows the optical spectrum after the amplification and dispersion compensation. Finally, the solitons are coupled to the surface normal modified uni-traveling carrier photodiode (MUTC PD) through a 8 μm collimated fiber. Pictures of the microresonator and a PD die are shown in Fig. 4.3**b** and Fig. 4.3**c**, respectively. The MUTC PDs used in this work are from Andreas Beling's group at UVA.

4.4 Power measurements

In this section, the mmWave power generated using soliton/heterodyne detection is investigated, including the power enhancement from the soliton combs, the power dependence on the number of comb lines/dispersion/comb spectral envelope, and the maximum power obtained from soliton detection.

4.4.1 6dB power enhancement

In conventional heterodyne detection, mmWaves are generated when two laser lines mix with each other on a photodiode and create one beat note. However, when using an optical frequency comb, each comb line will beat with its two adjacent neighbour lines to create beatnotes at the comb repetition frequency. For a comb that consists of N comb lines, $(N-1)$ beat notes will be created at the comb repetition frequency. Therefore, for the same average optical power, the comb can produce up to twice the number of beatnotes per laser line than heterodyne detection, and thus generate twice the AC photocurrent. The output power from the photodiode at the comb repetition frequency can be described as Urick, Williams, and McKinney 2015; Kuo et al. 2010:

$$P_{PD} = \frac{I_{DC}^2 R_L}{2} \left[\frac{2(N-1)}{N}\right]^2 \times \Gamma, \tag{4.1}$$

where I_{DC} is the average photocurrent, R_L (50 Ω) is the load resistor, and $N \geq 2$ is the number of comb lines. Γ is the measured relative mmWave power roll-off for the photodiode, and is $\sim$ 5.5 dB for the 7 μm and $\sim$ 6 dB for the 8 μm diameter PDs used in this work at 100 GHz. Clearly, the power at the limit of $N \rightarrow \infty$ is 4 times (6 dB) higher than the power of heterodyne detection, where $N = 2$.

To characterize the 6 dB power increase from the microresonator solitons, the PD output powers are measured for both microresonator soliton detection and heterodyne detection on four of our PDs with 7, 8, 10, and 11 μm diameters. The heterodyne measurements are performed using two continuous-wave lasers with the same optical power and polarization. A variable optical attenuator is used to control the optical power illuminating on the PD. In the linear region of PD operation, the 100 GHz mmWave powers at different photocurrents are shown in Fig. 4.3**d** for the 7-μm device. The DC photocurrent is a direct measurement of the optical power illuminating on the PD. In the experiment, the coupling distance from fiber to PD is increased for a uniform illumination, resulting in 1 mA photocurrent for 11 mW optical input power. The mmWave power generated from the microresonator solitons is measured to be 5.8 dB higher than that of heterodyne detection. This power increase is approaching the 6 dB theoretical limit, and is verified on all four PDs with different diameters (shown in the inset of Fig. 4.3**d**). As a result of the 6 dB power increase, the mmWave power generated using microresonator solitons is within 1 dB of the theoretical power limit of heterodyne detection (solid black line in Fig. 4.3**d**), where the detector is assumed to be ideal and has no power roll-off at mmWave frequency. It shall be noted that no optical spectrum flattening is applied in our measurement. For 5.8 dB power improvement, a 3 dB bandwidth of 7 comb lines is required for the Sech^2 or Gaussian spectral envelope.

4.4.2 Power dependence on the number of comb lines

Next, we verify the dependence of mmWave power increase on the number of comb lines, which is described in Equation 4.1. A line-by-line waveshaping filter is used to select the number of comb lines that pass to the MUTC PD. We test the number of comb lines from 2 to 22 at four different photocurrent levels (optical power), and the result is shown in Fig. 4.4**a**. Three representative optical spectra for 2, 12, and 22 comb lines are shown in Fig. 4.4**b**. The measured mmWave power follows the calculated curves. Interestingly, a 3 or 5 dB increase of power only requires 4 or 9 comb lines. This relatively small demand for comb lines relaxes the microresonator soliton requirement in terms of its optical bandwidth.

4.4.3 Dispersion effect on power

The increase of mmWave power only happens when the beatnotes generated by different pairs of comb lines are in constructive interference. This is not always the case if there is dispersion between the microresonator and the PD. This effect is studied by applying programmable dispersion using a waveshaper. The measurement of mmWave power versus waveshaper dispersion is shown in Fig. 4.4**c**. The effect can be calculated analytically by adding phase to each comb line, and will modify Equation 4.1 to:

$$P_{PD} = \frac{I_{DC}^2 R_L}{2} \left[\frac{2\sin\left[(N-1)\pi c d f_r^2/f_p^2\right]}{N\sin\left[\pi c d f_r^2/f_p^2\right]} \right]^2 \times \Gamma, \tag{4.2}$$

where c is the speed of light, and $d = d_0 + d_c$ is the accumulated group velocity dispersion between the microresonator and PD. d_0 denotes the offset dispersion in the system introduced by fibers and amplifiers, and d_c represents the dispersion compensation added by the waveshaper. The derivation of Equation 4.2 is shown at the end of this subsection. The measurement and theory prediction agree very well when an offset dispersion of $d_0 = 1.95$ ps/nm is included. The offset dispersion exists in our system because of the 70 meter fiber used to connect the microcomb lab and photodetector lab (contributing 1.26 ps/nm), with the rest of the dispersion coming from the fibers in the EDFA. N is used as a free parameter for fitting the experimental curve, and $N = 15$ is used for the dashed line in Fig. 4.4**c**. The fitted N should be interpreted as the effective number of comb lines to account for the spectral envelope shape. When the entire system is fully integrated, the overall length of waveguides will be well below a meter, and the dispersion will not impact the mmWave power.

Here, the derivation of Equation 4.2 is given. Consider optical pulses propagating in an optical fiber will acquire additional phase due to group velocity dispersion in the fiber. If we suppose the center frequency of the pulse is ω_p, then the component at frequency ω will acquire a relative phase after propagation of distance z (G. P. Agrawal 2007):

$$E(z,\omega) = E(0,\omega)\exp[-i\frac{D_\lambda \lambda^2}{4\pi c}(\omega-\omega_p)^2 z] + c.c., \tag{4.3}$$

where $E(0,\omega) = E_0/\sqrt{2N}\exp(-i\omega t)$ is the electrical field of light at frequency ω and position $z = 0$, normalized to the photon number per unit time. Here we have assumed a flat spectrum for the comb, and N as the total number of comb lines. D_λ is the group velocity dispersion parameter, and $D_\lambda \approx 18$ ps/nm/km for SMF-28 fiber at 1550 nm. For soliton frequency combs, $(\omega - \omega_p)/2\pi = n \times f_r$ for the n-th comb line from the spectral envelope center, where f_r is the comb repetition frequency. Therefore, the photocurrent generated in the photodiode is

$$\begin{aligned} I \equiv I_{DC} + I_{AC} = |E|^2 &= |\sum_{-N_0}^{N_0} E(0,\omega)\exp[\frac{-i\pi c f_r^2}{f_p^2} n^2 D_\lambda z] + c.c.|^2 \\ &= |E_0|^2 + |E_0|^2 \frac{2\sin\left[(N-1)\pi c D_\lambda z f_r^2/f_p^2\right]}{N\sin\left[\pi c D_\lambda z f_r^2/f_p^2\right]}\cos(2\pi f_r t) + ..., \end{aligned} \tag{4.4}$$

where we have used the $\sum_{k=m}^{n} ar^k = a(r^m - r^{n+1})/(1-r)$ to derive the term of $\cos(2\pi f_r t)$, and we have set $2N_0 + 1 = N$. Higher harmonics of the repetition frequency are neglected as they are beyond the detection limit of our photodiode. Considering I_{DC} as the average photocurrent flowing through the load resistor R_L, the detected mmWave power at frequency f_r is yielded as:

$$P_{f_r} = \frac{I_{DC}^2 R_L \Gamma}{2}\left[\frac{2\sin\left[(N-1)\pi c d f_r^2/f_p^2\right]}{N\sin\left[\pi c d f_r^2/f_p^2\right]}\right]^2, \tag{4.5}$$

where we have defined $d = D_\lambda z$ as accumulated dispersion, and Γ is the PD power roll-off at the repetition frequency. This equation is the same as equation Equation 4.2.

When dispersion is very small ($d \to 0$), the detected mmWave power approximates to

$$P_{f_r} = \frac{I_{DC}^2 R_L \Gamma}{2}\left[\frac{2(N-1)}{N}\right]^2, \tag{4.6}$$

which is Equation 4.1.

4.4.4 Power versus optical spectral envelope

In this subsection, we calculate the impact of the optical spectral envelope on the mmWave power. For simplicity, we assume that the optical envelope is symmetric along the envelope center, and we assume no accumulated dispersion. For the n-th comb line, we have:

$$E(\omega_n) = f(n)\frac{E_0}{\sqrt{2N}}e^{-i\omega_n t} + c.c., \tag{4.7}$$

where function $f(n)$ is real and it describes the spectral envelope. We focus on the case where the number of comb lines is large, so that we can assume the envelope is smooth, and $|f(n+1) - f(n)| \ll f(n)$. The photocurrent is then expressed as:

$$\begin{aligned} I = |E|^2 = |\sum_{-N_0}^{N_0} f(n)\frac{E_0}{\sqrt{2N}}e^{-i\omega_n t} + c.c.|^2 = \frac{|E_0|^2}{N}\sum_{-N_0}^{N_0} f^2(n) \\ + \frac{2|E_0|^2}{N}\cos(2\pi f_r t) \times \sum_{n=-N_0}^{N_0-1} f(n)f(n+1) + ..., \end{aligned} \tag{4.8}$$

where we have neglected higher harmonics of the repetition frequency again. The sum can be simplified by using the symmetric envelope condition, $f(-n) = f(n)$, and we can substitute $f(n+1) = f(n) + \Delta f(n+1/2)$, where $\Delta f(n+1/2)$ is the difference between $f(n+1)$ and $f(n)$, and $\Delta f(x)$ is an odd function. Therefore, we have:

$$
\begin{aligned}
\sum_{n=-N_0}^{N_0-1} f(n)f(n+1) &= \sum_{n=-N_0}^{N_0} f(n)f(n+1) - f(N_0)f(N_0+1) \\
&= \sum_{n=-N_0}^{N_0} f(n)\left[f(n) + \Delta f(n+1/2)\right] - f(N_0)f(N_0+1) \\
&= \sum_{n=-N_0}^{N_0} f^2(n) + \sum_{n=-N_0}^{N_0} f(n)\Delta f(n+1/2) - f(N_0)f(N_0+1) \\
&\approx \sum_{n=-N_0}^{N_0} f^2(n) - f(N_0)f(N_0+1),
\end{aligned}
\tag{4.9}
$$

where we have used $f(n)\Delta f(n+1/2)$ approximated to an odd function when the spectrum is broad, and thus $|f(n+1) - f(n)| \ll f(n)$, and $\Delta f(n+1/2) \approx \Delta f(n)$. It is clear that when N and N_0 are very large, the sum is dominated by the total optical power, $\sum_{n=-N_0}^{N_0} f^2(n)$, and is almost irrelevant to the function of the envelope. The mmWave power can be expressed as:

$$
P_{f_r} = \frac{I_{DC}^2 R_L}{2}\left[2 - \frac{2f(N_0)f(N_0+1)}{\sum_{-N_0}^{N_0} f^2(n)}\right]^2. \tag{4.10}
$$

When $N_0 \to \infty$, $f(N_0)f(N_0+1) \ll \sum_{-N_0}^{N_0} f^2(n)$, and the power gain relative to the heterodyne detection approaches 6 dB regardless of the spectral envelope $f(n)$. It shall be noted that this result only applies to the case where the spectral envelope is symmetric and smooth, otherwise the approximation used in Equation 4.9 will fail.

4.4.5 Measuring maximum mmWave power

We obtain a maximum output power of 7 dBm at 22.5 mA for the 8 μm device shown in Fig. 4.5**a**, due to the optimized light coupling from the size match of the 8 μm spot-size collimated fiber and diameter of the PD's absorber. Using equation (1) we find that the ideal heterodyne response for this 8 μm device would need 26.7 mA to achieve 7 dBm, which means we can produce the same power at lower average photocurrent using soliton excitation. The 7 dBm saturation power is recorded at -3.6 V bias. Increasing the reverse bias can improve the saturation power, however, ultimately this can cause PD thermal failure (X. Xie et al. 2015), which is due to the raise in junction temperature from the dissipated power in the PD (reverse bias × average photocurrent). One advantage of using solitons is that they can generate the same RF output power at a lower photocurrent than the two-laser heterodyne method, and thus can reduce the dissipated power and allow the PD to be operated further below the point of thermal failure.

4.5 Coherence measurements

In this section, the mmWave coherence performance is investigated with measurements including linewidth, phase noise, and Allan deviation.

4.5.1 Linewidth reduction

The electrical spectrum of the 100 GHz mmWave signal is measured and shown in Fig. 4.3**e**. Limited by the available bandwidth of our electrical spectrum analyzer, we down convert the 100 GHz mmWave by sending it to an RF mixer to mix it with the fifth harmonic of a 20.2 GHz local oscillator. The mixer generates a difference frequency at $\Delta f = 5f_{LO} - f_r$. Δf is measured to be 1.2410 GHz, and we can derive the mmWave frequency as $f_r = 99.7590$ GHz. A low-noise, narrow signal is clearly observed at 3 kHz resolution bandwidth (RBW) in Fig. 4.3**e** (red trace). The signal is fitted with a Lorentzian, and the 3-dB bandwidth is 0.2 kHz (zoomed-in panel in Fig. 4.3**e**). Note that the soliton repetition rate is subject to fluctuations (laser frequency drift, temperature, etc.), and the central part of the signal is Gaussian with 3-dB linewidth of 4 kHz. This narrow linewidth at 100 GHz frequency is obtained for a free-running microcavity soliton, which is driven by a pump laser with significantly broader linewidth ($\sim$ 200 kHz, New Focus 6700 series specification). We note that there are a few bumps around 50 kHz offset frequency, which are likely to be derived from the technical noise of the pump laser. To compare the signal coherence between conventional heterodyne method and the soliton method, the heterodyne signal of beating the pump laser and another 6700 series New Focus laser is also measured and shown in Fig. 4.3**e** (blue trace). At the same RBW, the heterodyne signal has poor coherence and its frequency is drifting $>$ 5 MHz. Our measurements show that using free-running microcavity solitons can reduce the linewidth of mmWave signals by 2 orders of magnitude, giving the microresonator soliton platform a key advantage over conventional heterodyne detection. No RF reference is used to stabilize the mmWave; in fact, the only controls used are the coarse temperature controls of the laser and the microresonator, used to offset the change in environmental temperature.

Our observation of linewidth reduction is in agreement with previous reports of microresonator solitons at X- and K-band repetition frequencies Yi, Q.-F. Yang, Xueyue Zhang, et al. 2017; J. Liu, Lucas, et al. 2020. The soliton repetition frequency equals to the cavity free-spectral range (FSR) at the wavelength of soliton spectral envelope center. Both Raman self-frequency shift Maxim Karpov et al. 2016 and dispersive wave recoils can affect the soliton envelope center wavelength Brasch et al. 2016; Yi, Q.-F. Yang, Xueyue Zhang, et al. 2017, and they are functions of laser-cavity frequency detuning. This can be clearly seen in Fig. **??a**, as our soliton's envelope center is to the red side of the pump laser. Because of the chromatic dispersion, the FSR at different wavelengths is different, and thus the variation of the pump laser frequency, f_p, will alter the soliton spectral envelope center, and change the soliton repetition rate, f_r. To the first order, the transfer of frequency variation from the pump (δf_p) to the repetition rate (δf_r) can be described as $\delta f_r = \frac{\partial f_r}{\partial f_p} \times \delta f_p$, where δ denotes the variation. For both silica and silicon nitride resonators Yi, Q.-F. Yang, Xueyue Zhang, et al. 2017; Bao, Xuan, et al. 2017, this transfer coefficient $\frac{\partial f_r}{\partial f_p}$ has been measured to be on the level of 10^{-2}, and thus the soliton repetition rate linewidth is much smaller than that of the pump laser.

4.5.2 Phase noise reduction

We further characterize the phase noise of the mmWaves generated from the free-running microcavity solitons, and compare it to the phase noise from the heterodyne method. Similar to the linewidth measurement, the 100 GHz mmWave signal is down converted in an RF mixer where it is mixed with the fifth harmonic of a 20.2 GHz local oscillator. To minimize the effect of frequency drifting in the phase noise measurement, the frequency of the down-converted signal is further divided down electrically by a factor of 14 and 100 for the soliton and heterodyne, respectively. The phase noise is then measured in the electrical spectrum analyzer with direct detection technique, and the result (at 100 GHz) is shown in Fig. 4.5**b**. Due to the large frequency drift, the heterodyne phase noise below 20 kHz offset frequency cannot be accurately characterized and thus is not presented. The soliton phase noise beyond 100 kHz is potentially limited by the measurement sensitivity, which is set by the noise floor of the spectrum analyzer (dash green), and the phase noise of the local oscillator (Keysight, PSG E8257D) used to down-convert the mmWave (dash black). The measurement shows that the free-running solitons can reduce the mmWave phase noise by $>$ 25 dB from the heterodyne method. The reduction of phase noise from the pump laser frequency to the soliton repetition rate is a result of the noise transfer mechanism in microresonator solitons (Yi, Q.-F. Yang, Xueyue Zhang, et al. 2017). Our observation is in agreement with the previous reports of X-band and K-band microwave generation with microresonator solitons (Yi, Q.-F. Yang, Xueyue Zhang, et al. 2017; J. Liu, Lucas, et al. 2020; Weng et al. 2020). The phase noise of soliton-based mmWaves can be further reduced in the future by using a pump laser with higher stability(Lucas et al. 2020), tuning the soliton into quiet operation point (Yi, Q.-F. Yang, Xueyue Zhang, et al. 2017), and implementing better temperature control of the entire system. For instance, a compact external-cavity diode laser has achieved Lorentzian linewidth of 62 Hz recently(Volet et al. 2018). Using this laser to drive the soliton could further reduce the free-running mmWave phase noise.

4.5.3 Allan deviation reduction

Finally, the Allan deviations of the mmWave generated from the soliton and the heterodyne detection are measured by counting the frequency of the down-converted signal on a zero dead-time counter (Fig. 4.5**c**). At 1 ms gate time, the Allan deviation of the soliton-based mmWave reaches the minimum of $<$ 0.7 kHz, which is more than two orders of magnitude better than that of the heterodyne detection. Above 1 ms gate time, the Allan deviation of the soliton-based mmWave increases due to the drift of pump laser frequency and temperature fluctuation. Stabilizing the mmWave signal to a low frequency reference could provide long term stability, which will increase the system complexity, but is possible through the electro-optics modulation method

(Tetsumoto, Ayano, et al. 2020), or dual microcavity soliton methods (Spencer et al. 2018; B. Wang, Z. Yang, Xiaobao Zhang, et al. 2020).

4.6 Summary

In this chapter, we demonstrated high-power, high-coherence mmWave generation at 100 GHz by using integrated microresonator solitons and MUTC PDs. Extending the frequency to several hundred GHz is possible. For the microresonator solitons, the highest repetition rate reported is 1 THz (Q. Li et al. 2017), while demonstrated MUTC PDs have detection capabilities of at least 300 GHz (A. Beling et al. 2019; Dülme et al. 2019). As the microresonator solitons consume very little pump power, and most of the pump transmits through the waveguide (Yi, Q.-F. Yang, K. Y. Yang, Suh, et al. 2015), it is possible to recycle the pump laser power to drive the next microresonator solitons (Fig. 4.1). Two tandem microresonator solitons driven by the same pump laser have been reported previously (Dutt et al. 2018). The proposed platform has the potential to be fully integrated on a single chip which can enable large-scale mmWave arrays. The four critical components: laser, Kerr microresonator, amplifier, and ultrafast photodiode, have all been shown to be compatible with Si_3N_4 photonic platforms through heterogeneous integration. Once all components are fully integrated, we expect that the platform can deliver a new paradigm regarding scalable, integrated photonics technologies for applications at very high frequencies, and thus provide a path to compact, low-noise high-frequency sources for spectroscopy, ranging, and wireless communications.

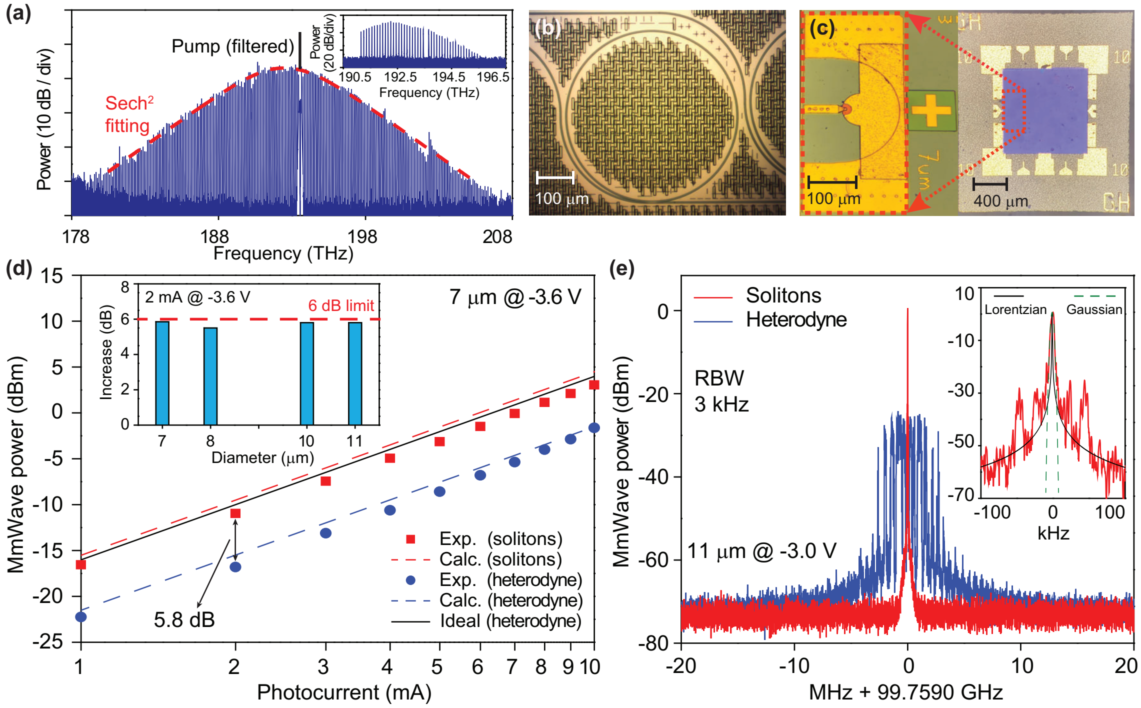

Figure 4.3: **Summary of featured experimental data of 100 GHz mmWave generation.** **(a)** Optical spectrum of single soliton state from the microresonator. The spectrum has sech^2 spectral envelope (fitting shown in dashed red line). The pump laser is suppressed by a fiber Bragg grating filter. Inset shows the optical spectrum of soliton frequency comb after amplification and dispersion compensation. **(b)** Microscopic image of integrated Si_3N_4 microresonator with 100 GHz free spectral range (FSR). **(c)** Microscopic images: front of photodiode die zoomed in on single 7μm device (left), and back of photodiode die flip-chip bonded to aluminum nitride submount (right). **(d)** 100 GHz mmWave output power measured for microresonator solitons (red) and optical heterodyne detection of two cw-lasers (blue). The mmWave output power from the soliton is $\sim$ 5.8 dB more than that of the heterodyne detection at the same photocurrent. Theoretical calculated powers from equation (1) are shown in dashed lines. Particularly, ideal output power from heterodyne detection is illustrated with black solid line, which serves as a theoretical limit of heterodyne detection assuming no PD power roll-off at 100 GHz frequency. The inset shows the power increase by using solitons over optical heterodyne on four devices with different diameters. **(e)** Down-converted electrical spectrum of 100 GHz signal generated with free-running microresonator solitons (red). Inset shows the fitting with Lorentzian (black) and Gaussian (dashed green) lineshapes and the corresponding 3-dB linewidths are 0.2 kHz and 4 kHz respectively. As a comparison, the signal generated from heterodyne method is shown in blue trace. The PD diameter and bias voltage are indicated in each panel.

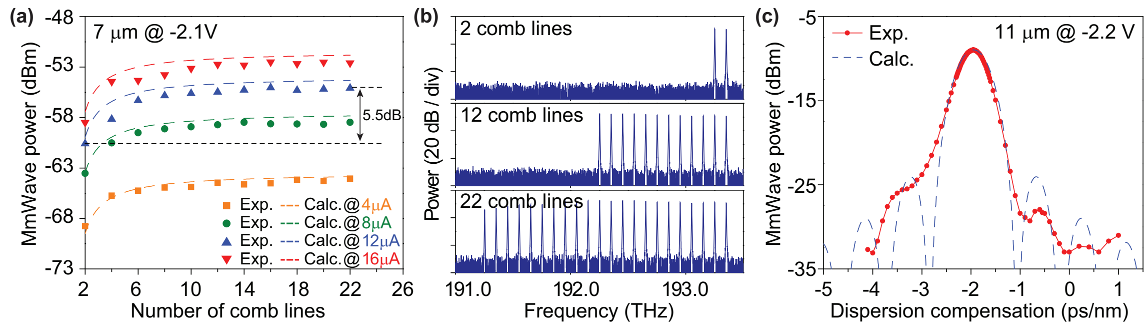

Figure 4.4: **MmWave power versus number of comb lines and dispersion. (a)** MmWave power at 100 GHz for different number of comb lines at four different photocurrents. The measurements agree very well with the theoretical calculation based on equation (1), which are shown in dashed lines. **(b)** Corresponding optical spectra of two, twelve and twenty-two comb line measurements in panel (a). **(c)** MmWave power versus dispersion compensation added by waveshaper, d_c. The maximum output power is reached at $d_c = -1.95$ ps/nm, where the dispersion from fiber and EDFA is completely compensated. A theoretical curve from equation (2) is shown in dashed line and agrees very well with the measurement. The PD diameter and bias voltage are indicated in each panel.

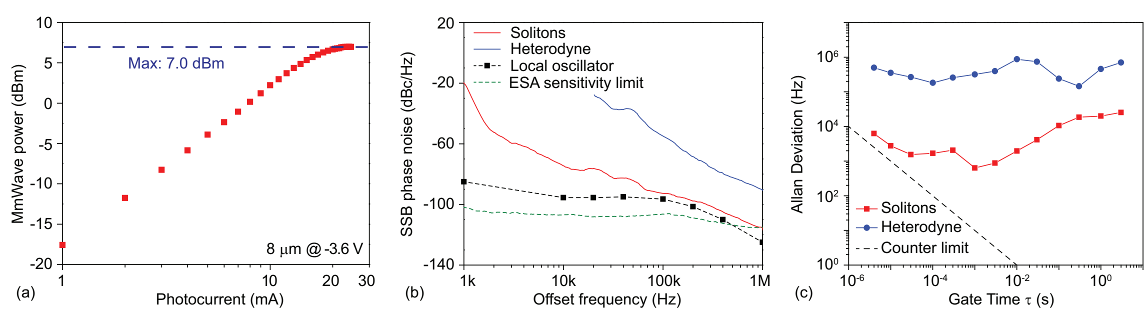

Figure 4.5: **Measurement of mmWave power, mmWave phase noise and Allan deviation. (a)** Maximum power of 7 dBm is reached at 22.5 mA and −3.6 V bias voltage in the $8\mu m$ device. **(b)** Phase noises of the free-running soliton-based mmWave (red) and the heterodyne mmWave (blue) at 100 GHz. The measurement sensitivity floor is set by both the ESA sensitivity limit (dash green), and the local oscillator phase noise (dash black). **(c)** Allan deviation of the free-running soliton-based mmWave (red) and the heterodyne mmWave (blue).

Chapter 5

Integrated optical frequency division for low noise mmWave synthesis

5.1 Introduction

Optical frequency combs provide a way to coherently link radio/microwave-rate electrical signals with optical-rate signals, and they have numerous applications in metrology, time-keeping, and microwave synthesis (Udem, Ronald Holzwarth, and Hänsch 2002; Nathan R Newbury 2011). An important application of optical frequency combs is the optical frequency division (OFD) (Fortier, Kirchner, et al. 2011), where the frequency and phase of optical lasers are coherently divided down by frequency combs to generate microwaves with record-low phase noise (Fortier, Kirchner, et al. 2011; Tetsumoto, Nagatsuma, et al. 2021; Jiang Li and Kerry Vahala 2023). Two of the most critical elements in OFD are (1) reference-cavity stabilized lasers that exhibit excellent fractional frequency stability and (2) optical frequency combs that coherently transfer the phase stability of stabilized lasers to the repetition rate in a laser pulse train. Recent development in ultra-low loss integrated photonics has made both elements possible on a chip(Blumenthal et al. 2018; J. Guo et al. 2022; K. Liu et al.

2022; Tobias J Kippenberg, Gaeta, et al. 2018). This creates a possibility to demonstrate integrated optical frequency division for low-noise microwave and mmWave generation.

In this chapter, we present a demonstration of integrated optical frequency division. The reference lasers with a frequency noise of 0.5 Hz^2/Hz are generated using an integrated high-Q 4-meter coil reference cavity (from Dan Blumenthal's group at UCSB), and the microcombs with 100 GHz rep-rate are generated on an integrated micro-ring resonator. Both are demonstrated on Si_3N_4 platforms.

5.2 Method of integrated optical frequency division

In our approach, the optical frequency division is realized with a ”two-point locking” approach (William C Swann et al. 2011). Two reference laser lines with excellent frequency stability serve as the two locking points. A frequency comb is generated and two of the comb lines are then phase-locked to the reference lasers. As a result, the relative frequency fluctuations between the two locked comb lines are set by the reference lasers. On the other hand, the frequency difference between these two comb lines is equal to the comb rep-rate f_{rep} multiplied by their comb line number difference N. Therefore, the comb rep-rate stability is equal to $1/N$ of the two reference lasers. In another word, the relative frequency stability of two lasers can be coherently divided by the number of comb lines within the two-point locking span. Importantly, a low-noise RF or mmWave signal can be generated by photodetecting the rep-rate of the microcomb on a photodiode using this division method. Assuming a perfect division, the frequency stability and phase noise of the synthesized mmWave is only determined by the reference lasers.

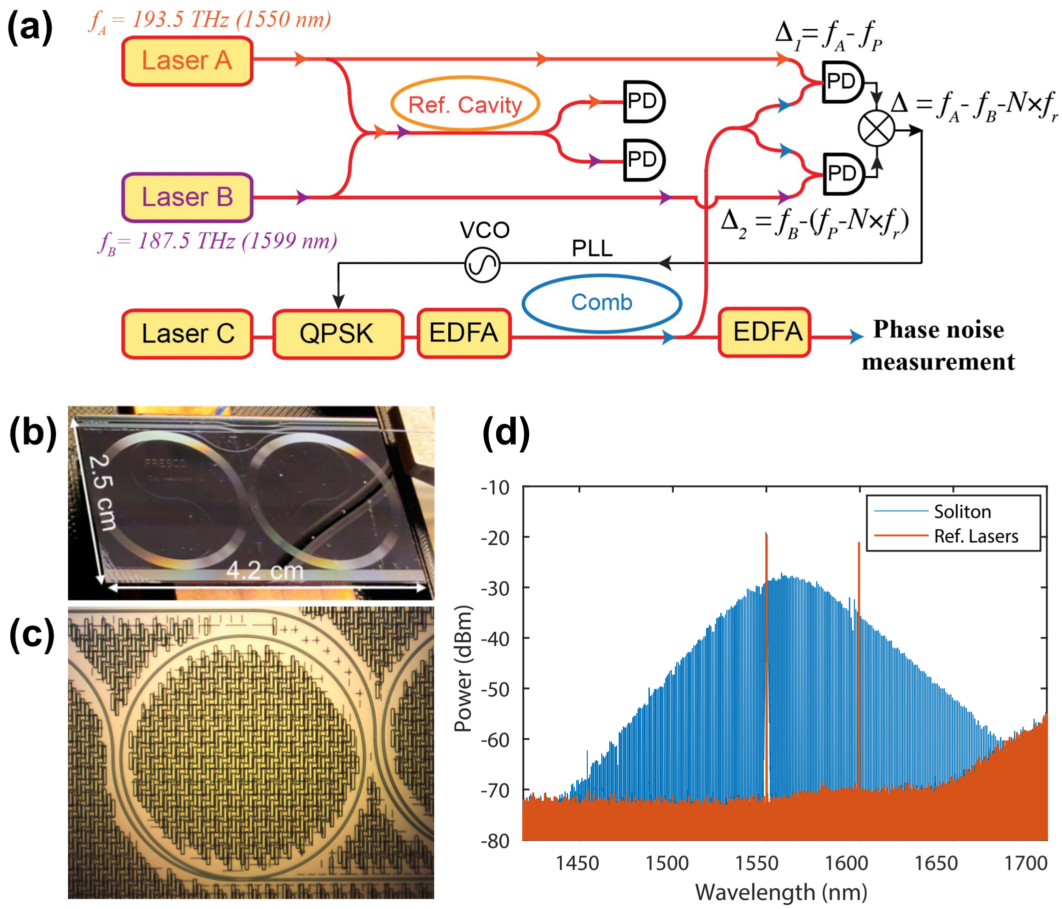

Figure 5.1: **Schematic of integrated optical frequency division.** **(a)** Simplified experimental setup. (b) Image of the integrated 4-meter coil resonator. (c) Image of the integrated micro-ring resonator with 100 GHz FSR. (d) Optical spectra of the soliton microcomb and two reference lasers.

A schematic of our integrated optical frequency division is shown in Fig. 5.1**a**. The two low-noise reference lasers are stabilized to a single high-Q reference cavity. A frequency comb is generated in a micro-ring resonator, and a portion of the comb is used to illustrate the two-point locking optical frequency division, while the rest is sent to the photodiode for producing a mmWave. The details of implementation are provided in the following sections.

5.3 Low-noise reference lasers using an integrated 4-meter coil resonator

In our experiment, the reference lasers are provided by PDH locking two tunable ECDL (NewFocus Velocity TLB-6700) to a single 4-meter-long coil resonator (Fig. 5.1**b**). The wavelengths of reference lasers are 1550 nm and 1600 nm, respectively. The 4-meter coil resonator is fabricated on Si_3N_4 waveguide with a cross-section area of 6 μm $\times$ 80 nm. The FSR of the coil resonator is $\sim$ 50 MHz. The intrinsic quality factors of the coil resonator are measured to be $\sim 40 \times 10^6$ at both C-band and L-band. The PDH locking technique is used to lock the two reference laser frequencies to the resonator mode frequencies by servo control of the cw-laser frequency through laser current modulation. This is implemented by phase-modulating the referenece lasers with electro-optic phase modulators. The modulated reference lasers are then combined using a 50/50 fiber coupler and sent to the coil resonator. After the resonator, the two lasers are separated using a FBG and sent to two photodiodes.

The frequency division ratio N is determined by the ratio between the frequency difference of two reference lasers ($f_A - f_B = 6$ THz) and the frequency comb repetition rate (100 GHz), which gives $N = 60$. Assuming a perfect frequency division, the phase noise reduction through frequency division is $60^2 \sim 35.6$ dB.

5.4 100GHz soliton microcomb generation and OFD implementation

To divide the 6 THz reference laser frequency difference to a 100 GHz mmWave, we generated a 100 GHz soliton microcomb on an integrated, bus-waveguide coupled Si_3N_4 micro-ring resonator (Fig. 5.1**c**) with a free-spectral range (FSR) of 100 GHz. The intrinsic quality factor of the micro-ring resonator is 4.3×10^6. An extended distributed Bragg reflector (E-DBR) laser from Morton Photonics is used to provide high stability to the laser carrier frequency. Then a single-sideband suppressed-carrier modulator is used to derive a rapid scanning pump laser using a voltage-controlled oscillator (J. R. Stone et al. 2018; B. Wang, Z. Yang, S. Sun, et al. 2022). The fast-scanned pump laser can overcome the thermal complexity in the microresonator and generate the single soliton with a power of hundreds of mW after amplification. The optical spectra of the soliton as well as the two reference lasers are shown in Fig. 5.1**d**.

To implement the optical frequency division, two comb lines ($m-$th and $n-$th) are selected using optical filters, and beat with the two reference lasers (f_1 and f_2) on the photodiodes (NewFocus 1811-FC). A L-band EDFA is used to amplify the comb line power at 1600nm, so that it can provides enough electrical power to the beatnote generated from the photodiode. The beatnote frequencies are $\Delta_1 = f_1 - (f_p + m f_{rep})$ and $\Delta_2 = f_2 - (f_p + n f_{rep})$. The two beatnotes are then mixed on an electrical frequency mixer with an output frequency of $\Delta = \Delta_1 - \Delta_2 = f_1 - f_2 + (n - m) f_{rep}$. It can be seen that the pump laser frequency noise is canceled out in the mixer output signal. Then the signal Δ is phase-locked to a stable reference frequency local oscillator (Keysight E8257D) through the servo control of the VCO (which controls the pump laser frequency and then translates to the comb rep-rate). Assuming a perfect phase-locking, the phase of comb rep-rate is given by $\phi_{rep} = (\phi_1 - \phi_2 - \phi_{LO})/(m-n)$, and its phase noise (power spectral density) is given by $S_\phi^{rep}(f) = (S_\phi^1 - S_\phi^2 - S_\phi^{LO})/(m-n)^2 \sim (S_\phi^1 - S_\phi^2)/(m-n)^2$ considering the phase noise of the local oscillator S_ϕ^{LO} is much lower than that of the ref laser noises $S_\phi^{1,2}$.

5.5 Preliminary results of phase noise reduction

To characterize the out-of-loop comb rep-rate phase noise, we employed a self-heterodyne method based on an AOM-modified unbalanced MZI interferometer. First, a waveshaper is used to select two comb lines ($k-$th line and $l-$th line). These two comb lines are then sent to an acoustic-optic modulator (AOM), and both of them get split into a 55MHz-frequency-shifted (1st order output) path and an unshifted (0-th order output) path. A fiber polarization controller and a 200-m fiber delay are also inserted into the frequency-shifted path, and two paths are then combined using a 50/50 coupler. This forms the AOM-modified unbalanced MZI interferometer with an FSR of 1.031 MHz. The MZI output is then sent to an FBG to separate the two comb lines with different frequencies of $f_k = f_p + kf_{rep}$ and $f_l = f_p + lf_{rep}$. Each of the comb lines is sent to a photodiode for self-heterodyne detection, and a signal with a 55 MHz carrier frequency (resulting from the AOM frequency shift) can be measured on an oscilloscope. More details of this method can be found in (Yuan et al. 2022).

The instantaneous phase fluctuation of each comb line ($\phi_k(t) = \phi_p(t) + k\phi_{rep}(t)$,$\phi_l(t) = \phi_p(t) + l\phi_{rep}(t)$) can be acquired during the data post-processing by applying the Hilbert Transform to the signal measured on the oscilloscope. The 200-m fiber delay in MZI provides both high sensitivity to the phase fluctuations and broad noise measurement bandwidth (~1 MHz). The phase of comb rep-rate can be calculated by subtracting the phase of two comb lines, $\phi_{rep}(t) = (\phi_l(t) - \phi_k(t))/(l-k))$, where the phase of the common pump laser is canceled. The phase noise of the comb rep-rate can be obtained by calculating the power spectral density of $\phi_{rep}(t)$ using Fourier transform. As shown in Fig. 5.2, the phase noise of the comb rep-rate is plotted when the comb is free-running and OFD locked. A locking bandwidth of 300 kHz is observed, and the phase noise of locked comb rep-rate reaches -115 dBc/Hz.

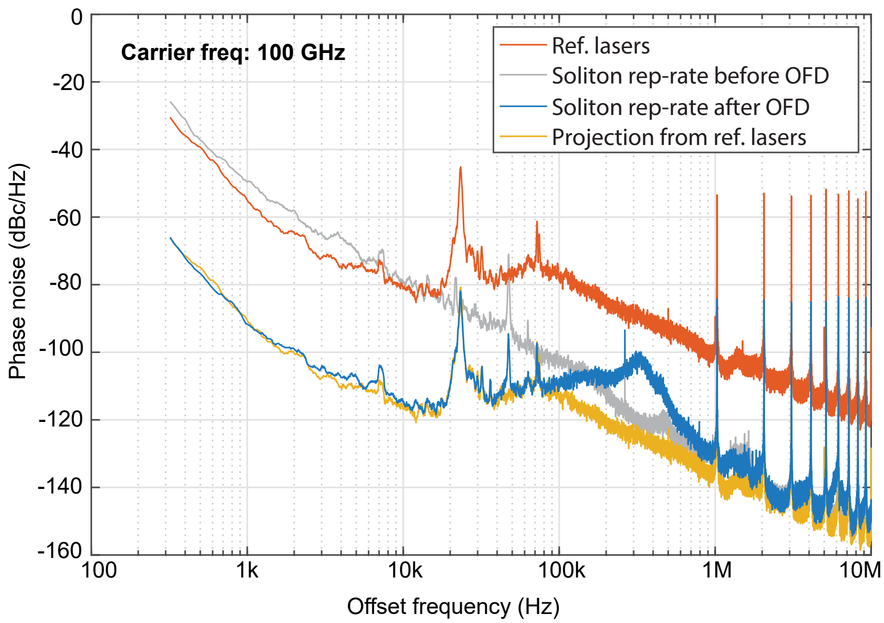

Figure 5.2: **Preliminary results of integrated OFD.** Phase noise measurement of reference lasers (red), rep-rate of free running soliton (grey), and OFD soliton (blue).

5.6 Disucssion

In this chapter, the initial demonstration of the integrated OFD is presented. The phase noise of the comb rep-rate reaches -115 dBc/Hz using two reference lasers with their relative phase noise of -81 dBc/Hz at 10 kHz offset frequency. Ultimately, the rep-rate phase is limited by 1) the reference cavity thermo-refractive noise (TRN) and 2) the division ratio. A longer reference cavity can be used to further reduce cavity TRN, and an octave-spanning comb (M. H. Pfeiffer, Herkommer, et al. 2017) can be used to provide more comb lines (or division ratio) for optical frequency division.

In the experiment, another limiting factor to the locking performance is the in-loop noise. We want the in-loop noise (when locking) to be lower than the divided reference laser noise, otherwise, the comb rep-rate phase noise will be limited by the in-loop noise. The in-loop noise can be optimized by increasing the SNR of the OFD signals ($\Delta = \Delta_1 - \Delta_2$).

More importantly, a 100 GHz low-noise mmWave can be synthesized by sending the OFD-implemented microcomb to an ultrahigh-speed photodiode. Its phase noise can be characterized by down-converting the signal using a local oscillator (LO) through a harmonics mixer (B. Wang, J. S. Morgan, et al. 2021). However, if the LO phase noise is higher than the microcomb noise, the measurement floor will be set by local oscillator. To accurately characterize the microcomb noise, one can lock the n-th harmonics of LO to the microcomb through a phase-locked-loop (Jiang Li, Yi, et al. 2014; Tetsumoto, Ayano, et al. 2020). Then the microcomb noise can be acquired by directly measuring the LO noise multipled by N^2.

Chapter 6

Dual-comb Vernier frequency division to detect and stabilize sub-THz comb rep-rate

6.1 Introduction

The recent development of microresonator-based soliton frequency combs (soliton microcombs) (Del'Haye et al. 2007; Tobias J Kippenberg, Ronald Holzwarth, and S. Diddams 2011; Tobias J Kippenberg, Gaeta, et al. 2018; Gaeta, Lipson, and Tobias J Kippenberg 2019) has miniaturized optical frequency comb technology and has the potential to revolutionize metrology, time keeping and spectroscopy (Udem, Ronald Holzwarth, and Hänsch 2002; S. Diddams, Bergquist, et al. 2004; Nathan R Newbury 2011). These solitary wave packets leverage Kerr nonlinearity to compensate cavity loss and to balance chromatic dispersion (Akhmediev and Ankiewicz 2008; Leo et al. 2010; Herr, Brasch, et al. 2014). They output a repetitive pulse stream at a rate set by the resonator roundtrip time, which can range from GHz to THz (Suh and Kerry Vahala 2018; Q. Li et al. 2017; M. H. Pfeiffer, Herkommer, et al. 2017). The reduction of resonator mode volume increases the intracavity Kerr nonlinearity, lowers the operation pump power and extends the comb spectrum span. This has enabled demonstrations of battery-operated soliton combs at 194 GHz repetition rate(Stern et al. 2018), and octave-spanning soliton generation for self-referencing in a resonator with 1 THz free-spectral-range (FSR)(Spencer et al. 2018). High repetition rates (rep-rates) are also desired in many comb-based applications. For instance, the maximum acquisition speed in dual-comb spectroscopy(Suh, Q.-F. Yang, et al. 2016; Pavlov et al. 2017; Dutt et al. 2018), ranging (Trocha et al. 2018; Suh and Kerry J Vahala 2018), and imaging (Bao, Suh, and Kerry Vahala 2019; Yi, Q.-F. Yang, K. Y. Yang, and Kerry Vahala 2018), all increase linearly with the comb repetition rate.

However, to detect the high repetition rate, a microresonator-based frequency comb (microcomb) system has to include an auxiliary frequency comb whose repetition rate can be directly detected by a photodiode (PD). The detectable repetition frequency is then multiplied up optically through the equally-spaced comb lines to track the microcombs in action (Del'Haye et al. 2007; Spencer et al. 2018). This limits the miniaturization of microcomb system as the area occupied by the resonator scales inverse quadratically with the repetition rate. For the popular electrical K-band, the auxiliary resonator diameter has to exceed several millimeters (H. Lee et al. 2012; Yi, Q.-F. Yang, K. Y. Yang, Suh, et al. 2015; K. Y. Yang et al. 2018; Lucas et al. 2020). An approach to divide and detect microcomb repetition frequency beyond photodiode's bandwidth will be critical to eliminate this restriction, and will advance the frequency comb technology in terms of miniaturization, power consumption and ease of integration.

In this chapter, a Vernier frequency division method is developed to detect soliton microcomb repetition rate well above the electrical bandwidth in use. In contrast to the conventional approaches, the Vernier frequency division does not require low-rate frequency combs. Instead, the rate of the auxiliary combs, f_{r2}, can be higher than that of the main combs, f_{r1}, and it can be free-running and stay unknown.

6.2 Methods of rep-rate detection

The repetition-rates of soliton microcombs can be from GHz to THz. Depending on its frequency, three methods are introduced in this section for rep-rate detection.

6.2.1 Direct photodetection

The simplest method is the direct photodetection of microcombs whose rep-rate frequency is detectable within the bandwidth of photodiodes and electronics (Herr, Brasch, et al. 2014; Yi, Q.-F. Yang, K. Y. Yang, Suh, et al. 2015; Suh and Kerry Vahala 2018; J. Liu, Lucas, et al. 2020). However, to detect rep-rates higher than 100 GHz, it will be more challenging since it goes beyond the commercial electronics bandwidth. In this case, ultrahigh-speed photodiodes and a method of frequency down-conversion are needed (S. Zhang, Silver, Shang, et al. 2019; Zang et al. 2020; Tetsumoto, Ayano, et al. 2020; B. Wang, J. S. Morgan, et al. 2021).

6.2.2 Low-rate comb calibration method

A conventional method uses low-rate combs to detect high rep-rate combs without the need of a ultrahigh-speed photodiode and electronics (Brasch et al. 2016). The concept is shown in Fig. 6.1 (c). By beating the low-rate combs and high-rate combs, the rep-rate of high-rate combs can be calibrated with the beatnote frequencies and the rep-rate of low-rate combs times an integer M.

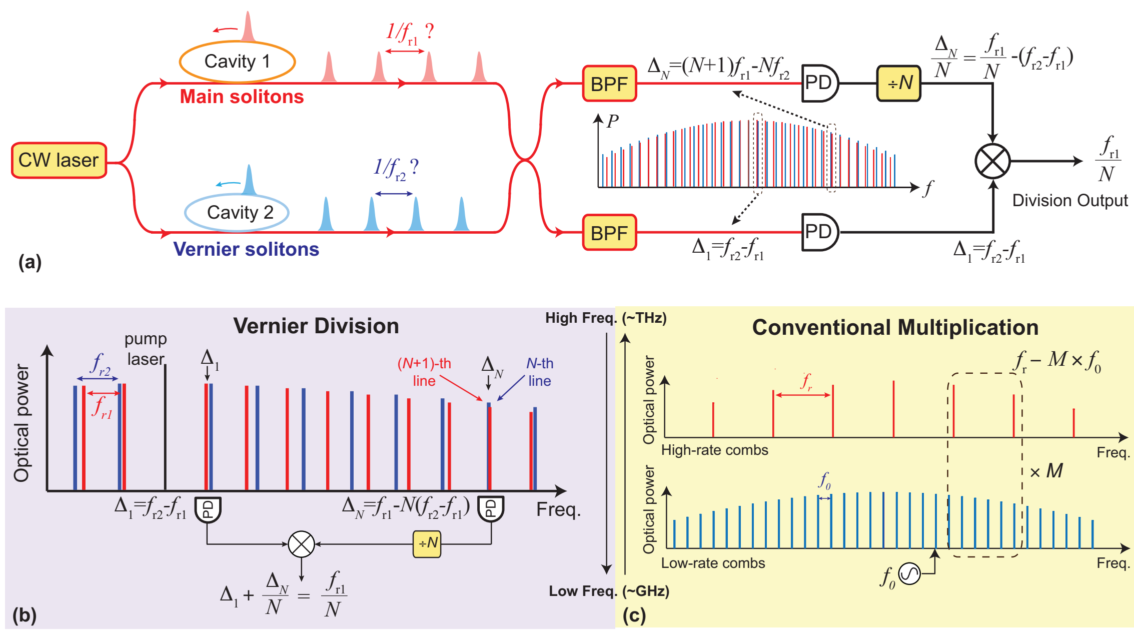

Figure 6.1: **Concept of Vernier dual-comb repetition rate division.** **(a)** To divide and detect the main soliton (red) repetition rate, a free-running higher rate microcomb (Vernier, blue) is generated to sample and divide down the main soliton rep-rate. Two pairs of low frequency dual-comb beat notes are selected by optical bandpass filters (BPFs) and detected on photodiodes (PDs) to extract the high repetition frequency. **(b)** The zoomed-in optical spectra to illustrate the Vernier division principle. When the Vernier soliton rep-rate is slightly higher than the main soliton rep-rate, the frequency of the N-th Vernier comb line can coarsely align with the $(N+1)$-th main soliton comb line. The corresponding beat frequency contains information of the absolute repetition rate (f_{r1}) and the repetition rate difference $(f_{r2} - f_{r1})$. The main soliton repetition rate can be divided down by N by electrically dividing Δ_N by N, and then adding it with Δ_1. **(c)** In comparison, conventional repetition rate detection methods require a low rep-rate comb to optically multiply a low frequency reference to a high frequency, which is then compared to the high repetition rate through heterodyne detection.

An alternative approach is based on the electro-optics modulation (EOM comb) (Jiang Li, Yi, et al. 2014). The EOM configuration is shown in the purple panel in Fig. 6.2. An optical bandpass filter is used to select two adjacent comb lines from the main soliton, which are then amplified by an EDFA. They are then sent into an electro-optic phase modulator which is driven by VCO_2 at a frequency of f_{VCO2}. Modulation sidebands are created for both comb lines, and when the modulation is strong enough, a pair of sidebands will meet in the midpoint of the two comb lines (Jiang Li, Yi, et al. 2014). This pair of sidebands is then optically filtered by a Bragg-grating filter, and is detected on a photodiode.

6.2.3 Vernier frequency division method

Small diameter resonators and high repetition rates are critical when pursuing low power consumption, massive integration, and octave-spanning for self-referencing. However, the low-rate comb calibration method would require a much larger auxiliary resonator compared to the soliton microresonator we want to detect. For example, the popular electrical K-band comb need an auxiliary resonator with a diameter exceeding several millimeters (H. Lee et al. 2012; Yi, Q.-F. Yang, K. Y. Yang, Suh, et al. 2015; K. Y. Yang et al. 2018; Lucas et al. 2020). Therefore, an approach that can eliminate the need for large diameter calibrate comb is important in terms of miniaturization, power consumption and ease of integration. The vernier frequency division is developed to address the issue.

The concept is illustrated in Fig. 6.1. The main and Vernier soliton comb lines create two free-running graduation markings on the optical frequency domain, and similar to a Vernier caliper, these markings coarsely align periodically. Detectable frequency beat notes can be created when the frequency of the N-th higher-rate comb line catches up with that of the $(N+1)$-th lower-rate comb line. These beat notes can be utilized to divide the soliton repetition frequency through an electrical frequency division followed by the subtraction of dual-comb repetition rate difference. Figure 6.1 presents one conceptual example, where the main soliton repetition rate divided by N can be obtained from the sum of the first beat frequency Δ_1, and the N-th beat frequency Δ_N divided by N. Δ_N denotes the beat frequency between the N-th Vernier comb line and its nearest main soliton comb line.

Vernier frequency division method can use two pairs of comb lines in the overtaking regime, where the frequency of the N-th higher-rate comb line catches up with that of the $(N+1)$-th lower-rate comb line. Here, we use the N-th pair and the M-th pair of comb lines as an example, and $\Delta f_{N,M}$ denotes the frequency difference between the $N(M)$-th Vernier soliton comb line and its nearest main soliton comb line:

$$\Delta f_N = N f_{\mathrm{r2}} - (N+1) f_{\mathrm{r1}} = N(f_{\mathrm{r2}} - f_{\mathrm{r1}}) - f_{\mathrm{r1}}, \tag{6.1}$$

$$\Delta f_M = M f_{\mathrm{r2}} - (M+1) f_{\mathrm{r1}} = M(f_{\mathrm{r2}} - f_{\mathrm{r1}}) - f_{\mathrm{r1}}. \tag{6.2}$$

f_{r1} and f_{r2} are the rep-rates of the main solitons and Vernier solitons, respectively. Eq. (6.1)$/N$ subtracted by Eq. (6.2)$/M$ will yield

$$(\frac{1}{M} - \frac{1}{N}) f_{\mathrm{r1}} = \frac{\Delta f_N}{N} - \frac{\Delta f_M}{M}, \tag{6.3}$$

where the repetition rate of the main solitons, f_{r1}, is now expressed by two measurable quantities. In the experiment, photodetecting the corresponding pair of comb lines produces RF signals at the frequency of $\Delta_{M,N}$, where $\Delta_{M,N} = |\Delta f_{M,N}|$. The "$\pm$" ambiguity in $\Delta f_{M,N} = \pm\Delta_{M,N}$ can be resolved by measuring the optical spectral of the main and Vernier solitons.

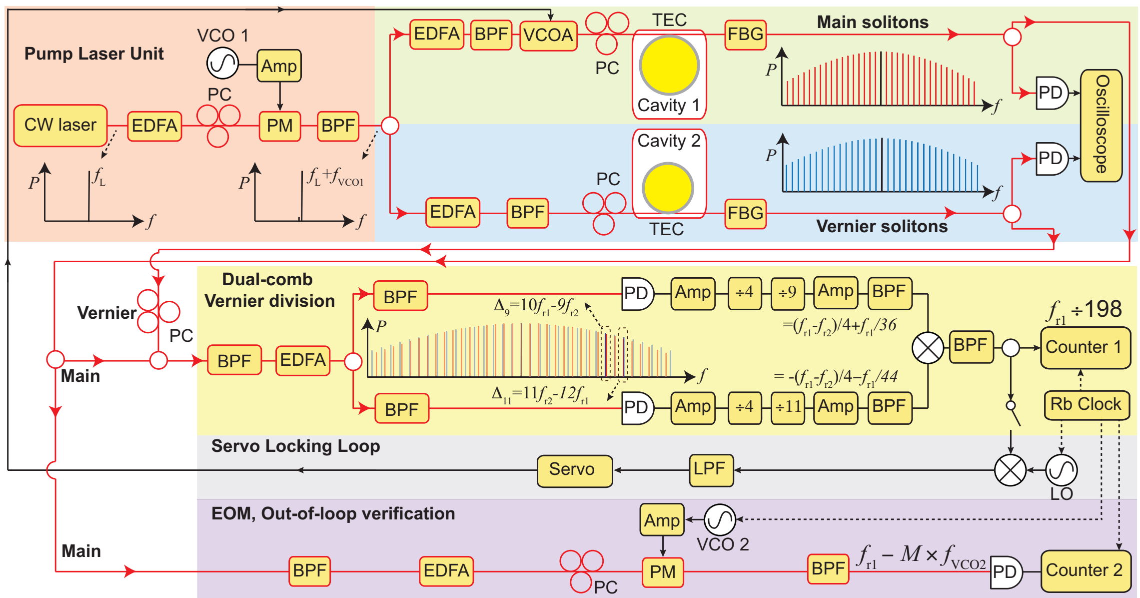

Figure 6.2: **Experimental setup.** The main solitons and Vernier solitons are generated in two SiN resonators which are temperature controlled by thermoelectric coolers (TECs). The pump laser is the first modulation sideband of a phase modulated (PM) continuous wave (cw) laser, and the sideband frequency can be rapidly tuned by a voltage controlled oscillator (VCO) (J. R. Stone et al. 2018). The frequencies of the cw laser and phase modulation are f_{L} and f_{VCO1}, respectively. The main and Vernier solitons are combined and then split to two paths, and two optical bandpass filters (BPFs) are used to select the 9-th and the 11-th pairs of comb lines in each path, respectively. Beat notes Δ_9 and Δ_{11} are generated by photodiodes (PDs) and they are electronically divided by 36 and 44, respectively. The sum of the two signals is created by a frequency mixer, and its frequency f_{v} is recorded on a counter. For stabilizing the rep-rate of main solitons, f_{v} is mixed with a rubidium-referenced local oscillator (LO) to servo control a voltage controlled optical attenuator (VCOA) for repetition rate tuning. For out-of-loop verification, electro-optics modulation (EOM) method is used and shown in the purple panel. Erbium-doped fiber amplifiers (EDFAs), polarization controllers (PCs), electrical amplifiers (Amps), low pass filters (LPFs) and rubidium (Rb) clock are also used in the experiment.

6.3 Dual-microresonator soliton generation

The dual-microresonator soliton generation is the first step of Vernier frequency division. The complete experimental setup is shown in Fig. 6.2. In our experiment, the main and Vernier solitons are generated in bus-waveguide coupled Si_3N_4 microresonators M. H. Pfeiffer, Kordts, et al. 2016, which have FSRs of 197 GHz and 216 GHz, intrinsic quality factors of 1.5×10^6 and 2.2×10^6, and loaded quality factors of 1.3×10^6 and 1.8×10^6, respectively. To overcome the thermal complexity in soliton generation process, the first phase-modulated sideband from a continous wave (CW) laser is used as a rapid-tuning pump laser. The phase modulator is driven by a voltage-controlled oscillator (VCO). The first sideband from the phase modulation is selected by an optical tunable bandpass filter (BPF). With the fast ramp voltage on the VCO, the pump laser scans at a speed of ~ 20 GHz/μs. A 50/50 splitter after the BPF splits the pump laser equally into two erbium-doped fiber amplifiers (EDFAs). The polarization is carefully adjusted by a polarization controller after each EDFA. The pump laser is coupled into the bus waveguide by a lensed fiber. Single solitons are generated simultaneously in both microresonators by rapidly scanning the pump laser from the blue-detuned regime to the red-detuned regime. The single soliton existence detuning ranges of both microresonators are thermally tuned to overlap. Each microresonator has a temperature controller with 0.01°C resolution. The resonant frequencies are tuned ~ 2.5 GHz/°C. The optical spectra of single soliton states for main (red) and Vernier (blue) resonators are shown in Fig. 6.3**a**. A zoomed-in panel shows the optical spectra where the frequency of the N-th Vernier soliton comb line coarsely aligns with that of the $(N+1)$-th main soliton comb line. An electrical spectrum of the beat frequencies between the two combs is shown in Fig. 6.3**b**. Within the 26 GHz cut-off frequency of our electrical spectrum analyzer (ESA), four beat frequencies are observed: $\Delta_1 = 19.3639$ GHz, $\Delta_9 = 22.6815$ GHz, $\Delta_{10} = 3.3157$ GHz and $\Delta_{11} = 16.0449$ GHz. The strong VCO_1 beat note near 14 GHz is derived from the modulation of the cw laser, and can be removed by an optical or electrical filter.

6.4 Detecting sub-THz comb rep-rate

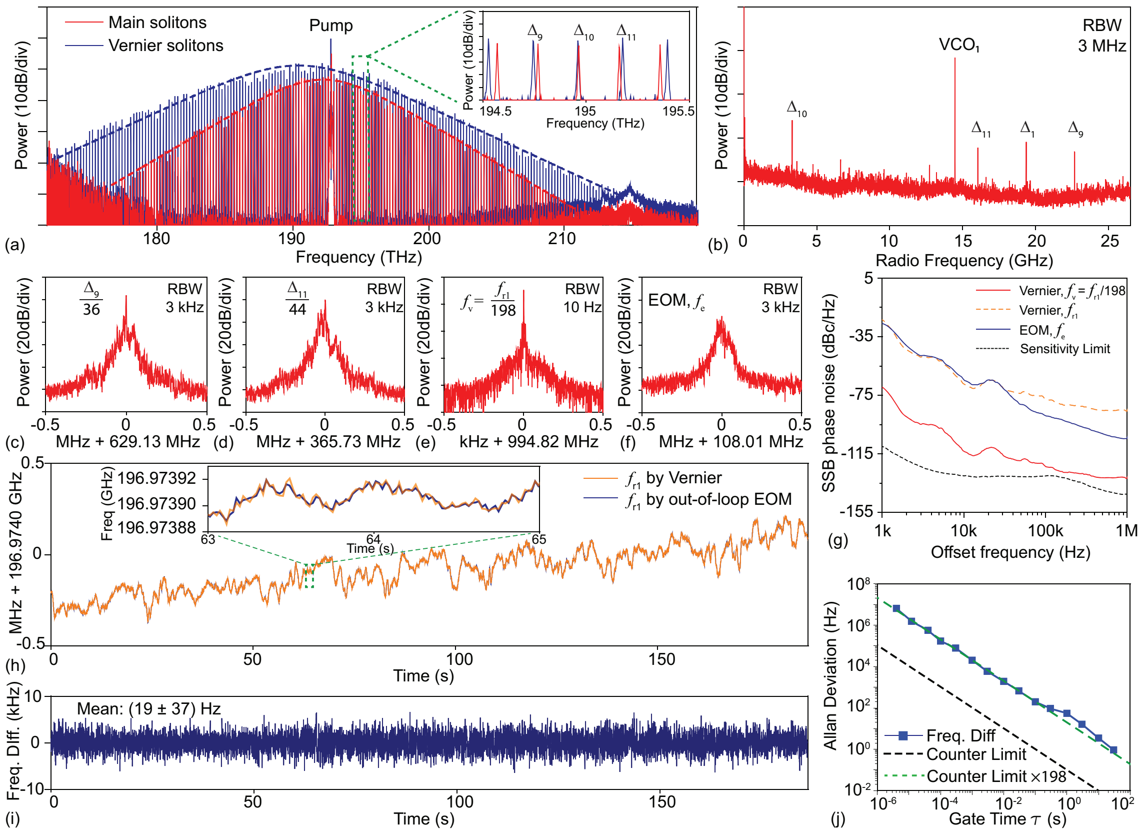

Figure 6.3: **Summary of experimental data.** **(a)** Optical spectra of main solitons (red) and Vernier solitons (blue) with sech^2 envelopes (dashed lines). The 9-th and 11-th pairs of comb lines are shown in the zoomed-in panel. The pump laser is suppressed by Bragg-grating filters. **(b)** ESA spectra of dual-comb beat notes. Δ_1, Δ_9, Δ_{10}, and Δ_{11} are apparent. The strong VCO_1 beat note is derived from the pump laser unit, and can be filtered out optically or electronically. ESA spectrum of: **(c)** Δ_9 divided by 36, **(d)** Δ_{11} divided by 44, **(e)** $f_v = f_{r1}/198$ as the sum of $\Delta_9/36$ and $\Delta_{11}/44$, and **(f)** beat note f_e from out-of-loop EOM method. **(g)** Phase noise measurement of f_v (red) and f_e (blue). The phase noise of f_v multiplied by 198^2 matches that of f_{r1} measured by out-of-loop EOM method. **(h)** Rep-rate of the main solitons measured by Vernier method (orange) and EOM method (blue). Both main and Vernier solitons are free-running. The gate time is 10 ms. **(i)** The frequency difference between rep-rate measured with Vernier and EOM methods in panel (h). Mean value is concluded with a 95% confidence interval under normal distribution. **(j)** Allan Deviation of the frequency difference. The frequency difference agrees with the counter resolution limit for the Vernier method.

Beat frequencies Δ_9 and Δ_{11} are selected for the main soliton rep-rate division. $\Delta_9(\Delta_{11})$ is the beat frequency between the 9 (11)-th Vernier soliton comb line and the 10 (12)-th main soliton comb line, where $\Delta_9 = 10f_{\mathrm{r1}} - 9f_{\mathrm{r2}}$, and $\Delta_{11} = 11f_{\mathrm{r2}} - 12f_{\mathrm{r1}}$. In the measurement, after combining the main and Vernier solitons with a fiber coupler, a bandpass filter is used to pass the comb lines associated with Δ_9, Δ_{10}, and Δ_{11} for optical amplification. Then a second fiber coupler splits the power into two optical paths, where in each path a bandpass filter is used to select the comb lines of Δ_9 or Δ_{11}, and the corresponding beat note is created on a photodiode. To divide the main soliton rep-rate, Δ_9 and Δ_{11} are divided by 36 and 44 in frequency, respectively, and sent to a RF mixer to produce their sum frequency, $f_{\mathrm{v}} = \Delta_9/36 + \Delta_{11}/44 = f_{\mathrm{r1}}/198$, which is the main soliton repetition rate divided by 198. The electrical spectra of $\Delta_9/36$, $\Delta_{11}/44$ and their sum f_{v} are shown in Fig. 6.3**c,d,e**. The complete experimental setup is shown in Fig. 6.2. In principle, one can use the configuration in Fig. 6.1, where Δ_1 is mixed with Δ_N/N to generate f_{r1}/N. However, limited by the selection of electrical mixers in our lab, we do not have the capability to mix Δ_1 ($\sim$ 20 GHz) and Δ_N/N ($\sim$ 2 GHz for $N = 9, 11$), and thus we select Δ_9 and Δ_{11} instead.

To validate the Vernier method, a conventional method by using electro-optics modulation (EOM) frequency comb is implemented as an out-of-loop verification. In the conventional EOM method, two adjacent comb lines from the main solitons are phase modulated at the frequency of a VCO to produce modulation sidebands. The strong modulation results in a pair of sidebands near the midpoint of the two comb lines, and they can be optically filtered and detected (Brasch et al. 2016; Jiang Li, Yi, et al. 2014) (see Fig. 6.2). The detected EOM beat note (Fig. 6.3**f**) has frequency of $f_{\mathrm{e}} = f_{\mathrm{r1}} - M \times f_{\mathrm{VCO2}}$, where M is the number of modulation sidebands, and f_{VCO2}

is the modulation frequency. M and f_{VCO2} are set to 11 and 17.897 GHz in this experiment, respectively. It is worth noting that the Vernier beat note f_{v} has much narrower linewidth than the EOM beat note f_{e}, which implies that the rep-rate of the main solitons is coherently divided down from 196.974 GHz to 994.82 MHz.

To show the coherent division in the Vernier dual-comb method, the phase noise of the Vernier beat note, f_{v}, and the out-of-loop EOM beat note, f_{e}, are measured with an ESA through direct detection technique (Fig. 6.3**g**). For coherent frequency division, the phase noise of f_{v} (red trace) should be 198^2 lower than the phase noise of the undivided rep-rate, which is measured through the EOM method (blue trace). This is verified in our measurement, as the phase noise of f_{v} multiplied by 198^2 (orange dash trace) agrees very well with the phase noise of f_{e} at offset frequency up to 30 kHz. Beyond 30 kHz offset frequency, the phase noise of f_{v} is comparable to the ESA sensitivity limit (black dash trace). At high offset frequency, our phase noise measurement might be affected by relative intensity noise (RIN). This is common for direct detection technique, as the RIN cannot be separated from the phase noise in the measurement.

The rep-rate of the main solitons can be derived by multiplying the Vernier beat note, f_{v}, by 198. A zero-dead-time frequency counter is used to record f_{v}. The main soliton rep-rate, $f_{\mathrm{r1}} = 198 \times f_{\mathrm{v}}$, is shown in Fig. 6.3**h** (orange trace). The free-running main solitons have repetition rate around 196.9740 GHz, and the rate is drifting due to temperature and pump laser frequency fluctuations. This rep-rate measurement is compared to the rep-rate measured with out-of-loop EOM method. The frequency of the EOM beat note f_{e} is recorded on a second zero-dead-time counter, and the rep-rate is derived as $f_{\mathrm{r1}} = f_{\mathrm{e}} + M \times f_{\mathrm{VCO2}}$. The EOM-measured rep-rate is shown in Fig. 6.3**h** (blue trace), and it overlaps with the rep-rate measured by Vernier method perfectly. The frequency difference between the Vernier-measured rep-rate and EOM-measured rep-rate is calculated and shown in Fig. 6.3**i**, and it has a mean value of (19 $\pm$ 37) Hz with a 95% confidence interval under normal distribution. Figure 6.3**j** shows the Allan deviation of this frequency difference at various gate times, and it agrees with the counter resolution limit at the frequency of f_v (dash black trace) multiplied by 198 (green dash trace), which is the counter limit for $f_{\mathrm{r1}} = 198 \times f_\mathrm{v}$. This indicates that no frequency difference between the Vernier method and the EOM method can be detected within the sensitivity of our instruments. In all frequency measurements, the counters and VCOs are synchronized to a rubidium clock.

6.5 Locking sub-THz comb rep-rate

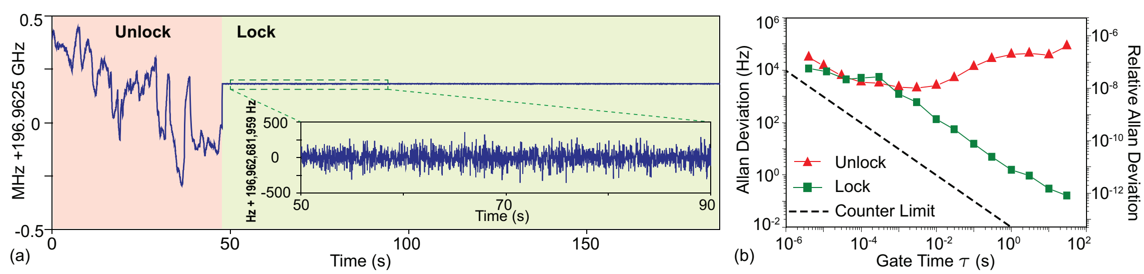

Figure 6.4: **Stabilization of main soliton repetition rate by using Vernier dual-comb method.** The rep-rate of the main solitons is stabilized by locking f_v to a Rb-referenced oscillator, and the locking is verified by using EOM method. **(a)** Rep-rate measurement using EOM method. The locking loop is engaged at the time near 50 s. The gate time (τ) is 10 ms. **(b)** Allan deviation calculated from the unlocked and locked repetition rates that are measured with the EOM method. The locking loop has $\sim$ kHz servo bandwidth. Within the servo bandwidth, the Allan deviation goes down as $1/\tau$. Beyond the servo bandwidth, the Allan deviation is similar to that of the free-running unlock rep-rate. The error in the rubidium clock has been corrected for the Allan deviation of the locked rep-rate. This is done by synchronizing the EOM and the soliton rep-rate to the same rubidium reference. In the entire measurement, the repetition rate of the Vernier solitons is not stabilized, and there is no feedback control of the laser-cavity detuning for the Vernier solitons.

The main soliton repetition rate can be stabilized by locking the Vernier beat note f_v to a radio-frequency reference. In this demonstration, f_v is locked to a rubidium-stabilized local oscillator through servo control of the pump power using an voltage-controlled optical attenuator (VCOA) to vary the main soliton repetition rate (see Fig. 6.2). Rep-rate measurement with the EOM method is utilized to verify the locking and the result is shown in Fig. 6.4**a**. To eliminate the relative frequency drifts of the electronic components, f_{VCO1}, f_{VCO2}, counter 1 and counter 2 are all synchronized to the same rubidium clock. Therefore, the error in the rubidium clock has been corrected, and the absolute stability of the reference will not affect our frequency readouts. This allows us to evaluate the servo locking loop without using high performance atomic clock reference. The locking is turned on at the time near 50 s, and the soliton rep-rate immediately stops drifting and is stabilized to 196,962,681,959 Hz (see Fig. 6.4**a**). The Allan deviations of the free-running (red) and stabilized (green) rep-rate are calculated from the EOM-based rep-rate measurements and are presented in Fig. 6.4**b**. Above 0.3 ms gate time, the Allan deviation of the locked rep-rate scales as $1/\tau$, where τ is the gate time. Below 0.3 ms gate time, the Allan deviation of the rep-rate follows that of the free-running rep-rate. This behavior of the Allan deviation is expected for a phase-locked oscillator with $\sim$ kHz locking bandwidth. Ultimately, the absolute stability of the rep-rate is limited by the atomic clock reference. It is worth noting that the repetition rate of the Vernier solitons is not stabilized in the entire measurement.

6.6 Summary

In this chapter, we demonstrated the Vernier frequency division method to detect and stabilize soliton repetition rate at 197 GHz with 20s GHz bandwidth photodiodes and electronics. The Vernier method shall be applicable for a wide range of repetition frequencies. It also applies to the case where the two frequency combs do not share the same pump frequency/center frequency. In this situation, one more pair of beat frequency should be detected. As this additional beat note and the two Vernier beat notes share the same offset frequency between the two pump lasers, the offset frequency can be eliminated by frequency subtraction. This will enable the Vernier method to be applied to other types of high-rate combs, such as mode-locked semiconductor lasers (Rafailov, Cataluna, and Sibbett 2007). The concept of Vernier dual combs could also be modified to assist carrier-envelope offset frequency (f_{CEO}) detection for self-referencing an octave-spanning microcomb. At 1 THz rep-rate, the f_{CEO} given by the f-$2f$ signal can range from 0 to 500 GHz, and it is challenging to keep this frequency in a detectable range as it is subject to small fabrication variations. However, if a Vernier comb is frequency doubled and beat against the main comb, a series of f-$2f$ beat frequencies can be created. Their spacing equals to the dual-comb rep-rate difference, and this can bring the f-$2f$ signal to a detectable frequency. Finally, the Vernier method has the potential to revolutionize optical and electrical frequency conversion by eliminating the need for a detectable repetition rate frequency comb, and it will have direct applications in optical clock (Newman et al. 2019), optical frequency division (Fortier, Kirchner, et al. 2011), and microwave frequency synthesis (Lucas et al. 2020).

Chapter 7

Line-by-line Fourier synthesis of radio-frequency arbitrary waveforms using optical dual-comb

7.1 Introduction

Fourier synthesis leverages precise line-by-line amplitudes and phases control of individual spectral components for waveform construction. It has been widely implemented in optical frequency and audio frequency domains for applications in arbitrary waveform generation, ultrafast optics, and coherent quantum interaction with atoms and molecules (Z. Jiang, Huang, et al. 2007; Cundiff and Weiner 2010) (AWG), coherent control of quantum processes (Goswami 2003; Stowe et al. 2006; Barmes, Witte, and Eikema 2013), and optical communications (Geisler et al. 2009). The broad optical bandwidth provides femtosecond temporal resolution in the Fourier synthesis (Chan et al. 2011) that is not attainable by conventional electronics.

Fourier synthesis in optical domain can be down-converted to microwave and mmWave frequencies (Durán, Tainta, et al. 2015; Durán, Andrekson, et al. 2016; Ferdous, Leaird, et al. 2009; Zhou et al. 2013; Yin et al. 2021; Ataie et al. 2015) through coherent dual-comb sampling method (Coddington, W. Swann, and N. Newbury 2009), and it could have wide applications in wireless communications, radar systems, and electronic testing (J.-W. Lin et al. 2012; Ghelfi et al. 2014; I. S. Lin, McKinney, and Weiner 2005). When photomixing two optical frequency combs with different repetition rates on a photodiode, an RF frequency comb will be created, with its comb lines deriving their amplitudes and phases from the dual optical combs. Line-by-line amplitude and phase control on optical frequency combs (Ferdous, Miao, et al. 2011) can then be coherently mapped to the RF frequency comb for waveform synthesis, which has been shown recently with electro-optic frequency combs (Durán, Tainta, et al. 2015; Durán, Andrekson, et al. 2016; Ferdous, Leaird, et al. 2009; Zhou et al. 2013; Yin et al. 2021; Ataie et al. 2015). Compared with other existing photonic methods for RF waveform generation (Khan et al. 2010; Rashidinejad and Weiner 2014; Rashidinejad, Leaird, and Weiner 2015; Rashidinejad, Y. Li, and Weiner 2015; Jian Wang et al. 2015; Tan et al. 2020), which rely on optical delay structures to either provide enough dispersion for far-field frequency-to-time mapping, or route different replicas of a low repetition rate optical pulse to different arrival times on a photodiode, the Fourier synthesis method eliminates the need for long tunable optical delay lines and low repetition rate mode-locked lasers, and thus creates the potential for mass-scale integration on a photonic chip.

In this chapter, we demonstrated RF spectral line-by-line waveshaping and Fourier synthesis of RF waveforms by using optical dual-microresonator solitons (Herr, Brasch, et al. 2014; Brasch et al. 2016; Suh, Q.-F. Yang, et al. 2016; Tobias J Kippenberg, Gaeta, et al. 2018). The high repetition rate of soliton microresonator-based frequency combs (microcombs) (Tobias J Kippenberg, Gaeta, et al. 2018) enables line-by-line amplitude and phase control of individual optical comb lines (Ferdous, Miao, et al.

2011). Dual-comb coherent sampling is then used to coherently down-convert the waveshaped optical microcomb to RF frequencies by beating it with another soliton microcomb on a fast photodiode. A complete discrete Fourier series can be constructed for waveform synthesis by nullifying the carrier envelope offset frequency in the down-converted RF frequency comb. A series of temporal waveforms, including: tunable Gaussian, triangle, square, and "UVA"-like logo, are demonstrated to illustrate arbitrary waveform synthesis. All critical components in the dual-microcomb method, including soliton microcombs (Tobias J Kippenberg, Gaeta, et al. 2018), wavelength multiplexer/demultiplexer (Rahim et al. 2019), intensity and phase modulators (C. Wang et al. 2018), optical amplifier (Beeck et al. 2020), and ultrafast photodiodes (Q. Yu et al. 2020), are compatible with photonic integration. A discussion of waveform quality and a comparison of the effective number of bits (ENOB) with electronic AWG are presented at the end of the section.

7.2 Concept of line-by-line Fourier synthesis

The concept of dual-microcomb RF line-by-line waveshaping is illustrated in Fig. 7.1. Signal solitons with a repetition rate of f_r, and local solitons with a repetition rate of $f_r + \Delta f_r$, are generated in two Kerr microresonators pumped by the same laser (Dutt et al. 2018; B. Wang, Z. Yang, Xiaobao Zhang, et al. 2020). A radio-frequency (RF) comb with zero offset frequency and a comb spacing of Δf_r can be created by beating the signal and local solitons on a fast photodiode. The RF comb forms a Fourier series, with $V(t) = \sum_{n=0}^{\infty} A_n \cos(2\pi n \Delta f_r t + \varphi_n)$, where $V(t)$ is the voltage output of the photodiode, n is the comb line number, A_n and φ_n are the amplitude and phase of n-th comb line, respectively. As the amplitude and phase of

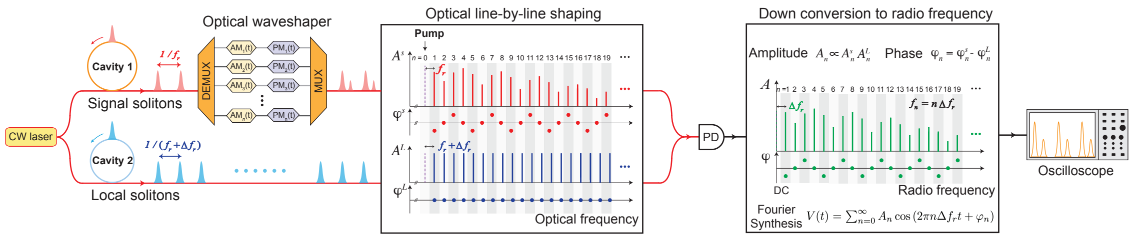

Figure 7.1: **Concept of RF line-by-line Fourier synthesis with dual-microresonator solitons.** A radio-frequency (RF) comb that is composed of a series of equidistant RF lines is created by photomixing two soliton microcombs with slightly different repetition frequencies on a photodiode (PD). The RF comb spacing is set by the repetition rate difference of the two soliton microcombs, and the RF comb offset frequency is nullified by using a common pump laser to drive both optical solitons. To implement line-by-line amplitude (A_n) and phase (φ_n) control of the RF comb lines, one of the optical microcomb (signal solitons) goes through optical line-by-line waveshaping, and optical amplitude modulations (AMs) and phase modulations (PMs) are down-converted to the RF frequency comb through dual-microcomb coherent sampling. As the RF frequency comb forms a complete Fourier series, arbitrary temporal waveforms can be synthesized.

the RF comb lines are fully derived from the amplitude and phase of the corresponding optical comb lines, the line-by-line optical waveshaping on the signal solitons can fully control the amplitude and phase of the RF comb. In principle, dynamic waveform synthesis is possible by using time varying modulations of A_n and φ_n through the use of electro-optic modulators. Here, an off-the-shelf optical waveshaper is used instead to demonstrate static, repetitive waveform synthesis.

7.3 Arbitrary waveform generation using Fourier synthesis

In our experiment, the signal and local solitons are generated in SiN micro-ring resonators (M. H. Pfeiffer, Kordts, et al. 2016) with intrinsic quality factors of 7.7×10^6 and 4.3×10^6, respectively. The radii of the signal and local soliton resonators are set to 228.65 μm and 228.30 μm, respectively, which introduces a 150 MHz repetition rate offset (Δf_r) between the two solitons. To create an RF comb with zero offset frequency, both optical solitons are generated using the same pump laser (Dutt et al. 2018; B. Wang, Z. Yang, Xiaobao Zhang, et al. 2020). Thermoelectric coolers (TECs) are placed beneath microresonators to coarsely align the resonance frequencies of the two resonators at the pump laser wavelength. The thermal tuning of the resonant frequency is ~2.5 GHz/°C, and the TEC has a resolution of 0.01°C. A rapid laser frequency scanning method that leverages the single-sideband suppressed-carrier (SSB-SC) modulator (J. R. Stone et al. 2018) is used to generate single soliton states in both resonators simultaneously (B. Wang, Z. Yang, Xiaobao Zhang, et al. 2020). The pump frequency is controlled by the voltage-controlled oscillator (VCO) that drives the SSB-SC modulator, which scans over ~3 GHz in 150 ns from shorter to longer wavelength. Fig. 7.2**a** illustrates the simplified experimental setup. The optical spectra of signal (red) and local (blue) solitons are shown in Fig. 7.2**b**. No active locking technique is used in our experiments for stabilization.

An optical line-by-line waveshaper (Ferdous, Miao, et al. 2011) is used to control the phase of each comb line in the signal solitons (φ_n^S). The signal and local solitons are then combined in a 50/50 fiber coupler, and a second waveshaper is followed to control the amplitudes of each comb line pair (A_n^S, A_n^L). An erbium-doped fiber amplifier (EDFA) is used to amplify the solitons, and a high-speed, high-power photodiode converts the optical dual solitons into a zero offset RF frequency comb. The dual-comb optical spectrum after EDFA is measured on an optical spectrum analyzer, and an oscilloscope with 4 GHz bandwidth is used to characterize the RF temporal waveform, the spectrum of the RF comb, and the phase of the RF comb. Fig. 7.2**c** presents the measurements when no phase or power adjustments are added by the waveshapers, except compensating the dispersion introduced by optical fibers. This can serve as a reference point for line-by-line waveshaping in the RF domain. In our experiment, we purposely select a small RF comb spacing, $\Delta f_r = 150$ MHz, such that the analog bandwidth of the RF comb will not exceed the 4 GHz bandwidth limit of our oscilloscope. The analog bandwidth in our experiment is limited by the oscilloscope, not by the Nyquist frequency of coherent dual-comb sampling method (Coddington, W. Swann, and N. Newbury 2009) or the speed of the photodiode.

To illustrate line-by-line waveshaping in the RF domain, four types of Gaussian based temporal waveforms are demonstrated in Fig.7.2**d** to Fig.7.2**g**. The fundamental Gaussian waveform is shown in Fig.7.2**d**, which has a Gaussian envelope with flat phase in both frequency and temporal domains. The power and phase of the generated RF comb match the designed ones very well, which are shown in red circles. The corresponding temporal waveform is a Gaussian pulse train with a time period of 6.71 ns, peak voltage of 0.94 Volt, and pulse width of 235 ps. No electrical amplifier after the photodiode is used in this work. The number of pulses in one period can be doubled by knocking out half of the RF comb lines (Fig.7.2**e**). This is equivalent to adding an equidistant Gaussian pulse with the same amplitude in one temporal period. The amplitude of the added Gaussian pulse can be adjusted by changing the amplitude of the RF comb (Fig.7.2**f**). Finally, the temporal position of the added Gaussian pulse can be shifted by modifying both the amplitude and the phase of the RF comb lines (Fig. 7.2**g**). The demonstration of these four Gaussian waveforms illustrates the full control of amplitude and phase in our RF line-by-line shaping method.

One direct application of line-by-line waveshaping is arbitrary waveform generation. Three representative waveforms, including triangle, square, and ”UVA”-like wave-

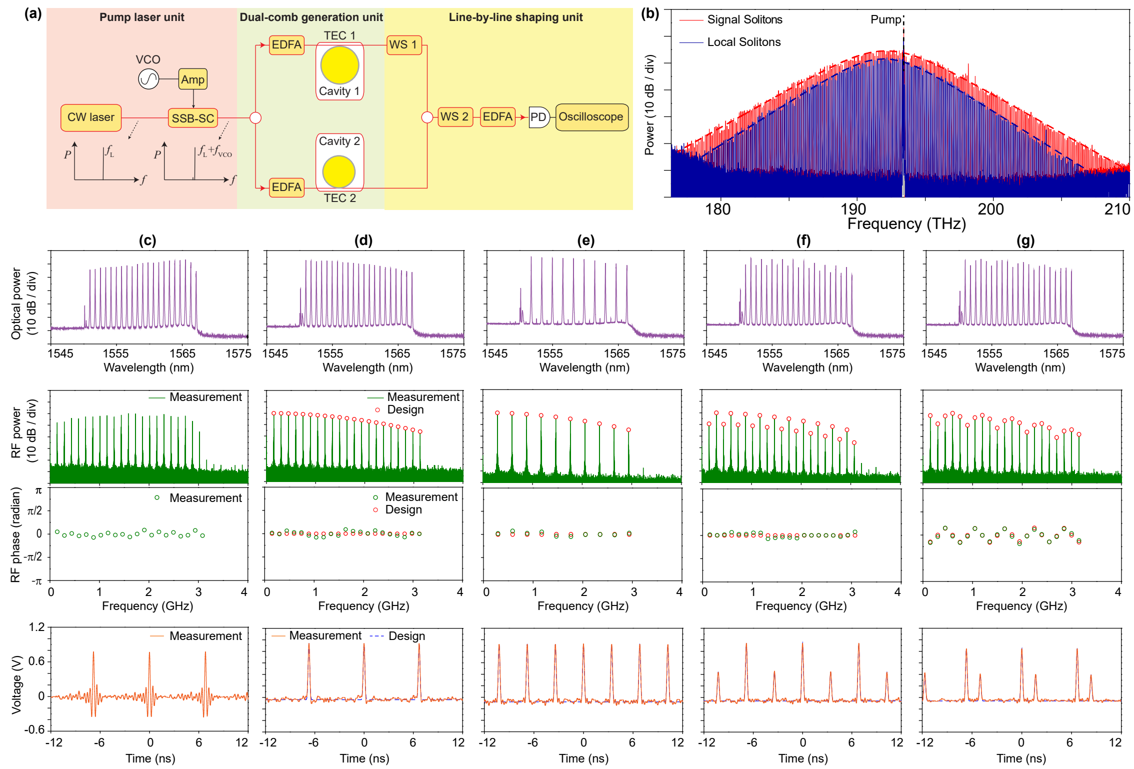

Figure 7.2: **Line-by-line waveshaping of RF Gaussian waveforms.** **(a)** Simplified experimental setup. The pump laser frequency is derived from the frequency of a continuous-wave (cw) laser, f_L, and the voltage-controlled oscillator (VCO), f_{VCO}. **(b)** Optical spectra of the signal (red) and local (blue) microresonator solitons. Sech^2 envelope fittings are shown in dash lines. The waveform synthesis is shown in panel **(c)** to **(g)** to illustrate the line-by-line control of amplitude and phase of the RF comb. **(c)** The reference dual-microcomb waveforms with only dispersion compensation. **(d)** Amplitude control of the RF comb lines to shape temporal waveforms into Gaussian pulses with 235 ps pulse width. **(e)** Further amplitude control to add an equidistant Gaussian pulse and double the RF comb repetition frequency. **(f)** Adjust the relative Gaussian amplitudes through comb line amplitude control. **(g)** Combined amplitude and phase control of the RF comb to tune the relative position of the two Gaussian pulses. From the top to bottom rows are: (i) the optical spectra of soliton dual-microcomb after waveshaping, (ii) the down-converted RF spectra, (iii) the phase of RF comb lines, and (iv) the temporal waveforms. Designed comb line powers and phases are shown in red circles, and the designed temporal waveforms are shown in dashed blue lines.

forms, are demonstrated here. For each temporal waveform, the corresponding amplitude and phase of each comb line can be derived by discrete Fourier transform of

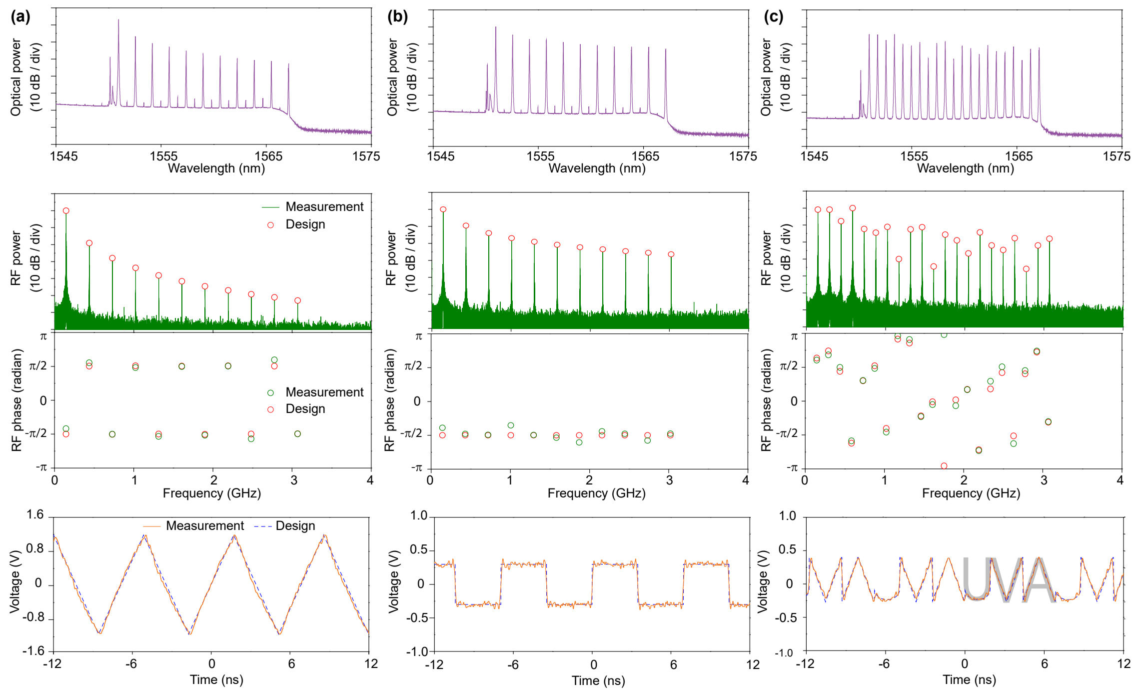

Figure 7.3: **Arbitrary waveform generation by using dual-microcomb RF Fourier synthesis. (a)** Triangle waveform. **(b)** Square waveform. **(c)** "UVA"-like waveform. The corresponding (i) optical spectra, (ii) RF spectra, (iii) comb line phases, and (iv) temporal waveforms are shown from top to bottom in each panel. Designed comb line powers and phases are shown in red circles, and the designed temporal waveforms are shown in dashed blue lines.

the temporal waveform. The Fourier transform of the triangle waveform is $x_{tr}(t) = \sum_{j=1}^{\infty} n^{-2} \cos\left(2\pi n \Delta f_r t + (-1)^j \pi/2\right)$, where j is integer number, and $n = 2j+1$. The triangle waveform only has comb lines with odd number n, where the phase of the comb line alternates between $-\pi/2$ and $\pi/2$, and the amplitude decays quadratically with the line number n. These features are well reproduced in the power and phase spectra (Fig.7.3**a**), and a triangle wave with period of 6.84 ns and 2.4 V peak to peak voltage is generated. Similarly, the square waveform is composed of comb lines with odd number: $x_{sq}(t) = \sum_{j=1}^{\infty} n^{-1} \cos\left(2\pi n \Delta f_r t - \pi/2\right)$. Fig.7.3**b** shows the measurements of the square waveform. Finally, a "UVA"-shaped waveform is shown in Fig.7.3**c** to illustrate that the waveform construction in our method is arbitrary. All three demonstrated waveforms agree very well with the designed waveforms.

7.4 Tuning of arbitrary waveform rep-rates

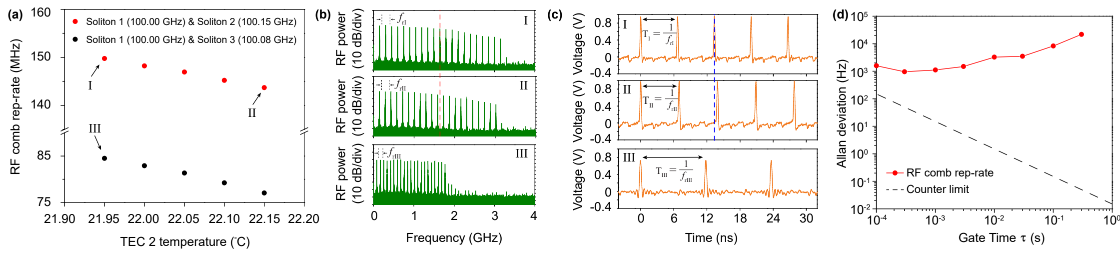

Figure 7.4: **Tuning the repetition frequency of the RF comb and temporal waveforms.** **(a)** The RF comb repetition frequency is tuned by adjusting the rep-rate of local solitons. Small range tuning is realized by tuning the temperature of the local soliton microresonator with a thermoelectric cooler (TEC). Large range tuning is accomplished by generating local solitons in a microresonator with a slightly different radius. Soliton repetition rates are indicated in the figure legend. Panel **(b)** and panel **(c)** show the electrical spectra and corresponding temporal waveforms at three different operating points indicated in panel **(a)**. **(d)** Allan deviation of RF comb repetition rate at point I in panel (a).

As the RF waveform repetition period is set by the repetition rate difference between the signal and local solitons, it can be tuned directly by adjusting the repetition rate of one of the solitons. Small range tuning of repetition period can be achieved by adjusting the temperature of the local soliton microresonator. Fig.7.4**a** presents the RF comb repetition rate versus the temperature of the local soliton microresonator and a tuning rate of ~ 30 MHz/°C is measured. The spectra and temporal profiles of two Gaussian waveforms at (I) 21.95 °C and (II) 22.15 °C are shown in Fig.7.4**b** and Fig.7.4**c**, where a difference of 0.29 ns in the waveform repetition periods can be seen. Large change of waveform period can be achieved by generating local solitons in a microresonator with slightly different radius. The RF comb rep-rate changes from ~ 150 MHz to ~ 85 MHz when the radius of local soliton microresonator is varied from 228.30 μm to 228.53 μm. Finally, Fig.7.4**d** presents the Allan deviation of the RF-comb repetition rate, which is subject to the pump laser frequency drift and environment temperature fluctuation in our free running system.

7.5 Figure of merits

7.5.1 Analog bandwidth

The ultrahigh analog bandwidth has been the key advantage of photonic AWG systems. 60 GHz analog bandwidth has been achieved previously using frequency-to-time mapping (Khan et al. 2010) and direct time-domain synthesis (Jian Wang et al. 2015). The analog bandwidth of the dual-comb Fourier synthesis method is ultimately limited by the Nyquist frequency of optical coherent sampling (Coddington, W. Swann, and N. Newbury 2009), i.e., half of the optical frequency comb repetition rate, and the bandwidth of the photodiode. The Nyquist frequency of dual-microcomb can range from a few GHz up to a few hundred GHz (Suh and Kerry Vahala 2018; Q. Li et al. 2017). The high Nyquist frequency has been applied to increase the bandwidth or sampling rate in dual-microcomb spectroscopy (Suh, Q.-F. Yang, et al. 2016; Dutt et al. 2018), Lidar (Suh and Kerry J Vahala 2018; Trocha et al. 2018) and imaging (Yi, Q.-F. Yang, K. Y. Yang, and Kerry Vahala 2018; Bao, Suh, and Kerry Vahala 2019). In terms of photodiodes, bandwidth exceeding 100s GHz has been demonstrated, and has been combined with soliton microcombs to generate RF signals with exceptional performance in power (B. Wang, J. S. Morgan, et al. 2021), phase noise (S. Zhang, Silver, Shang, et al. 2019; Tetsumoto, Ayano, et al. 2020) and time jitter (Jeong et al. 2020). It is thus possible to extend the analog bandwidth of dual-microcomb AWG beyond 100 GHz. In addition, all the critical components in dual-microcomb Fourier synthesis, including laser, Kerr microresonators, multiplexers/demultiplexers, modulators, amplifiers, and ultrafast photodiodes, have all been shown to be compatible with silicon photonics integration. Also, it eliminates the need of low-rate mode-locked lasers and long tunable delay lines required by the previous proposed on-chip solutions (Khan et al. 2010; Jian Wang et al. 2015; Tan et al. 2020), and has the potential of mass-production on a photonic chip.

7.5.2 Effective number of bits

An important figure of merit for RF arbitrary waveform generation is the effective number of bits (ENOB) (Kester 2009), which can be used to evaluate the waveform quality or the effective resolution of the waveforms. For our dual-comb AWG method, the fundamental limit of its ENOB is set by the optical power of the frequency combs. The fundamental limit of the ENOB in the dual-comb AWG method can be calculated using the ratio of signal voltage to the root-mean-square noise voltage fluctuations, and it is defined as: $2^{\mathrm{ENOB}} = V_p/\sqrt{2}V_\sigma$, where V_p is the time domain peak voltage, and V_σ^2 is the voltage noise variance. As harmonic distortion is not observed in our experiments, it is not included in our ENOB calculation. The digital quantization noise is not included either for our analog system. It should be noted that the widely used ENOB expression for sinusoidal waveforms (Kester 2009) agrees with our definition when excluding harmonic distortion and digital quantization noise. For the sinc-shaped waveform, where all comb lines are shaped into equal power, the ENOB can be expressed as the following when the noise variance is dominated by shot noise

(σ_S^2) and thermal noise (σ_T^2):

$$\begin{aligned}\text{ENOB} &= \frac{1}{2}\log_2\left[\frac{V_p^2}{2R_{load}^2(\sigma_S^2+\sigma_T^2)}\right] \\ &= \frac{1}{2}\log_2\left[\frac{2R^2\cdot N^2P_0^2}{(4e\cdot R\cdot NP_0+k_BT/R_{load})\cdot f_{\text{BW}}}\right],\end{aligned} \tag{7.1}$$

where we have used $V_p = 2R_{load}\cdot R\cdot NP_0$, $\sigma_S^2 = 4e\cdot R\cdot NP_0\cdot f_{\text{BW}}$, and $\sigma_T^2 = k_BT/R_{load}\cdot f_{\text{BW}}$. R_{load} is the load resistor of the photodiode, R is the the responsivity of the photodiode, N is the number of comb lines, P_0 is the optical power per comb line, e is electron charge, k_B is Boltzmann constant, T is the temperature, and f_{BW} is the total bandwidth. It can be seen that the ENOB increases with the total comb power (NP_0), but decreases with total bandwidth.

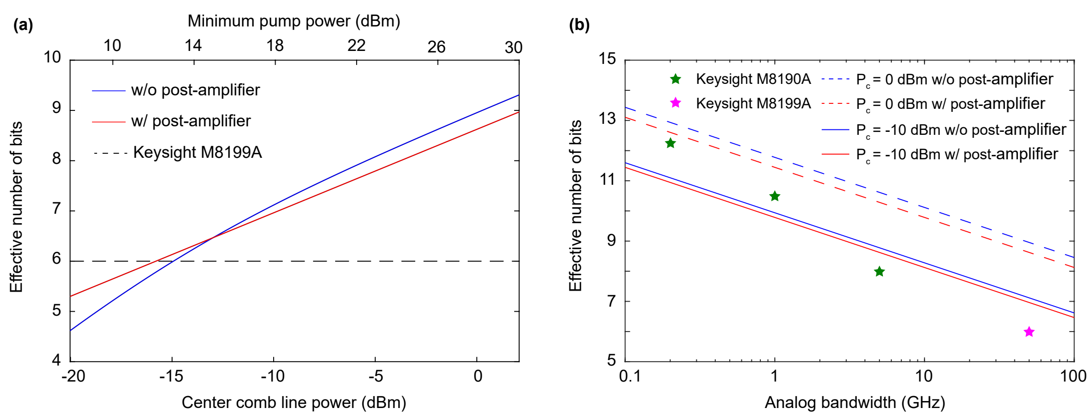

Figure 7.5: **Theoretical analysis of effective number of bits (ENOB). (a)** The theoretical limit of dual-comb AWG ENOB versus the comb line power for 50 GHz analog bandwidth. The minimum pump power required to achieve such comb line power in the single soliton microcomb state is also shown. In this calculation, we assume 3 dB loss between the microresonators and the photodiode, and 4 dB noise figure for the optical post-amplifier. **(b)** ENOB comparison of dual-comb AWG and state-of-the-art commercial electronic AWG.

For Kerr soliton microcombs, the comb line power at the envelope center (P_c) can be expressed as (Yi, Q.-F. Yang, K. Y. Yang, Suh, et al. 2015) $P_c = (0.8814\eta/N)^2 \times P_p^{\min}$, where P_p^{min} is the minimum pump power required for soliton existence, N is the number of one-sided comb lines in 3-dB spectrum bandwidth, and $\eta = Q/Q_e$ is the waveguide to resonator loading factor. Q_e is the external or coupling Q-factor and $Q = (Q_0^{-1} + Q_e^{-1})^{-1}$ is the total Q-factor (Q_0 is the intrinsic Q-factor). We can plot the fundamental limit of ENOB versus center comb line power (P_c) and the minimum pump power (P_p^{min}) for the sinc-shaped waveform, where the optical power per comb line is shaped to half of the center comb line power ($P_0 = P_c/2$). In fig. 7.5(a), the blue trace is obtained with the parameters of $\eta = 0.91$, $N = 20$, $f_{\text{BF}} = 50$ GHz, $R_{load} = 50\,\Omega$, responsivity (Q. Yu et al. 2020) $R = 0.8$ A/W, and 3 dB insertion loss (1 dB from phase and intensity modulators (C. Wang et al. 2018), 2dB from wavelength demultiplexer and multiplexer (Bauters et al. 2014)) between the resonators and the photodiode. It can be seen that for comb line power below -10 dBm, the ENOB is affected by photodiode thermal noise, which can be addressed by using an optical post-amplifier to amplify the dual-comb power (red trace). A noise figure of 4 dB is assumed for the post-amplifier in the calculation of the ENOB. The ENOB of Keysight M8199A at 50 GHz is indicated with dash line in Fig. 7.5(a). It should be noted that ENOB for electronic AWG is typically measured for the sinusoidal waveform instead of the sinc waveform, and thus here it only serves as a rough reference for our photonic AWG analysis. The ENOB versus analog bandwidth is shown in Fig. 7.5(b) for center comb line power of 0 dBm (dashed) and -10 dBm (solid). The ENOB of our experiment (≈ 4) is much lower than the theoretical limit, because of the high loss in our optical path and the transmitted ASE noise from the pump EDFAs before microresonators. Both of these can be addressed in a fully integrated system.

ENOB analysis

The optical field of an N-pair dual-comb can be expressed as:

$$E = \sum_{n=1}^{N} \sqrt{P_n^S} \exp[-i(w_n^S t - \varphi_n^S)] + \sum_{n=1}^{N} \sqrt{P_n^L} \exp[-i(w_n^L t - \varphi_n^L)], \tag{7.2}$$

where $\omega_n^{S,L}$, $P_n^{S,L}$ and $\varphi_n^{S,L}$ are the n-th comb line's frequency, power, and phase of the signal (S) and local (L) combs. The photocurrent generated at the photodiode can be expressed as:

$$\begin{aligned} I_{ph} &= R|E|^2 + \Delta I_S + \Delta I_T \\ &= R\sum_{n=1}^{N}(P_n^S + P_n^L) + 2R\sum_{n=1}^{N} \sqrt{P_n^S P_n^L} \cos[2\pi n \Delta f_r t + (\varphi_n^S - \varphi_n^L)] + \Delta I_S + \Delta I_T + \cdots , \end{aligned} \tag{7.3}$$

where R is the responsivity of the photodiode, and $2\pi n\Delta f_r = \omega_n^L - \omega_n^S$ are the frequency differences of n-th lines of signal combs and local combs. ΔI_S and ΔI_T are the current fluctuations caused by the shot noise and thermal noise, respectively. In our experiments, the dark current noise can be neglected (10 nA for our PD, Finisar VPDV2120). The first term in the second line of Eq. (7.3) corresponds to the DC photocurrent, and the second term corresponds to the AC photocurrent for the down-converted RF comb. Higher frequency terms beyond the Nyquist bandwidth (Coddington, W. Swann, and N. Newbury 2009), such as harmonics of comb repetition frequencies, are neglected. For the analysis of signal-to-noise ratio (SNR) and effective number of bits (ENOB) (Kester 2009), we assume a flat spectrum for the dual-comb for simplicity, i.e., $P_n^S = P_n^L = P_0$. The AC voltage output is then given by:

$$V_{AC} = 2R_{load} \cdot RP_0 \sum_{n=1}^{N} \cos[2\pi n \Delta f_r t + (\varphi_n^S - \varphi_n^L)], \tag{7.4}$$

where R_{load} (50 Ω) is the load resistor. For the sinc-shaped waveform, we will have $\varphi_n^S = \varphi_n^L$, and the peak voltage will occur when $t = M/\Delta f_r$, where M is an integer number. The peak voltage can be expressed as:

$$V_p = 2R_{load} \cdot R \cdot NP_0. \tag{7.5}$$

The variances from shot noise and thermal noise, and their total variance are given by:

$$\sigma_S^2 = 2e \cdot I_{DC} \cdot f_{\mathrm{BW}}, \tag{7.6}$$

$$\sigma_T^2 = k_B T/R_{load} \cdot f_{\mathrm{BW}}, \tag{7.7}$$

$$\sigma^2 = \sigma_S^2 + \sigma_T^2, \tag{7.8}$$

where e is the charge of an electron, $I_{DC} = 2R \cdot NP_0$ is DC photocurrent, f_{BW} is the bandwidth of photodiode (or the total bandwidth, assuming photodiode bandwidth is equal to or larger than the Nyquist bandwidth), k_B is the Boltzmann constant, and T is the temperature (300 K in the lab environment).

The ENOB of the demonstrated waveform can be calculated using the ratio of the signal peak voltage to the root-mean-square noise voltage fluctuations (Kester 2009):

$$\frac{V_p/\sqrt{2}}{V_\sigma} = 2^{\mathrm{ENOB}} \Leftrightarrow \mathrm{ENOB} = \log_2\left(\frac{V_p/\sqrt{2}}{R_{load} \cdot \sigma}\right), \tag{7.9}$$

where we have used $V_\sigma = R_{load} \cdot \sigma$. By plugging Eqs. (7.5 - 7.8) into Eq. (7.9), the expression of ENOB is given by:

$$\mathrm{ENOB} = \frac{1}{2}\log_2\left[\frac{2R^2 \cdot N^2 P_0^2}{\sigma^2}\right] = \frac{1}{2}\log_2\left[\frac{2R^2 \cdot N^2 P_0^2}{(4e \cdot R \cdot NP_0 + k_B T/R_{load}) \cdot f_{\mathrm{BW}}}\right]. \tag{7.10}$$

The ENOB increases with the number of comb pairs N and comb line power P_0, and decreases with the electrical bandwidth.

Our definition of ENOB agrees with the common ENOB definition in electronic AWG for sinusoidal waveform, which is given by (Kester 2009):

$$\mathrm{ENOB} = \frac{\mathrm{SINAD} - 1.76}{6.02}, \tag{7.11}$$

where $\mathrm{SINAD} = P_{signal}/(P_{noise} + P_{distortion})$ is the signal-to-noise and distortion ratio, and $1.76/6.02 \approx 0.29$ comes from the quantization error in an ideal digital-to-analog converter (DAC)/analog-to-digital converter (ADC). When excluding the effect of harmonics distortion and digital quantization error, Eq. (7.11) becomes:

$$\mathrm{ENOB} = \frac{\mathrm{SNR}}{6.02} = \frac{10\log_{10}(V_{sig-rms}/V_\sigma)^2}{20\log_{10}2} = \log_2(V_{sig-rms}/V_\sigma) = \log_2(V_p/\sqrt{2}V_\sigma), \tag{7.12}$$

which is the same as our ENOB definition in Eq. (7.12).

ENOB and soliton microcomb power

For bright dissipative Kerr cavity solitons, the center comb line power can be expressed (Herr, Brasch, et al. 2014; Yi, Q.-F. Yang, K. Y. Yang, Suh, et al. 2015) as a function of cavity second-order dispersion D_2 and external coupling rate κ_{ext}:

$$P_c = \frac{\hbar\omega_0}{4g}\kappa_{ext}D_2 = \frac{\pi n_0 S_{eff}}{2\omega_0 n_2 D_1}\kappa_{ext}D_2, \tag{7.13}$$

where $g = \hbar\omega_0^2 c n_2/n_0^2 V_{eff}$ is the Kerr nonlinear coefficient and $V_{eff} = 2\pi c S_{eff}/n_0 D_1$ is the effective cavity mode volume. $\hbar$, ω_0, c, n_0, n_2, S_{eff}, D_1 are the plank constant, cavity mode angular frequency, speed of light, refractive index, Kerr nonlinear refractive index, effective mode area and free spectral range, respectively. P_c increases with the product of κ_{ext} and D_2. For a given soliton pulse width τ_s, the minimum pump power for the soliton state is given by (Yi, Q.-F. Yang, K. Y. Yang, Suh, et al. 2015):

$$P_{pump}^{min} = -\frac{2c}{\pi}\frac{S_{eff}\beta_2}{\omega_0 n_2 D_1}\frac{\kappa^2}{\kappa_{ext}}\frac{1}{\tau_s^2} = \frac{2}{\pi}\frac{n_0 S_{eff}}{\omega_0 n_2}\frac{D_2}{D_1^3}\frac{(\kappa_0+\kappa_{ext})^2}{\kappa_{ext}}\frac{1}{\tau_s^2}, \tag{7.14}$$

where $\beta_2 = -n_0 D_2/cD_1^2$ is the group velocity dispersion, and κ_0 is the cavity intrinsic loss rate. Combining Eq. (7.13) and Eq. (7.14), the center comb line power can be expressed as a function of the minimum pump power:

$$P_c = \left(\frac{\eta\pi D_1\tau_s}{2}\right)^2 P_{pump}^{min}, \tag{7.15}$$

where we have used resonator-waveguide coupling strength coefficient $\eta = \kappa_{ext}/(\kappa_0 + \kappa_{ext})$. For the sech^2-shaped soliton microcomb, its comb power spectral envelope is given by:

$$P(\Delta\omega) = P_c \cdot \mathrm{sech}^2\left(\frac{\pi\tau_s}{2}\Delta\omega\right), \tag{7.16}$$

where $\Delta\omega$ is the comb tooth frequency relative to the comb center frequency. Assuming that within 3-dB spectral bandwidth there are N single-sided comb lines, we can then obtain:

$$\mathrm{sech}^2\left(\frac{\pi\tau_s}{2}ND_1\right) = \frac{1}{2} \Leftrightarrow \frac{\pi D_1\tau_s}{2} = \frac{0.8814}{N}. \tag{7.17}$$

Therefore, Eq. (7.15) can be expressed as:

$$P_c = \left(\frac{0.8814\eta}{N}\right)^2 P_{pump}^{min}, \tag{7.18}$$

In our experiment, these N comb lines can be used for line-by-line Fourier synthesis.

For sinc-shaped waveform, the power of each comb line is set to the weakest comb line power, i.e., 3 dB lower than that of the center comb line. Also, considering the total insertion loss of optical components (such as wavelength demultiplexer/multiplexer, phase/intensity modulators) between microresonators and photodiodes, the actual comb line power received by the photodiode can be expressed as:

$$P_0 = \alpha \times \frac{P_c}{2}, \tag{7.19}$$

where α is the efficiency from resonators to detectors. By plugging Eqs. (7.18)-(7.19) into Eq. (7.10), ENOB can be expressed as:

$$\begin{aligned} \text{ENOB} &= \frac{1}{2}\log_2\left[\frac{R^2 \cdot \alpha^2 N^2 P_c^2}{2(2e \cdot R \cdot \alpha N P_c + k_B T/R_{load}) \cdot f_{\text{BW}}}\right] \\ &= \frac{1}{2}\log_2\left[\frac{(0.8814\eta)^4 \cdot R^2 \cdot \alpha^2 P_{pump}^{min\ 2}}{2[2(0.8814\eta)^2 \cdot e \cdot R \cdot \alpha P_{pump}^{min}/N + k_B T/R_{load}]N^2 \cdot f_{\text{BW}}}\right]. \end{aligned} \tag{7.20}$$

Eq. (7.20) is used for plotting ENOB without amplifier in Fig. 5**a** and Fig. 5**b**.

ENOB after optical amplification

If an optical amplifier, i.e. erbium-doped fiber amplifier (EDFA), is placed before the photodiode for amplifying the comb line power, the output optical power per comb line P_{0A} is given by:

$$P_{0A} = P_0 G, \tag{7.21}$$

where G is the gain of the amplifier and we assume it is constant over the entire amplifier bandwidth. The spectral density of amplified spontaneous emission (ASE) noise is given by (Heffner 1962; Kogelnik and Yariv 1964; G. Agrawal 2001; Becker, Olsson, and Simpson 1999):

$$S_{ASE} = \frac{1}{2}(F_n G - 1)h\nu, \tag{7.22}$$

where F_n is the amplifier noise figure, h is the Planck constant, and ν is the frequency of input signal. Given that the amplifier bandwidth ($\Delta\nu$) is much smaller than the frequency of light ($\Delta\nu \ll \nu$), the spectral density of ASE noise can be treated as a constant, i.e., $S_{ASE} = 1/2 \times (F_n G - 1)h\nu_0$, where ν_0 is the center frequency of the amplifier operating band. The total power of ASE noise over the entire amplifier bandwidth $\Delta\nu$ is given by:

$$P_{ASE} = 2 \times S_{ASE} \times \Delta\nu = (F_n G - 1)h\nu_0 \times \Delta\nu, \tag{7.23}$$

where the factor of 2 includes both orthogonal polarization modes supported in a single-mode fiber. When dividing the ASE bandwidth $\Delta\nu$ into K bins (G. P. Agrawal 2005; Desurvire and M. N. Zervas 1995; Becker, Olsson, and Simpson 1999) and each bin has a bandwidth of $\delta\nu = \Delta\nu/K$, we can express the optical field of the ASE noise as:

$$E_{ASE} = (S_{ASE}\delta\nu)^{1/2} \sum_{k=1}^{K} \exp[-i(\omega_k t - \varphi_k)]. \tag{7.24}$$

The photocurrent generated at the photodiode can be modified as:

$$I_{ph} = R|\sqrt{G}E + E_{ASE}|^2 + \Delta I_S + \Delta I_T. \tag{7.25}$$

While the thermal noise variance σ_T^2 remains the same as before, the shot noise variance of the amplified light now becomes:

$$\sigma_S^2 = \sigma_{S_{comb}}^2 + \sigma_{S_{ASE}}^2 = 2e \cdot R(2NP_0G + P_{ASE}) \cdot f_{\mathrm{BW}}, \tag{7.26}$$

which has optical power contributed from both the amplified comb signals and the ASE noise. Besides the shot noise, from Eq. (7.25), the ASE noise field can also induce extra noise current I_{ASE}, which includes the ASE field photomixing with the amplified signal (I_{sig-sp}), and ASE field photomixing with itself (I_{sp-sp}):

$$I_{ASE} = I_{sig-sp} + I_{sp-sp}, \tag{7.27}$$

$$\begin{aligned} I_{sig-sp} &= R(\sqrt{G}EE_{ASE}^* + \sqrt{G}E^*E_{ASE}) \\ &= 2R\sqrt{G}(S_{ASE}\delta\nu)^{1/2}\sum_{k=1}^{K}\left(\sum_{n=1}^{N}A_n^S\cos[(\omega_n^S-\omega_k)t+\varphi_k-\varphi_n^S]+\sum_{n=1}^{N}A_n^L\cos[(\omega_n^L-\omega_k)t+\varphi_k-\varphi_n^L]\right) \\ &= 2R\sqrt{G}A_0(S_{ASE}\delta\nu)^{1/2}\sum_{k=1}^{K}\left(\sum_{n=1}^{N}\cos[(\omega_n^S-\omega_k)t+\varphi_k-\varphi_n^S]+\sum_{n=1}^{N}\cos[(\omega_n^L-\omega_k)t+\varphi_k-\varphi_n^L]\right), \end{aligned} \tag{7.28}$$

$$\begin{aligned} I_{sp-sp} &= R \cdot E_{ASE}E_{ASE}^* \cdot 2 \\ &= 2RS_{ASE}\delta\nu\sum_{k=1}^{K}\exp[-i(\omega_k t-\varphi_k)]\sum_{l=1}^{K}\exp[i(\omega_l t-\varphi_l)] \\ &= 2RS_{ASE}\delta\nu\sum_{k=1}^{K}\sum_{l=1}^{K}\cos[(\omega_k-\omega_l)t+\varphi_l-\varphi_k], \end{aligned} \tag{7.29}$$

where the factor of 2 in I_{sp-sp} includes both two orthogonal polarization modes. Note that only terms with their frequencies within the photodiode bandwidth should be kept in the calculation, i.e., $|\omega_n^{S(L)} - \omega_k| \le f_{\mathrm{BW}}$ and $|\omega_k - \omega_l| \le f_{\mathrm{BW}}$. To derive the variances, we can first calculate the average values of I_{sig-sp} and I_{sp-sp}:

$$< I_{sig-sp} >= 0, \tag{7.30}$$

$$< I_{sp-sp} >= 2RS_{ASE}\delta\nu K = 2RS_{ASE}\Delta\nu = R \cdot P_{ASE}, \tag{7.31}$$

where we have considered the phase of ASE noise $\varphi_{k(l)}$ fluctuates with time. The expected values of I^2_{sig-sp}, I^2_{sp-sp} are given by:

$$\begin{aligned}
&< I^2_{sig-sp} >= 4R^2P_0GS_{ASE}\delta\nu \overline{\left[\sum_{k=1}^{K}\left(\sum_{n=1}^{N}\cos[(\omega_n^S-\omega_k)t+\varphi_k-\varphi_n^S]+\sum_{n=1}^{N}\cos[(\omega_n^L-\omega_k)t+\varphi_k-\varphi_n^L]\right)\right]^2}\\
&= 4R^2P_0GS_{ASE}\delta\nu \times (\frac{2f_{\mathrm{BW}}}{\delta\nu}\cdot 2N\cdot\frac{1}{2}) = 4R^2\cdot(2NP_0G)S_{ASE}\cdot f_{\mathrm{BW}},
\end{aligned} \tag{7.32}$$

$$\begin{aligned}
&< I^2_{sp-sp} >= 4R^2S^2_{ASE}\delta\nu^2 \overline{\left(\sum_{k=1}^{K}\sum_{l=1}^{K}\cos[(\omega_k-\omega_l)t+\varphi_l-\varphi_k]\right)^2}\\
&= 4R^2S^2_{ASE}\delta\nu^2 \times \left[K\cdot\frac{2f_{\mathrm{BW}}}{\delta\nu}-\frac{f_{\mathrm{BW}}}{\delta\nu}(\frac{f_{\mathrm{BW}}}{\delta\nu}-1)\right]\times\frac{1}{2}+4R^2S^2_{ASE}\delta\nu^2\times K^2\\
&\approx 4R^2S^2_{ASE}\delta\nu^2 \times \left[2K\cdot\frac{f_{\mathrm{BW}}}{\delta\nu}-(\frac{f_{\mathrm{BW}}}{\delta\nu})^2\right]\times\frac{1}{2}+4R^2S^2_{ASE}\delta\nu^2\times K^2\\
&= 4R^2S^2_{ASE}\cdot f_{\mathrm{BW}}(\Delta\nu-f_{\mathrm{BW}}/2)+4R^2S^2_{ASE}\Delta\nu^2,
\end{aligned} \tag{7.33}$$

where $f_{\mathrm{BW}}/\delta\nu$ represents the number of frequency bins within PD bandwidth. $2f_{\mathrm{BW}}/\delta\nu\cdot 2N$ is the number of terms whose frequencies fall within PD bandwidth for I^2_{sig-sp}. $K\cdot 2f_{\mathrm{BW}}/\delta\nu-(f_{\mathrm{BW}}/\delta\nu)(f_{\mathrm{BW}}/\delta\nu+1)$ and K^2 are the numbers of terms whose frequencies fall within PD bandwidth for I^2_{sp-sp} when $k\neq l$ and when $k=l$, respectively. As a result, the variances can be expressed as (G. P. Agrawal 2005; Desurvire and

M. N. Zervas 1995; Becker, Olsson, and Simpson 1999):

$$\sigma^2_{sig-sp} =< I^2_{sig-sp} > - < I_{sig-sp} >^2 = 8R^2NP_0GS_{ASE} \cdot f_{\mathrm{BW}}, \tag{7.34}$$

$$\sigma^2_{sp-sp} =< I^2_{sp-sp} > - < I_{sp-sp} >^2 = 4R^2S^2_{ASE} \cdot f_{\mathrm{BW}}(\Delta\nu - f_{\mathrm{BW}}/2). \tag{7.35}$$

The total noise variance after optical amplification is:

$$\sigma^2_A = \sigma^2_S + \sigma^2_{sig-sp} + \sigma^2_{sp-sp} + \sigma^2_T. \tag{7.36}$$

The ENOB after amplification can be expressed as:

$$\begin{aligned} \mathrm{ENOB}_A &= \frac{1}{2}\log_2\left[\frac{2R^2 \cdot N^2P_0^2G^2}{\sigma^2_A}\right] \\ &= \frac{1}{2}\log_2\left[\frac{2R^2 \cdot N^2P_0^2G^2}{[4eRNP_0G + R(F_nG-1)h\nu_0(2e\Delta\nu + 4RNP_0G + R(F_nG-1)h\nu_0(\Delta\nu - f_{\mathrm{BW}}/2)) + k_BT}\right. \end{aligned} \tag{7.37}$$

To simply this expression, three noise terms can be neglected with confidence. The first is the shot noise of ASE, since the optical power of ASE is usually much smaller than the optical power of amplified comb lines. The second is the photomixing of ASE field with itself, which can be significantly suppressed using optical filters. The last term is the shot noise of amplified comb lines, as it is found to be always much smaller than the noise contributed from the photomixing of the ASE field and the amplified signal field:

$$\sigma^2_{S,comb} = 4eRNP_0G \cdot f_{\mathrm{BW}} \ll 4\eta_{pd} \cdot eRNP_0G(F_nG-1) \cdot f_{\mathrm{BW}} = \sigma^2_{sig-sp}, \tag{7.38}$$

where we have used amplifier gain $G \gg 1$, and the expression of responsivity $R =$

$\eta_{pd} \cdot e/h\nu$, η_{pd} is the quantum efficiency of the photodiode. The amplifier noise figure F_n is usually bigger than 2 (3 dB in log scale). Then the remaining noise sources only include the thermal noise, and the noise from the photomixing between the ASE field and the amplified signal field. Eq. (7.37) can be reduced to:

$$\begin{aligned}\mathrm{ENOB}_A &\approx \frac{1}{2}\log_2\left[\frac{2R^2 \cdot N^2 P_0^2 G^2}{[4\eta_{pd} \cdot eR(F_n G - 1)NP_0 G + k_B T/R_{load}] \cdot f_{\mathrm{BW}}}\right] \\ &\approx \frac{1}{2}\log_2\left[\frac{2R^2 \cdot N^2 P_0^2 G^2}{[4\eta_{pd} \cdot eRF_n G^2 NP_0 + k_B T/R_{load}] \cdot f_{\mathrm{BW}}}\right].\end{aligned} \tag{7.39}$$

Plugging Eqs. (7.18,7.19,7.21) into Eq. (7.39), ENOB after amplification can be expressed as:

$$\begin{aligned}\mathrm{ENOB}_A &= \frac{1}{2}\log_2\left[\frac{R^2 \cdot \alpha^2 N^2 P_c^2 G^2}{2[2\eta_{pd} \cdot eRF_n G^2 \alpha NP_c + k_B T/R_{load}] \cdot f_{\mathrm{BW}}}\right] \\ &= \frac{1}{2}\log_2\left[\frac{(0.8814\eta)^4 \cdot R^2 \cdot \alpha^2 {P_{pump}^{min}}^2 G^2}{2[2(0.8814\eta)^2\eta_{pd} \cdot eR \cdot F_n G^2 \cdot \alpha P_{pump}^{min}/N + k_B T/R_{load}]N^2 \cdot f_{\mathrm{BW}}}\right].\end{aligned} \tag{7.40}$$

Eq. (7.40) is used for plotting ENOB with amplifier in Fig. 5**a** and Fig. 5**b**.

7.5.3 Time-bandwidth product

Finally, the time-bandwidth product (TBWP) of our current static arbitrary waveform demonstration is limited by the number of comb lines, which gives a maximum TBWP of 20. In contrast, a TBWP of 600 has been demonstrated by combining frequency-to-time mapping and optical interferometry (Rashidinejad and Weiner 2014). In the future, the TBWP of our method can be increased dramatically by replacing the static waveshaper with phase and amplitude modulators for dynamic line-by-line phase and amplitude control (C. Wang et al. 2018; Geisler et al. 2009; Yin et al. 2021), and the time aperture of the waveforms will be directly set by the time aperture of modulation signals.

7.6 Summary

In summary, we demonstrated arbitrary RF waveform generation through spectral line-by-line shaping with optical dual-microresonator solitons. In our experiment, the analog bandwidth of the waveform is 3 GHz, which is set purposely such that the waveform bandwidth will not exceed our oscilloscope bandwidth. The waveform analog bandwidth in our dual-microcomb method can be conveniently increased by adjusting the FSR difference between the two soliton microresonators, which can be precisely controlled in microfabrication. In addition, although the demonstrated waveform generation is periodic and static, dynamic waveform generation can be implemented by using time varying amplitude and phase modulation of the optical comb lines through integrated photonic modulators (C. Wang et al. 2018; Geisler et al. 2009; Yin et al. 2021).

Bibliography

Heffner, H (1962). “The fundamental noise limit of linear amplifiers”. In: *Proceedings of the IRE* 50.7, pp. 1604–1608.

Kogelnik, H and A Yariv (1964). “Considerations of noise and schemes for its reduction in laser amplifiers”. In: *Proceedings of the IEEE* 52.2, pp. 165–172.

Lugiato, Luigi A and René Lefever (1987). “Spatial dissipative structures in passive optical systems”. In: *Phys. Rev. Lett.* 58.21, p. 2209.

Gorodetsky, ML and VS Ilchenko (1994). “High-Q optical whispering-gallery microresonators: precession approach for spherical mode analysis and emission patterns with prism couplers”. In: *Optics Communications* 113.1-3, pp. 133–143.

Desurvire, Emmanuel and Michael N Zervas (1995). “Erbium-doped fiber amplifiers: principles and applications”. In: *Physics Today* 48.2, p. 56.

Gorodetsky, Mikhail L, Anatoly A Savchenkov, and Vladimir S Ilchenko (1996). “Ultimate Q of optical microsphere resonators”. In: *Optics letters* 21.7, pp. 453–455.

Becker, Philippe M, Anders A Olsson, and Jay R Simpson (1999). *Erbium-doped fiber amplifiers: fundamentals and technology.* Elsevier.

Holzwarth, R et al. (2000). “Optical frequency synthesizer for precision spectroscopy”. In: *Phys. Rev. Lett.* 85.11, p. 2264.

Jones, David J et al. (2000). “Carrier-envelope phase control of femtosecond mode-locked lasers and direct optical frequency synthesis”. In: *Science* 288.5466, pp. 635–639.

Minoshima, Kaoru and Hirokazu Matsumoto (2000). “High-accuracy measurement of 240-m distance in an optical tunnel by use of a compact femtosecond laser”. In: *Applied Optics* 39.30, pp. 5512–5517.

Agrawal, Govind (2001). *Applications of nonlinear fiber optics*. Elsevier.

Diddams, SA, Th Udem, et al. (2001). “An optical clock based on a single trapped $^{199}Hg^{+}$ ion”. In: *Science* 293.5531, pp. 825–828.

Udem, Th, Ronald Holzwarth, and Theodor W Hänsch (2002). “Optical frequency metrology”. In: *Nature* 416.6877, pp. 233–237.

Cundiff, Steven T and Jun Ye (2003). “Colloquium: Femtosecond optical frequency combs”. In: *Rev. Mod. Phys.* 75.1, p. 325.

Goswami, Debabrata (2003). “Optical pulse shaping approaches to coherent control”. In: *Physics Reports* 374.6, pp. 385–481.

Spillane, SM et al. (2003). “Ideality in a fiber-taper-coupled microresonator system for application to cavity quantum electrodynamics”. In: *Physical review letters* 91.4, p. 043902.

Vahala, Kerry J (2003). “Optical microcavities”. In: *Nature* 424.6950, pp. 839–846.

Altug, Hatice and Jelena Vučković (2004). “Two-dimensional coupled photonic crystal resonator arrays”. In: *Applied Physics Letters* 84.2, pp. 161–163.

Diddams, SA, JC Bergquist, et al. (2004). “Standards of time and frequency at the outset of the 21st century”. In: *Science* 306.5700, pp. 1318–1324.

Kippenberg, TJ, SM Spillane, and KJ Vahala (2004). “Kerr-nonlinearity optical parametric oscillation in an ultrahigh-Q toroid microcavity”. In: *Physical Review Letters* 93.8, p. 083904.

Kippenberg, Tobias Jan August (2004). *Nonlinear optics in ultra-high-Q whispering-gallery optical microcavities*. California Institute of Technology.

Ma, Long-Sheng et al. (2004). “Optical frequency synthesis and comparison with uncertainty at the 10-19 level”. In: *Science* 303.5665, pp. 1843–1845.

Agrawal, Govind P (2005). *Lightwave technology: telecommunication systems*. John Wiley & Sons.

Jiang, Zhi, DS Seo, et al. (2005). “Spectral line-by-line pulse shaping”. In: *Optics letters* 30.12, pp. 1557–1559.

Lin, Ingrid S, Jason D McKinney, and Andrew M Weiner (2005). “Photonic synthesis of broadband microwave arbitrary waveforms applicable to ultra-wideband communication”. In: *IEEE Microwave and Wireless Components Letters* 15.4, pp. 226–228.

Matsko, AB et al. (2005). “Review of applications of whispering-gallery mode resonators in photonics and nonlinear optics”. In: *IPN Progress Report* 42.162, pp. 1–51.

Fortier, Tara M, Albrecht Bartels, and Scott A Diddams (2006). “Octave-spanning Ti: sapphire laser with a repetition rate> 1 GHz for optical frequency measurements and comparisons”. In: *Optics letters* 31.7, pp. 1011–1013.

Stowe, Matthew C et al. (2006). “High resolution atomic coherent control via spectral phase manipulation of an optical frequency comb”. In: *Physical review letters* 96.15, p. 153001.

Agrawal, Govind P (2007). *Nonlinear fiber optics*. Academic press.

Capmany, José and Dalma Novak (2007). “Microwave photonics combines two worlds”. In: *Nature photonics* 1.6, p. 319.

Del’Haye, P et al. (2007). “Optical frequency comb generation from a monolithic microresonator”. In: *Nature* 450.7173, pp. 1214–1217.

Diddams, Scott A, Leo Hollberg, and Vela Mbele (2007). "Molecular fingerprinting with the resolved modes of a femtosecond laser frequency comb". In: *Nature* 445.7128, pp. 627–630.

Jiang, Zhi, Chen-Bin Huang, et al. (2007). "Optical arbitrary waveform processing of more than 100 spectral comb lines". In: *Nature Photonics* 1.8, pp. 463–467.

Rabus, Dominik G (2007). *Integrated ring resonators*. Springer.

Rafailov, Edik U, Maria Ana Cataluna, and Wilson Sibbett (2007). "Mode-locked quantum-dot lasers". In: *Nature photonics* 1.7, pp. 395–401.

Akhmediev, N and A Ankiewicz (2008). *Dissipative Solitons: From Optics to Biology and Medicine*.

Coddington, Ian, William C Swann, and Nathan R Newbury (2008). "Coherent multiheterodyne spectroscopy using stabilized optical frequency combs". In: *Physical Review Letters* 100.1, p. 013902.

Cooper, Ken B et al. (2008). "Penetrating 3-D imaging at 4-and 25-m range using a submillimeter-wave radar". In: *IEEE Transactions on Microwave Theory and Techniques* 56.12, pp. 2771–2778.

De Lucia, Frank C, Douglas T Petkie, and Henry O Everitt (2008). "A double resonance approach to submillimeter/terahertz remote sensing at atmospheric pressure". In: *IEEE journal of quantum electronics* 45.2, pp. 163–170.

Steinmetz, Tilo et al. (2008). "Laser frequency combs for astronomical observations". In: *Science* 321.5894, pp. 1335–1337.

Bartels, Albrecht, Dirk Heinecke, and Scott A Diddams (2009). "10-GHz self-referenced optical frequency comb". In: *Science* 326.5953, pp. 681–681.

Coddington, I, WC Swann, and NR Newbury (2009). "Coherent linear optical sampling at 15 bits of resolution". In: *Optics letters* 34.14, pp. 2153–2155.

Coddington, I, William C Swann, et al. (2009). “Rapid and precise absolute distance measurements at long range”. In: *Nature photonics* 3.6, pp. 351–356.

Ferdous, Fahmida, Daniel E Leaird, et al. (2009). “Dual-comb electric-field cross-correlation technique for optical arbitrary waveform characterization”. In: *Optics letters* 34.24, pp. 3875–3877.

Geisler, David J et al. (2009). “Modulation-format agile, reconfigurable Tb/s transmitter based on optical arbitrary waveform generation”. In: *Optics express* 17.18, pp. 15911–15925.

Gondarenko, Alexander, Jacob S Levy, and Michal Lipson (2009). “High confinement micron-scale silicon nitride high Q ring resonator”. In: *Optics express* 17.14, pp. 11366–11370.

Kester, Walt (2009). “Understand SINAD, ENOB, SNR, THD, THD+ N, and SFDR so you don’t get lost in the noise floor”. In: *MT-003 Tutorial, www. analog. com/static/importedfiles/tutorials/MT-003. pdf.*

Yao, Jianping (2009). “Microwave photonics”. In: *Journal of lightwave technology* 27.3, pp. 314–335.

Chembo, Yanne K and Nan Yu (2010). “Modal expansion approach to optical-frequency-comb generation with monolithic whispering-gallery-mode resonators”. In: *Physical Review A* 82.3, p. 033801.

Cundiff, Steven T and Andrew M Weiner (2010). “Optical arbitrary waveform generation”. In: *Nature Photonics* 4.11, pp. 760–766.

Diddams, Scott A (2010). “The evolving optical frequency comb”. In: *JOSA B* 27.11, B51–B62.

Hofer, Johannes, Albert Schliesser, and Tobias J Kippenberg (2010). “Cavity optomechanics with ultrahigh-Q crystalline microresonators”. In: *Physical Review A* 82.3, p. 031804.

Khan, Maroof H et al. (2010). “Ultrabroad-bandwidth arbitrary radiofrequency waveform generation with a silicon photonic chip-based spectral shaper”. In: *Nature Photonics* 4.2, pp. 117–122.

Kuo, F-M et al. (2010). “Spectral power enhancement in a 100 GHz photonic millimeter-wave generator enabled by spectral line-by-line pulse shaping”. In: *IEEE Photonics Journal* 2.5, pp. 719–727.

Leo, François et al. (2010). “Temporal cavity solitons in one-dimensional Kerr media as bits in an all-optical buffer”. In: *Nat. Photon.* 4.7, pp. 471–476.

Chan, Han-Sung et al. (2011). “Synthesis and measurement of ultrafast waveforms from five discrete optical harmonics”. In: *Science* 331.6021, pp. 1165–1168.

Ferdous, Fahmida, Houxun Miao, et al. (2011). “Spectral line-by-line pulse shaping of on-chip microresonator frequency combs”. In: *Nature Photonics* 5.12, pp. 770–776.

Fortier, Tara M, Matthew S Kirchner, et al. (2011). “Generation of ultrastable microwaves via optical frequency division”. In: *Nature Photonics* 5.7, p. 425.

Kippenberg, Tobias J, Ronald Holzwarth, and SA Diddams (2011). “Microresonator-based optical frequency combs”. In: *Science* 332.6029, pp. 555–559.

Kleine-Ostmann, Thomas and Tadao Nagatsuma (2011). “A review on terahertz communications research”. In: *Journal of Infrared, Millimeter, and Terahertz Waves* 32.2, pp. 143–171.

Newbury, Nathan R (2011). “Searching for applications with a fine-tooth comb”. In: *Nat. Photon.* 5.4, pp. 186–188.

Swann, William C et al. (2011). “Microwave generation with low residual phase noise from a femtosecond fiber laser with an intracavity electro-optic modulator”. In: *Optics express* 19.24, pp. 24387–24395.

Ward, Jonathan and Oliver Benson (2011). *WGM microresonators: sensing, lasing and fundamental optics with microspheres.*

Cingöz, Arman et al. (2012). “Direct frequency comb spectroscopy in the extreme ultraviolet”. In: *Nature* 482.7383, pp. 68–71.

Herr, T, K Hartinger, et al. (2012). “Universal formation dynamics and noise of Kerr-frequency combs in microresonators”. In: *Nat. Photon.* 6.7, pp. 480–487.

Lee, Hansuek et al. (2012). “Chemically etched ultrahigh-Q wedge-resonator on a silicon chip”. In: *Nat. Photon.* 6.6, pp. 369–373.

Lin, Jim-Wein et al. (2012). “Photonic generation and detection of W-band chirped millimeter-wave pulses for radar”. In: *IEEE Photonics Technology Letters* 24.16, pp. 1437–1439.

Barmes, Itan, Stefan Witte, and Kjeld SE Eikema (2013). “Spatial and spectral coherent control with frequency combs”. In: *Nature Photonics* 7.1, pp. 38–42.

Chembo, Yanne K and Curtis R Menyuk (2013). “Spatiotemporal Lugiato-Lefever formalism for Kerr-comb generation in whispering-gallery-mode resonators”. In: *Phys. Rev. A* 87.5, p. 053852.

Koenig, Swen et al. (2013). “Wireless sub-THz communication system with high data rate”. In: *Nature Photonics* 7.12, p. 977.

Marpaung, David et al. (2013). “Integrated microwave photonics”. In: *Laser & Photonics Reviews* 7.4, pp. 506–538.

Matsko, Andrey B and Lute Maleki (2013). “On timing jitter of mode locked Kerr frequency combs”. In: *Opt. Express* 21.23, pp. 28862–28876.

Zhou, Xin et al. (2013). “Pair-by-pair pulse shaping for optical arbitrary waveform generation by dual-comb heterodyne”. In: *Optics letters* 38.24, pp. 5331–5333.

Bauters, Jared F et al. (2014). “Design and characterization of arrayed waveguide gratings using ultra-low loss Si 3 N 4 waveguides”. In: *Applied Physics A* 116.2, pp. 427–432.

Ghelfi, Paolo et al. (2014). “A fully photonics-based coherent radar system”. In: *Nature* 507.7492, pp. 341–345.

Hansson, T, D Modotto, and S Wabnitz (2014). “On the numerical simulation of Kerr frequency combs using coupled mode equations”. In: *Optics Communications* 312, pp. 134–136.

Herr, T, V Brasch, et al. (2014). “Temporal solitons in optical microresonators”. In: *Nat. Photon.* 8.2, pp. 145–152.

Li, Jiang, Xu Yi, et al. (2014). “Electro-optical frequency division and stable microwave synthesis”. In: *Science* 345.6194, pp. 309–313.

Rashidinejad, Amir and Andrew M Weiner (2014). “Photonic radio-frequency arbitrary waveform generation with maximal time-bandwidth product capability”. In: *Journal of Lightwave Technology* 32.20, pp. 3383–3393.

Wun, Jhih-Min et al. (2014). “Photonic high-power 160-GHz signal generation by using ultrafast photodiode and a high-repetition-rate femtosecond optical pulse train generator”. In: *IEEE Journal of Selected Topics in Quantum Electronics* 20.6, pp. 10–16.

Ataie, Vahid et al. (2015). “Subnoise detection of a fast random event”. In: *Science* 350.6266, pp. 1343–1346.

Durán, Vicente, Santiago Tainta, et al. (2015). “Ultrafast electrooptic dual-comb interferometry”. In: *Optics express* 23.23, pp. 30557–30569.

Griffith, Austin G et al. (2015). “Silicon-chip mid-infrared frequency comb generation”. In: *Nature communications* 6, p. 6299.

Liang, W et al. (2015). “High spectral purity Kerr frequency comb radio frequency photonic oscillator”. In: *Nat. Commun.* 6, p. 7957.

Rashidinejad, Amir, Daniel E Leaird, and Andrew M Weiner (2015). "Ultrabroadband radio-frequency arbitrary waveform generation with high-speed phase and amplitude modulation capability". In: *Optics express* 23.9, pp. 12265–12273.

Rashidinejad, Amir, Yihan Li, and Andrew M Weiner (2015). "Recent advances in programmable photonic-assisted ultrabroadband radio-frequency arbitrary waveform generation". In: *IEEE Journal of Quantum Electronics* 52.1, pp. 1–17.

Urick, Vincent Jude, Keith J Williams, and Jason D McKinney (2015). *Fundamentals of microwave photonics*. John Wiley & Sons. DOI: 10.1002/9781119029816.

Wang, Jian et al. (2015). "Reconfigurable radio-frequency arbitrary waveforms synthesized in a silicon photonic chip". In: *Nature communications* 6.1, pp. 1–8.

Xie, Xiaojun et al. (2015). "Photonic generation of high-power pulsed microwave signals". In: *Journal of Lightwave Technology* 33.18, pp. 3808–3814.

Yi, Xu, Qi-Fan Yang, Ki Youl Yang, Myoung-Gyun Suh, et al. (2015). "Soliton frequency comb at microwave rates in a high-Q silica microresonator". In: *Optica* 2.12, pp. 1078–1085.

Brasch, V et al. (2016). "Photonic chip–based optical frequency comb using soliton Cherenkov radiation". In: *Science* 351.6271, pp. 357–360.

Durán, Vicente, Peter A Andrekson, et al. (2016). "Electro-optic dual-comb interferometry over 40 nm bandwidth". In: *Optics letters* 41.18, pp. 4190–4193.

Karpov, Maxim et al. (2016). "Raman self-frequency shift of dissipative Kerr solitons in an optical microresonator". In: *Phys. Rev. Lett.* 116.10, p. 103902.

Nagatsuma, Tadao, Guillaume Ducournau, and Cyril C Renaud (2016). "Advances in terahertz communications accelerated by photonics". In: *Nature Photonics* 10.6, pp. 371–379.

Obrzud, Ewelina, Steve Lecomte, and Tobias Herr (2016). "Temporal Solitons in Microresonators driven by Optical Pulses". In: *Nature Photonics* 11, pp. 600–607.

Pfeiffer, Martin HP, Arne Kordts, et al. (2016). "Photonic Damascene process for integrated high-Q microresonator based nonlinear photonics". In: *Optica* 3.1, pp. 20–25.

Suh, Myoung-Gyun, Qi-Fan Yang, et al. (2016). "Microresonator soliton dual-comb spectroscopy". In: *Science* 354.6312, pp. 600–603.

Yi, Xu, Qi-Fan Yang, Ki Youl Yang, and Kerry Vahala (2016). "Theory and measurement of the soliton self-frequency shift and efficiency in optical microcavities". In: *Opt. Lett.* 41.15, pp. 3419–3422.

Bao, Chengying, Yi Xuan, et al. (2017). "Soliton repetition rate in a silicon-nitride microresonator". In: *Optics letters* 42.4, pp. 759–762.

Li, Qing et al. (2017). "Stably accessing octave-spanning microresonator frequency combs in the soliton regime". In: *Optica* 4.2, pp. 193–203.

Marin-Palomo, Pablo et al. (2017). "Microresonator-based solitons for massively parallel coherent optical communications". In: *Nature* 546.7657, pp. 274–279.

Pavlov, NG et al. (2017). "Soliton dual frequency combs in crystalline microresonators". In: *Optics Letters* 42.3, pp. 514–517.

Pfeiffer, Martin H. P. et al. (July 2017). "Octave-spanning dissipative Kerr soliton frequency combs in Si3N4 microresonators". In: *Optica* 4.7, pp. 684–691.

— (2017). "Octave-spanning dissipative Kerr soliton frequency combs in Si_3N_4 microresonators". In: *Optica* 4.7, pp. 684–691.

Pfeiffer, Martin HP, Junqiu Liu, et al. (2017). "Coupling ideality of integrated planar high-Q microresonators". In: *Physical Review Applied* 7.2, p. 024026.

Schmalz, Klaus et al. (2017). "Gas spectroscopy system for breath analysis at mm-wave/THz using SiGe BiCMOS circuits". In: *IEEE Transactions on Microwave Theory and Techniques* 65.5, pp. 1807–1818.

Yi, Xu, Qi-Fan Yang, Xueyue Zhang, et al. (2017). “Single-mode dispersive waves and soliton microcomb dynamics”. In: *Nature Communications* 8, p. 14869.

Blumenthal, Daniel J et al. (2018). “Silicon nitride in silicon photonics”. In: *Proceedings of the IEEE* 106.12, pp. 2209–2231.

Carlson, David R et al. (2018). “Ultrafast electro-optic light with subcycle control”. In: *Science* 361.6409, pp. 1358–1363.

Dutt, Avik et al. (2018). “On-chip dual-comb source for spectroscopy”. In: *Science advances* 4.3, e1701858.

Gong, Zheng et al. (2018). “High-fidelity cavity soliton generation in crystalline AlN micro-ring resonators”. In: *Optics letters* 43.18, pp. 4366–4369.

Kippenberg, Tobias J, Alexander L Gaeta, et al. (2018). “Dissipative Kerr solitons in optical microresonators”. In: *Science* 361.6402, eaan8083.

Liu, Junqiu, Arslan S Raja, et al. (2018). “Ultralow-power chip-based soliton microcombs for photonic integration”. In: *Optica* 5.10, pp. 1347–1353.

Spencer, Daryl T et al. (2018). “An optical-frequency synthesizer using integrated photonics.” In: *Nature* 557.7703, pp. 81–85.

Stern, Brian et al. (2018). “Battery-operated integrated frequency comb generator”. In: *Nature* 562.7727, pp. 401–405.

Stone, Jordan R et al. (2018). “Thermal and nonlinear dissipative-soliton dynamics in Kerr-microresonator frequency combs”. In: *Physical review letters* 121.6, p. 063902.

Suh, Myoung-Gyun and Kerry Vahala (2018). “Gigahertz-repetition-rate soliton microcombs”. In: *Optica* 5.1, pp. 65–66.

Suh, Myoung-Gyun and Kerry J Vahala (2018). “Soliton microcomb range measurement”. In: *Science* 359.6378, pp. 884–887.

Trocha, Philipp et al. (2018). “Ultrafast optical ranging using microresonator soliton frequency combs”. In: *Science* 359.6378, pp. 887–891.

Volet, Nicolas et al. (2018). “Micro-resonator soliton generated directly with a diode laser”. In: *Laser & Photonics Reviews* 12.5, p. 1700307.

Wang, Cheng et al. (2018). “Integrated lithium niobate electro-optic modulators operating at CMOS-compatible voltages”. In: *Nature* 562.7725, pp. 101–104.

Yang, Ki Youl et al. (2018). “Bridging ultrahigh-Q devices and photonic circuits”. In: *Nature Photonics* 12.5, pp. 297–302.

Yi, Xu, Qi-Fan Yang, Ki Youl Yang, and Kerry Vahala (2018). “Imaging soliton dynamics in optical microcavities”. In: *Nature communications* 9.1, pp. 1–8.

Bao, Chengying, Myoung-Gyun Suh, and Kerry Vahala (2019). “Microresonator soliton dual-comb imaging”. In: *Optica* 6.9, pp. 1110–1116.

Beling, A. et al. (2019). “High-Speed Integrated Photodiodes”. In: *2019 24th OptoElectronics and Communications Conference (OECC) and 2019 International Conference on Photonics in Switching and Computing (PSC)*, pp. 1–3.

Chang, Lin et al. (2019). “Ultra-efficient frequency comb generation in AlGaAs-on-insulator microresonators”. In: *arXiv preprint arXiv:1909.09778*.

Dülme, Sebastian et al. (2019). “300 GHz Photonic Self-Mixing Imaging-System with vertical illuminated Triple-Transit-Region Photodiode Terahertz Emitters”. In: *2019 International Topical Meeting on Microwave Photonics (MWP)*. IEEE, pp. 1–4.

Gaeta, Alexander L, Michal Lipson, and Tobias J Kippenberg (2019). “Photonic-chip-based frequency combs”. In: *Nature Photonics* 13.3, pp. 158–169.

He, Yang et al. (2019). “Self-starting bi-chromatic $LiNbO_3$ soliton microcomb”. In: *Optica* 6.9, pp. 1138–1144.

Newman, Zachary L et al. (2019). “Architecture for the photonic integration of an optical atomic clock”. In: *Optica* 6.5, pp. 680–685.

Rahim, Abdul et al. (2019). “Open-access silicon photonics platforms in Europe”. In: *IEEE Journal of Selected Topics in Quantum Electronics* 25.5, pp. 1–18.

Sun, Keye and Andreas Beling (2019). “High-Speed Photodetectors for Microwave Photonics”. In: *Applied Science* 9.4, p. 623.

Zhang, Shuangyou, Jonathan M Silver, Leonardo Del Bino, et al. (2019). “Sub-milliwatt-level microresonator solitons with extended access range using an auxiliary laser”. In: *Optica* 6.2, pp. 206–212.

Zhang, Shuangyou, Jonathan M Silver, Xiaobang Shang, et al. (2019). “Terahertz wave generation using a soliton microcomb”. In: *Optics express* 27.24, pp. 35257–35266.

Beeck, Camiel Op de et al. (2020). “Heterogeneous III-V on silicon nitride amplifiers and lasers via microtransfer printing”. In: *Optica* 7.5, pp. 386–393.

Jeong, Dongin et al. (2020). “Ultralow jitter silica microcomb”. In: *Optica* 7.9, pp. 1108–1111.

Liu, Junqiu, Erwan Lucas, et al. (2020). “Photonic microwave generation in the X-and K-band using integrated soliton microcombs”. In: *Nature Photonics*, pp. 1–6.

Lucas, Erwan et al. (2020). “Ultralow-noise photonic microwave synthesis using a soliton microcomb-based transfer oscillator”. In: *Nature Communications* 11.1, pp. 1–8.

Tan, Mengxi et al. (2020). “Photonic RF arbitrary waveform generator based on a soliton crystal micro-comb source”. In: *Journal of Lightwave Technology* 38.22, pp. 6221–6226.

Tetsumoto, Tomohiro, Fumiya Ayano, et al. (2020). “300 GHz wave generation based on a Kerr microresonator frequency comb stabilized to a low noise microwave reference”. In: *Optics Letters* 45.16, pp. 4377–4380.

Wang, Beichen, Zijiao Yang, Xiaobao Zhang, et al. (2020). “Vernier frequency division with dual-microresonator solitons”. In: *Nature communications* 11.3975.

Weng, Wenle et al. (2020). “Frequency division using a soliton-injected semiconductor gain-switched frequency comb”. In: *Science Advances* 6.39, eaba2807.

Xiang, Chao, Warren Jin, et al. (2020). “Narrow-linewidth III-V/Si/Si_3N_4 laser using multilayer heterogeneous integration”. In: *Optica* 7.1, pp. 20–21.

Yu, Qianhuan et al. (2020). “Heterogeneous photodiodes on silicon nitride waveguides”. In: *Optics express* 28.10, pp. 14824–14830.

Zang, Jizhao et al. (2020). “Wide-band Millimeter-wave Synthesizer by Integrated Microcomb Photomixing”. In: *Conference on Lasers and Electro-Optics (CLEO) 2020*. Optical Society of America.

Zhang, Long et al. (2020). “Ultrahigh-Q silicon racetrack resonators”. In: *Photonics Research* 8.5, pp. 684–689.

Jin, Warren et al. (2021). “Hertz-linewidth semiconductor lasers using CMOS-ready ultra-high-Q microresonators”. In: *Nature Photonics* 15.5, pp. 346–353.

Tetsumoto, Tomohiro, Tadao Nagatsuma, et al. (2021). “Optically referenced 300 GHz millimetre-wave oscillator”. In: *Nature Photonics* 15.7, pp. 516–522.

Wang, Beichen, Jesse S Morgan, et al. (2021). “Towards high-power, high-coherence, integrated photonic mmWave platform with microcavity solitons”. In: *Light: Science & Applications* 10.1, pp. 1–10.

Xiang, Chao, Junqiu Liu, et al. (2021). “Laser soliton microcombs heterogeneously integrated on silicon”. In: *Science* 373.6550, pp. 99–103.

Yin, Feifei et al. (2021). “Broadband radio-frequency signal synthesis by photonic-assisted channelization”. In: *Optics Express* 29.12, pp. 17839–17848.

Guo, Joel et al. (2022). “Chip-based laser with 1-hertz integrated linewidth”. In: *Science advances* 8.43, eabp9006.

Liu, Kaikai et al. (2022). “36 Hz integral linewidth laser based on a photonic integrated 4.0 m coil resonator”. In: *Optica* 9.7, pp. 770–775.

Wang, Beichen, Zijiao Yang, Shuman Sun, et al. (2022). “Radio-frequency line-by-line Fourier synthesis based on optical soliton microcombs”. In: *Photonics Research* 10.4, pp. 932–938.

Yuan, Zhiquan et al. (2022). “Correlated self-heterodyne method for ultra-low-noise laser linewidth measurements”. In: *Optics Express* 30.14, pp. 25147–25161.

Li, Jiang and Kerry Vahala (2023). “Small-sized, ultra-low phase noise photonic microwave oscillators at X-Ka bands”. In: *Optica* 10.1, pp. 33–34.